Detergent Solubilization of Mixed-Lipid Liposomes and Mixed Liposomes for Incorporation of Photosynthetic Membrane Proteins

A Dissertation Presented for the

Doctor of Philosophy

Degree

The University of Tennessee, Knoxville

Samantha Tyane Clark

December 2019

I would like to dedicate this dissertation to my mom and dad for their continuous flow of love, support, and encouragement.

Acknowledgments

I would like to thank everyone who has inspired and assisted me during my time at the University of Tennessee, Knoxville. I would first like to thank my advisor and mentor, Dr. Paul D. Frymier, for guiding me throughout this process. I thank him for giving me the opportunity to come to UTK and learn from him in his research lab. He has displayed so much insight, kindness, and patience during my time here. I would also like to thank Dr. Paul Dalhaimer, Dr. Eric Boder, and Dr. Fransisco Barrerra for providing insight and experience in research and for serving on my dissertation committee. I also thank Dr. S. Andy Sarles for lending his guidance and knowledge to enhance the scientific impact of my work.

Additionally, I would like to thank the many fellow graduate students that I have had the opportunity to learn from and work with at UTK. Among these, but not limited to, are Rosemary, Brad, Baker, Guru, and Graham. I also thank my cohort friends - Zuania, Michelle, Samiksha, Nelly, and Diana - for sharing so many great times together and enriching my time here. I also thank my friends and family from the Knoxville community and abroad who have been there to support me. Most importantly, I would like to thank my parents who taught and remind me to believe in myself, and who have given me so much help, love, and support always.

Abstract

This dissertation examines two phenomena related to the use of photosystem proteins and hydrogenase enzymes in liposomes to form light-catalyzed fusion complexes for producing molecular hydrogen. First, the method to best form fusion proteins of photosystem I (PSI) using sortase-mediated ligation was examined. In this work, a surrogate for hydrogenase, green fluorescent protein, was used and the concentrations of the ligation reaction compounds were varied to most effectively achieve fusion complexes. Second, the process of detergent solubilization of liposomes needed for PSI incorporation was examined. In this work, mixtures of lipids were used to more closely imitate natural thylakoid membranes than single lipid systems. I looked at factors that affect the ability to drive insertion of amphiphilic detergent molecules into lipid bilayers by observing changes in lipid vesicle morphology as the concentration of detergent is increased. Detergent molecules interact with liposomes by inserting their hydrophobic portion into the bilayer, thereby partitioning the lipids and causing swelling of the vesicle. As the vesicles are saturated with detergent, mixed lipid-detergent micelles bud off until there is complete dissociation of liposomes. By studying the detergent concentration these stages occur, I gained understanding about lipid-lipid interactions and factors that affect the incorporation of PSI into liposomes. In this case, I found that lipid shape, conical vs. cylindrical respectively, is a major influence in the incorporation of detergent, Triton X-100 (TX). The conical nature of ePA leads to increased mismatching within the bilayer and promotes increased uptake of TX before dissociation. Additionally, the interaction of detergent with multiple membrane types present was examined with two populations of liposomes made from egg phosphatidic acid (ePA) and egg phosphatidylcholine (ePC). An equilibrium model was derived that predicts the point of saturation for mixtures of two liposomes types and aligns with experimental observations.

Furthermore, the model estimates the number of detergent molecules incorporated into each of the liposome populations.

Table of Contents

List of Tables

List of Figures

Chapter 1

Introduction

The overarching goal of this research was to create a liposome system that enables insertion of the photosynthetic protein Photosystem I in a native-like membrane. Renewable energy is a topic of much interest as fossil fuel demands continue to rise above projected production capacity [4], and concern about greenhouse gas emissions also continues to grow. In this arena, biologically derived hydrogen production systems utilizing photosynthetic plants and microorganisms have gained attention. Plant-based materials would provide a nearly unlimited resource alternative to present technology, which uses expensive, inorganic, and rare materials. Part of the photosynthesis pathway is Photosystem I (PSI), which is a protein that absorbs solar energy and converts it into reducing power for forming carbohydrates from CO_2. This protein is an ideal candidate for providing a reductant for forming molecular hydrogen from protons owing to a quantum efficiency nearing unity (99.95%) and approximately a 1 V potential [1]. This protein has been used to create renewable energy devices that produce electricity and hydrogen fuel. However, the overall efficiency in these devices is at least two orders of magnitude lower than traditional photovoltaic materials [2].

1.1 Relevance and Applicability

Life on earth is made possible by energy from the sun. This energy is captured by organisms which readily convert it into chemical energy by a process known as photosynthesis. Photosynthesis is performed across a membrane allowing for the maintenance of proton gradients, required for energy storage in ATP. The majority of photosynthesis is oxygenic, occurring in plants, green algae, and cyanobacteria, during which carbon dioxide is absorbed from the atmosphere, energy is stored as carbohydrates, and oxygen is released in the process of aerobic respiration.

In addition to providing the energy for life, photosynthetic organisms also provide the energy that spurred the industrial revolution, as well as the majority of the fuel for modern society. Coal, petroleum, and natural gas are made from energy from the sun that was converted, compressed, and stored in organisms thousands of years ago. These sources have high concentrations of carbon that make them efficient sources of energy to drive our demands. Unfortunately, fossil fuel is most often burned to harness the energy, and in the process, many harmful gases are released into the atmosphere and water sources. Due to these environmental concerns, alternative sources of energy are currently being researched. Biofuel is one option currently in use as a source of alternative energy. Similarly to fossil fuel, the energy in biofuels also comes from the sun through photosynthesis, as it is derived from biological materials.

Other types of alternative energy have also made use of energy from the sun. The first of these is a solar water heater, which uses solar thermal energy to heat water. An extremely common collector of solar energy in many parts of the world, China for example, is the photovoltaic cell, which collects energy using the photovoltaic effect properties inherent in semi-conductors. Absorption of solar energy causes excitation of electrons within the solar cell, thereby energizing the electrons to travel freely as electrical energy. Many of these devices have an internal quantum efficiency in the 80^{th} and 90^{th} percentile, meaning that 80 to 90 charge carriers are collected for every 100 photons absorbed by the cell. However, problems with these types of energy collection devices often include health and safety concerns, along

with their price and durability. These problems make Photosystem I an attractive option for biophotovoltaics, along with the fact that PSI has a high internal quantum efficiency [3].

The aim of this work with PSI is to increase the *in vitro* photo-efficiency of the protein in a photovoltaic device by developing the groundwork for insertion of membrane proteins into synthetic lipid bilayers, called liposomes, through detergent mediated solubilization. PSI is located within the thylakoid membrane, which is composed of a mixture of lipid types and fatty acids. The majority of research performed on detergent solubilization has focused on single lipid liposomes. This dissertation aims to close the gap between single lipid liposomes solubilizations and liposomes that more closely mimic the thylakoid membrane.

1.2 Objectives and Organization of Chapters

The objectives were to develop a framework for a native-like synthetic membrane for PSI. These gaps have been filled here by the solubilization of naturally derived lipid liposomes and by establishing the activity and functionalization of a mutant PSI. In Chapter 2, the literature on photosynthesis and photosynthetic devices, as well as the state of research in the formation of functionalized membranes, including liposomes is described. In Chapter 3, the structure and functionalization of mutant PSI are compared with that of wild type PSI. In Chapter 4, mixed-lipid liposomes are utilized to develop a model for understanding detergent association with membranes dependent on lipid shape. In Chapter 5, an equilibrium mode is derived for detergent association with multiple populations of liposomes. Lastly, in Chapter 6, the overarching conclusions are summarized and future directions for this work are presented.

References

[1] Alexey Amunts and Nathan Nelson. "Plant Photosystem I Design in the Light of Evolution". In: *Structure* 17.5 (2009), pp. 637–650.

[2] Rosemary K Le. "Photosystem I-Based Applications for the Photo-catalyzed Production of Hydrogen and Electricity". In: *Dissertation* (2014).

[3] Nathan Nelson. "Plant Photosystem I – The Most Efficient Nano-Photochemical Machine". In: *Journal of Nanoscience and Nanotechnology* 9 (2009), pp. 1709–1713.

[4] U.S. Energy Information Administration. *Annual Energy Outlook 2016 with Projections to 2040*. Tech. rep. Department of Energy, 2016.

Chapter 2

Literature Review

2.1 Photosystem I

Photosynthesis is the process by which plants and cyanobacteria convert sunlight and water into energy to promote growth and subsistence. This process occurs in the thylakoid membrane as a highly efficient photosynthetic reaction system that works in two stages, each of which occurs in a large protein complex. This is observed in Figure 2.1.

In the first stage, within Photosystem II (PSII), electrons are harvested from water molecules, and in the second stage, within Photosystem I (PSI), the electrons are energized to allow for energy storage. PSII and PSI are housed in the thylakoid membrane, which has an acidic aqueous environment on the inside called the lumen, and a neutral aqueous environment on the outside called the stroma. The stroma also houses proteins responsible for carbohydrate production. Both protein complexes contain hundreds of light-absorbing pigment molecules that transfer photons as resonance and vibrational energy to a reaction center to be used. In PSII, photons are absorbed and funneled to a manganese center in the lumen, which acts as an oxygen-evolving complex and catalyzes the division of water into protons and oxygen, O_2. Electrons are released into an electron transport chain in PSII (see Figure 2.1). These electrons are passed through a series of electron acceptors in PSII until it reaches plastoquinone (PQ), where it assists in creating a proton gradient by binding protons to PQ and moving them from the stroma to the lumen. PQ migrates through the membrane to the cytochrome b_6f complex, where it releases protons and electrons.

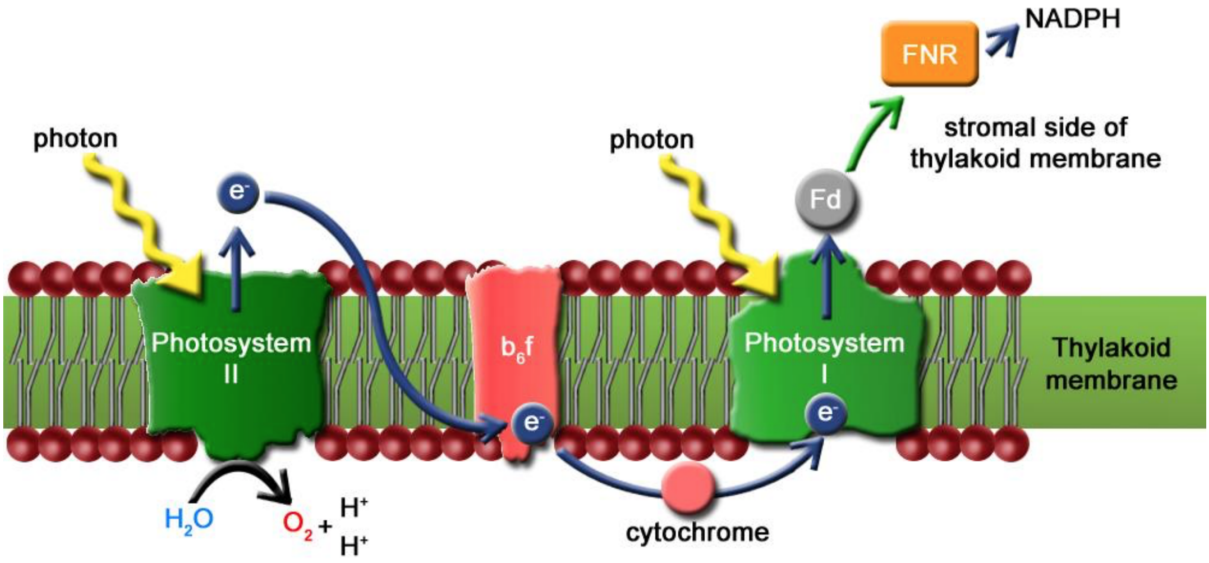

Figure 2.1: Photosynthetic electron transport chain in the thylakoid membrane. (Reproduced with permission from Le [41].)

The electrons are then shuttled through the cytochrome b_6f complex to a soluble electron carrier, like cytochrome, which diffuses through the lumen to PSI. Photons absorbed by light-harvesting complexes in association with PSI are transported to the reaction center and induce charge separation, passing an electron through a transport chain to the stroma, where it can be converted into chemical energy. The P700 reaction center is re-reduced by cytochrome or other donors present. In the stroma, ferrodoxin (Fd) is present to accept the electron from PSI and transport it to Fd-NADP oxidoreductase where it is used in the reduction of nicotinamide adenine dinucleotide phosphate (NADP+) to nicotinamide adenine dinucleotide phosphate-oxidase (NADPH). An alternative to the ferrodoxin pathways occurs in the presence of hydrogenase enzymes, which utilize the electrons to reduce protons and form molecular hydrogen. In addition to the electron pathway, photosynthesis also assists in the creation of another energy storage molecule, adenosine triphosphate (ATP). ATP production is driven by the electrochemical proton gradient across the thylakoid membrane, which powers the ATP synthase enzyme complex in the binding of inorganic phosphate (Pi) with adenosine diphosphate (ADP). NADPH and ATP can then be used as reducing agents in the Calvin Cycle to upgrade the energy to the carbohydrate storage form [7].

The architecture of light-harvesting complexes and electron transport chain in PSI is highly complex. In *Thermosynechococcus elongatus* (*T. elongatus*), each PSI monomer is formed by 12 polypeptide subunits (see Figure 2.2). Much of the interwoven peptide structure is highly conserved between photosynthetic organisms. It consists of 23 transmembrane α-helices, and a three protein stromal hump [11]. Within this structure are 127 cofactors, consisting of 2 phylloquinones, 3 iron-sulfur clusters, 22 carotenoids, 4 lipids, a calcium ion, and 96 chlorophylls a's – six of which are responsible for electron transfer, while the other ninety act as photon antennas. In cyanobacteria, PSI monomers exist primarily in groups of three joined homo-monomeric complexes weighing 1068 kilodaltons together [33]. In *T. elongatus*, the clover-leaf-like PSI trimer has a diameter of 22 nm and a height of 10.5 nm [25, 9]. Variations in PSI exist between photosynthetic species, as *Synechocystis* PCC 6803 only contains 11 polypeptide subunits, and in plants, PSI is present as a monomer with light harvesting complexes (See Figure 2.2).

In all photosynthetic organisms, the electron transport chain in this protein complex is centered about a heterodimer formed by integral membrane proteins, PsaA and PsaB (see Figure 2.3). These proteins are made of 11 transmembrane helices each. At their luminal juncture is a P700 reaction center, fashioned by a chlorophyll a epimer (Chl$a$') and regular chlorophyll a (Chl$a$), which causes charge separation when excited. Corresponding chlorophyll a's in position A are present to accept electrons and allow transfer to a subsequent Chl$a$ at A_0. Following the electron's path, phylloquinones QK-A and QK-B, are then utilized as acceptors. Although the reduction pathway is present in both PsaA and PsaB, there is evidence to demonstrate electrons only follow the one in the PsaA subunit. Kinetic studies have shown the reaction rate in PsaA is much faster than in PsaB. The alternative pathway is likely an artifact of early photosynthetic systems [72, 10]. After reduction of QK-A, electrons are transferred to a shared [4Fe-4S] cube, named F_x, near the lumen and upper PSI subunit, PsaC. PsaC houses two more iron-sulfur clusters, whose proximity allows the transfer of redox potential to F_A, then on to F_B based on proximity of the structures. The upper PsaC subunit is a part of the stromal hump, also containing PsaD and PsaE subunits. These three polypeptide subunits extend into the stroma and are responsible for creating an electrostatic binding pocket for functional electron-accepting proteins, such as ferredoxin or

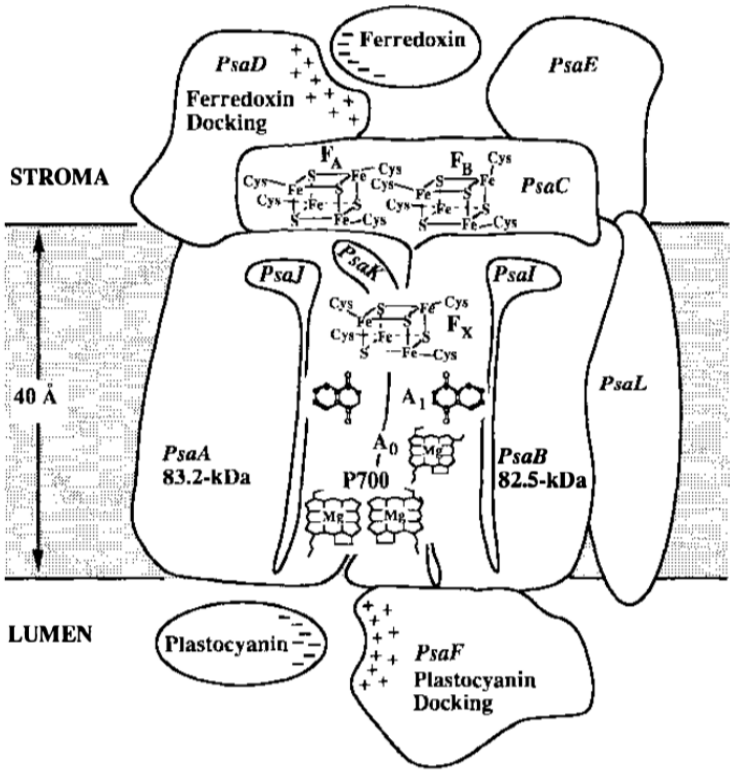

Figure 2.2: Depiction of Photosystem I protein complex with labeled subunits and inset electron transport chain. (Reproduced with permission [21].)

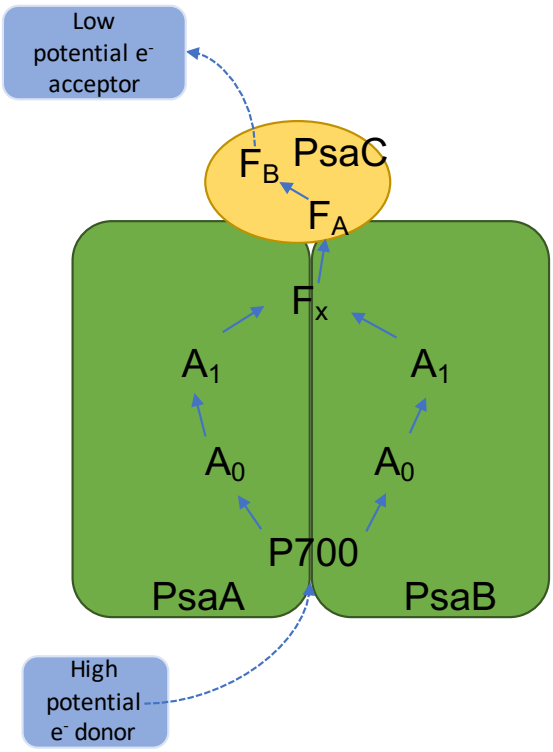

Figure 2.3: PSI electron transport pathway. Upon illumination, P700 passes an electron through 2 chlorophyll *a* molecules (A_0, A_1) in the PsaB subunit and three iron-sulfur clusters (F_X, F_A, F_B), and externally to a low potential electron acceptor. P700 is re-reduced by a high potential electron donor, such as $DCPIP^-$.

flavodoxin. These proteins allow the release of reductants from PSI and re-reduction at the active site [33, 72, 11, 20]. Other subunits that assist in PSI function are PsaF and PsaL. These polypeptides extend into the lumen and electrostatically bind PC to receive electrons at the reaction center. Additionally, in cyanobacteria, PsaL functions to bind three PSI monomers into a trimer by electrostatic interactions.

In addition to forming the reaction center, PsaA and PsaB play an important part in binding and orienting most of the chlorophyll in Figure 2.4, and all of the carotenoid pigments responsible for harvesting photons. Chlorophyll molecules can also be found in the proteins which surround the core – PsaJ, PsaK, PsaL, PsaM, and PsaX (if present). Each of these small hydrophobic proteins binds 1-3 Chl*a*'s as well. These chlorophyll molecules are efficient absorbers of light at 430nm and 663nm. The beauty of the number of chlorophylls present in close proximity is that, as photons are absorbed and Chl*a* is excited to the first excited singlet state, the energy is converted to vibrational and rotational excitation, which can be

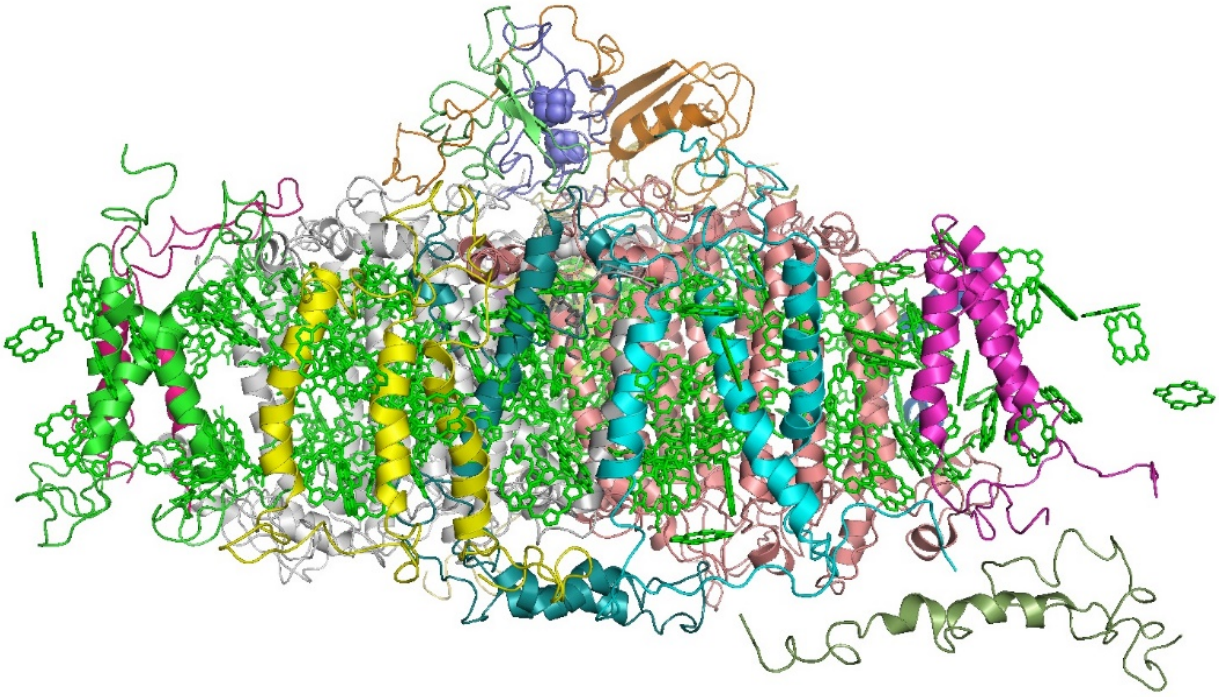

Figure 2.4: Ribbon structure of plant PSI with bound chlorophyll pigments., shown in green. Depiction of PDB ID: 1JB0. [8]

passed to neighboring Chl*a*'s and funneled to the P700 reaction center for charge separation. Additional resonance energy comes from carotenoids which assist in the collection of light at wavelengths primarily between 400 and 500 nm's [11]. This combination of light energy absorption and energy transfer to the reaction center yields an exceptional midpoint potential of -1.3 V in the charge-separated state (see Figure 2.5) [20].

These remarkable electronic properties of PSI make it a good candidate for studies utilizing light energy to generate photocurrents in a biological photovoltaic cell. Many studies have made use of this by the attachment of reaction centers to substrates for the collection of photo-electricity. These studies have looked at different methods to attach PSI to an electrode and different electrodes compatibilities with PSI [59, 51, 64, 47, 39, 38, 13, 3, 43, 26, 23]. The highest reported photocurrent in an artificial nano-device is 335 $e^{-}s^{-1}PSI^{-1}$ [38]. *In vivo* electron transport in PSI occurs at a rate of 47 $e^{-}s^{-1}PSI^{-1}$, which is a seventh of the rate of that device. Part of this efficiency gain in nano-devices is the avoidance of

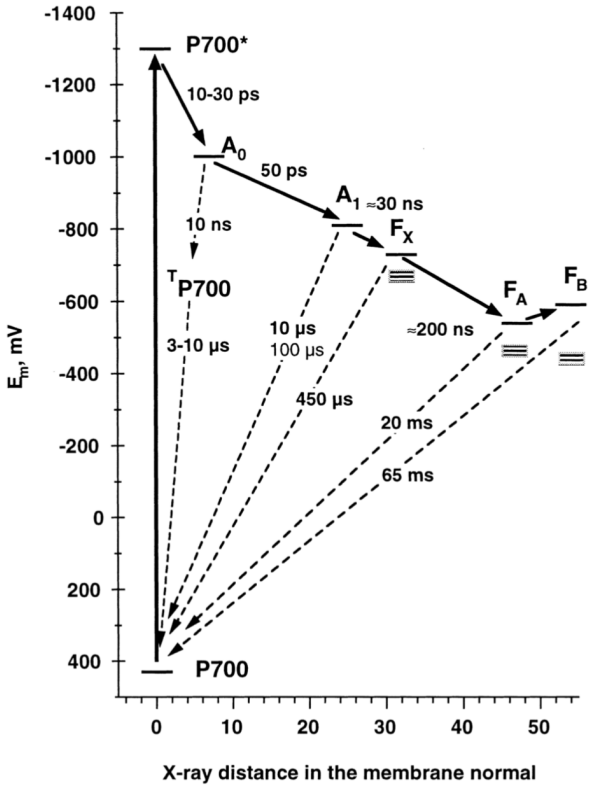

Figure 2.5: Electrochemical potential gain in PSI upon photo-reduction. (Reproduced with permission [66].)

the diffusion limited step for association of electron donors with the PsaF dock of natural photosynthesis.

Another option seeking to harness the photo-potential of PSI is the production of hydrogen (H_2), which is an energy carrier for a sustainable energy infrastructure. *In vivo* electrons are passed off to ferrodoxin; however, in the presence of hydrogenase enzymes, the electron is used in the reduction of two protons to form molecular hydrogen. To make use of this *in vitro*, hydrogenase enzymes have been attached to the stromal hump of PSI, and H_2 production has been observed [31, 39, 62, 46]. Alternatively, H^+ reduction reactions have also been produced by attaching a metal catalyst (platinum) to PSI [32]. The ability to produce electricity and hydrogen *in vitro* makes PSI a good candidate for future research in renewable energy and photovoltaic nano-devices.

2.2 Biological Membranes and Protein Reconstitution

In the majority of research on PSI, the protein is not in an environment similar to its native one. The lack of native lipids can have a detrimental effect on both the protein's stability [27] and its activity [71]. *In vivo*, photosynthetic proteins are located in the thylakoid membrane. The membrane effectively surrounds PSI by a lipid bilayer that shields the protein's hydrophobic regions from the cell's aqueous environment and provides lateral pressures to the protein complex, while simultaneously allowing the hydrophilic top and bottom to interact with other proteins in the stroma and lumen. The thylakoid membrane is composed of four different types of lipid molecules: phosphatidylglycerol (PG), monoglactosyl diacylglycerol (MGDG), digalactosyl dicaylglycerol (DGDG), and sulfoquinovosyl diacylglycerol (SQDG) [15, 48, 22]. SQDG and PG carry a negative charge, while MGDG and DGDG remain neutral. The presence of PG and MGDG, in particular, are important for holding PSI trimers together; without them, the N-terminus of PsaL has a high degree of deviation, leading to instability of the trimeric complex [27]. The tight binding of the lipids to the protein can be observed in crystalized PSI, which contains three PG molecules and one MGDG molecule [33]. Furthermore, functional studies of PSI in the

presence of PG have demonstrated the lipids' importance in stimulating electron transport [71].

Usually membrane proteins are isolated from their beneficial native lipid bilayer to study. This is most commonly performed with detergents, which surround the hydrophobic helices of the protein and insert themselves into the interstitial space between the clover-leaf formation of monomers [42]. Detergent molecules are conical in shape, as seen in Figure 2.6, with a hydrophilic head group and a singular short fatty acid chain. In an aqueous solution, they spontaneously group into micelles to avoid hydrophobic interactions with water. Micelles are formed as the hydrophobic tails come together and are shielded from water by the head groups (see Figure 2.6B). In general, micelles are spherical but do have a slight degree of ellipticity depending on the size and shape of each particular detergent [52]. Due to the natural formation of detergents, they make a toroidal belt around the hydrophobic portion of proteins. This can be seen in the simulation of detergent (●) surrounding a PSI trimer (●) in Figure 2.7. At high detergent concentrations, the electrostatic interactions between PsaL subunits of cyanobacterial PSI trimers can cause the multimer to separate into monomers [51]. It should be noted that a decrease in activity has not been seen in the disassembly of PSI trimers in detergent [16, 4].

To better simulate *in vivo* environments for membrane proteins, other methods of protein solubilization have been examined. These methods look at the effect of lipopeptide on PSI structure and function [70, 18, 36]. However, these systems also form a toroidal belt-like structure around PSI and fall short of replicating the macroscopic environment that lipid membranes provide (Figure 2.7).

More native-like environments can be found in planar and spherical lipid bilayers. Lipid molecules are cylindrical in shape and are composed of a large hydrophilic head group, which may or may not be charged, as well as two hydrophobic fatty acid chains (see Figure 2.6C and 2.6D). The number of carbon atoms and the degree of saturation, or rigidity, varies amongst acyl chains. The properties of lipids affect interactions with one another and with proteins as well. When lipid molecules are exposed to water, they spontaneously organize to minimize water exposure. For the vast majority of lipids, this is a spherical bilayer and is referred to as a liposome or vesicle. In addition to forming a membrane, liposomes are

also able to better replicate the curvature and lateral pressures found in living cells than micelles. Membrane curvature has an important role in charge distribution across many membranes, including the thylakoid. There is an asymmetric distribution of charges, with negatively charged lipids predominating in the inner leaflet. This lipid asymmetry, along with curvature, affects membrane protein orientation such that the more electrostatically positive end of the protein is facing the inner layer [17, 68]. The asymmetry found *in vivo* is consistent with *in vitro* studies as well [55, 6]. Other factors that affect the stability and activity of proteins within lipid bilayer are membrane thickness [2] and fluidity [28].

Formation of lipid bilayers *in vitro* is spontaneous. Figure 2.8 demonstrates two processes by which vesicles can be formed. Lipids are dried from an organic solvent solution into a film. As an aqueous buffer is added to the film, it dissolves the lipids, causing hydrophobic tails of the cylindrical lipids to come together and form bilayer sheets. To reduce surface tension, the sheets swell and bud off into vesicles, often containing smaller concentric bilayers within them; these are called multilamellar vesicles. Freezing and thawing break the multilamellar vesicles into unilamellar vesicles, which contain only one lipid bilayer. To control the size and uniformity of liposomes, the solution can be extruded through filters with pores of the desired final vesicle diameter, or the solution can be placed in a bath sonicator, which uses ultrasonic waves to break the liposomes into small unilamellar vesicles [40]. However, the effectiveness of these techniques is highly dependent on the type of lipid and the mixture of lipids, as well as the pH and electrolyte concentration of the buffer with which the lipids are hydrated [5]. Additionally, certain lipids must be heated above their transition temperature from a gel to a fluid state for the tail groups to become mobile enough to realign into new structures. Other lipids, such as dipalmitoylphosphatidylcholine (DPPC) require substantial sonication to form stable liposomes; otherwise, it will precipitate [34]. Once liposomes are formed, detergent can be added to weaken the interactions between lipid molecules. At this point, detergent-solubilized proteins can be added, and protein will then self-insert into the weakened membrane when detergent is removed. Common methods for the removal of detergents include dialysis, gel chromatography, hydrophobic adsorption onto polystyrene beads, and dilution [57].

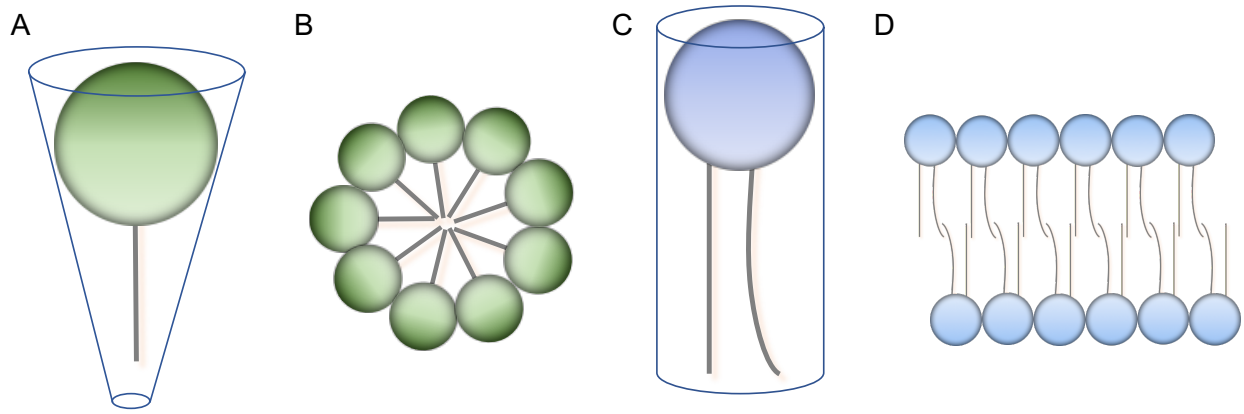

Figure 2.6: Depiction of (A) conical shape of a detergent which forms (B) micelle at high enough concentrations in solutions, and the (C) cylindrical shape of a lipid which forms a (D) lipid bilayer in water. Hydrophobic tails are gray, and hydrophilic head groups are blue or green.

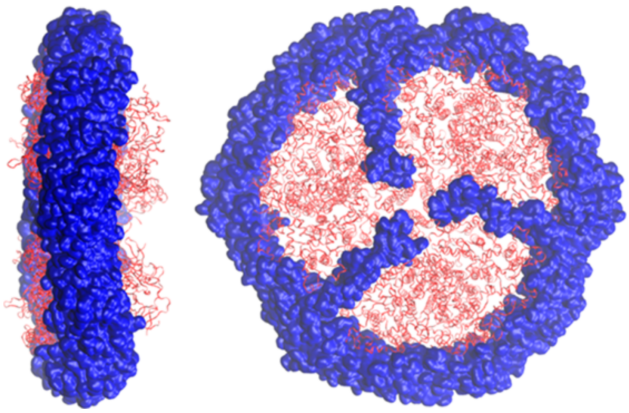

Figure 2.7: All-atom molecular dynamics simulation of PSI trimer (●) in DDM detergent (●). (Reproduced with permission [27].)

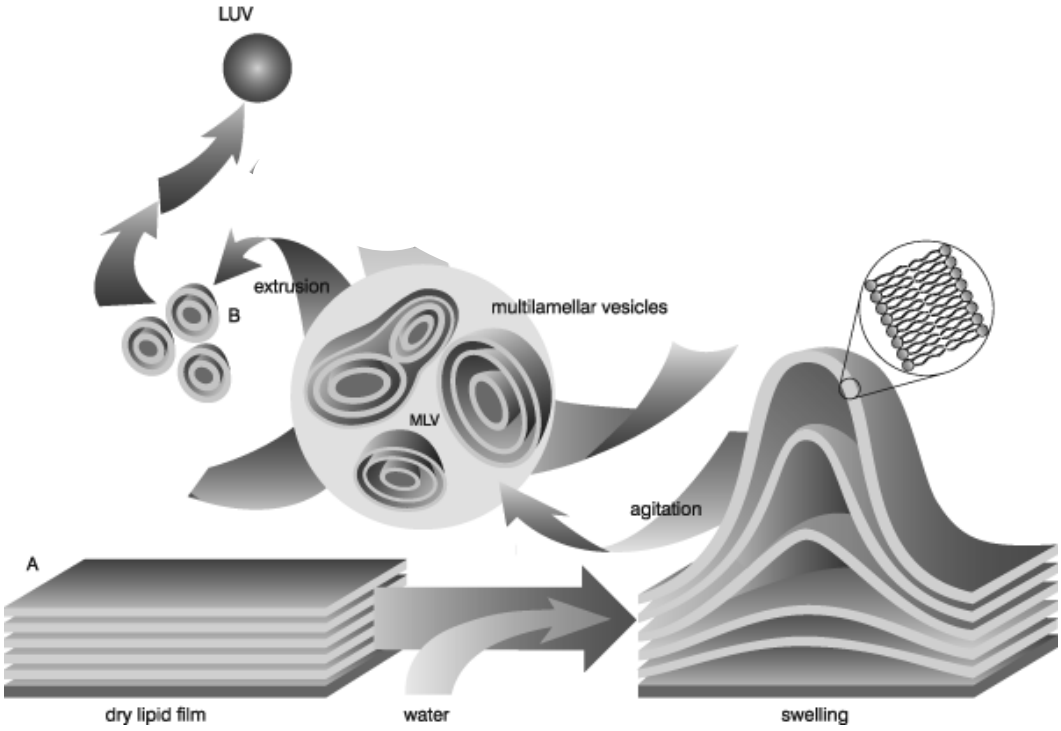

Figure 2.8: Formation of liposomes from dried lipid films in the presence of an aqueous buffer. (Figure adapted from [40].)

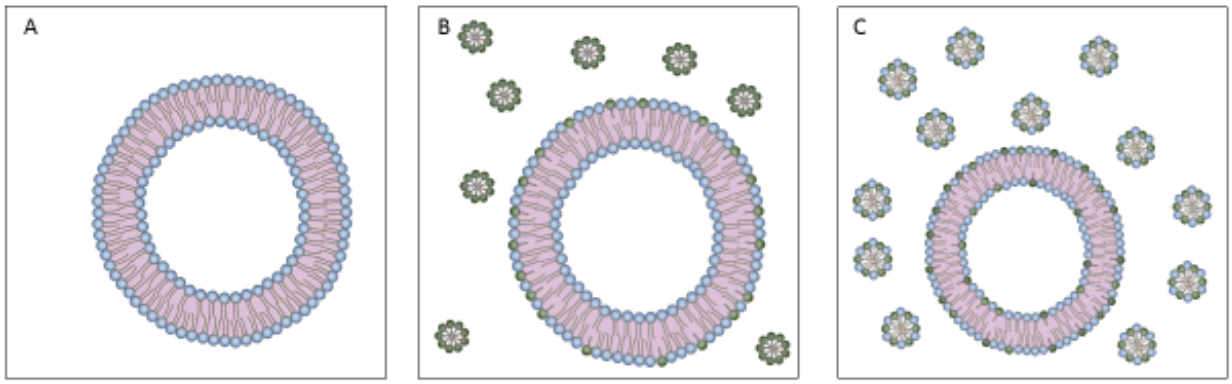

Figure 2.9: Stages of solubilization of a liposome with detergent molecules (green). A) Lipid (● and ●) only liposome. B) Detergent (●) micelles and detergent integration into the outer shell of liposomes. C) Equilibration of the inner and outer leaflet of liposomes, followed by the budding of detergent and lipid mixed micelles.

The mechanism of detergent addition into liposomes has been well studied over the last twenty years. The molar ratio of lipid to detergent plays an important role in both the ability to reconstitute membrane proteins into liposomes as well as the ability to control the directionality of proteins – a very important factor in observing the activity of any protein. Adjustment of the lipid:detergent ratio affects the size of particles in solution; therefore, spectroscopic techniques are commonly used to observe these changes [45, 63, 67]. Upon initial addition of detergent, liposomes swell relatively rapidly as detergent penetrates the outer shell (Figure 2.9b); this is followed by equilibration between the inner and outer leaflet as detergent molecules move from the outer lipid layer to the inner layer, or "flip-flop." Further detergent addition yields saturation of the bilayer and permeabilization of the membrane, during which a maximum diameter is reached. As detergent concentration increases, thread-like mixed micelles composed of detergent and lipid bud off of the shrinking vesicle until the complete bilayer has dissipated (Figure 2.9c) [45]. Reviews of detergent solubilization in different lipid systems can be found in Lichtenberg *et al.* [45], Seddon *et al.* [63], and Riguad and Levy [67].

UV-Vis spectrophotometry is used to examine the changes in turbidity. The Mie theory describes the direct proportionality of absorbance to the size of particles in solution [12]. Figure 2.10 demonstrates an typical turbidity curve for liposome solubilization of large and small unilamellar vesicles (LUV and SUV, respectively). It shows absorbance of particles

as a function of increased detergent to lipid ratio. In Panel I, vesicles are saturated with detergent, causing swelling and increased absorbance to the peak, D_{sat}. Further addition of detergent causes mixed detergent-lipid micelles to bud off of the liposome, and absorbance to decrease (panel II) until D_{sol}, in which liposomes have completely dissolved into mixed micelles and absorbance reaches a minimum (panel III). This method has been developed and studied thoroughly by Rigaud and Goni [56, 65]. Their works have sought to optimize the point of liposome solubilization for the best protein reconstitution, which has indicated the best ratios of detergents to lipids for different systems.

Another optimization for morphology and size homogeneity in protein reconstitution deals with the speed of detergent removal. Non-polar polystyrene beads have a high surface area with a high adsorption affinity for small detergent molecules. The quantity of beads in solution is proportional to the rate of detergent removal, thus lending to slow or fast removal, which yields larger liposomes with asymmetric protein orientation or smaller liposomes with symmetric protein orientation, respectively. Methods dictating ratios of lipids, detergents, and hydrophobic resins are further described in J. Rigaud *et al.* [67].

By way of this prescribed liposome formation method, many membrane proteins have been reconstituted in synthetic membranes. Amongst these proteins are the lactose transport protein (LacS) of *Streptococcus thermophilus*, which was reconstituted into vesicles formed by multiple freeze/thaw cycles and extrusions [35]. Reconstitution efficiency was examined by Knot *et. al.* [35] for uniform directionality and protein activity using two separate detergents, Triton X-100 and n-dodecyl beta-D-maltoside (DDM). Figure 2.11 demonstrates the results from this study. In Figure 2.11A, a detergent solubilization curve was generated by measuring absorbance (left y-axis) to monitor physical changes in the size of the liposomes with increasing detergent concentration (x-axis). The solubilization curves for DDM and TX followed the typical stages of saturation (R_{sat}) and solubilization (R_{sol}), which were described above. LacS was reconstituted into liposomes at the increasing detergent concentrations, and the protein activity was observed through lactose counter-flow measurements (right y-axis) in Figure 2.11A. For LacS reconstitution using DDM, the highest counterflow activity was observed at R_{sat}. Comparatively, for LacS reconstituted into liposomes using TX, similar counterflow activity was observed at R_{sat} and R_{sol}. To better understand the physical

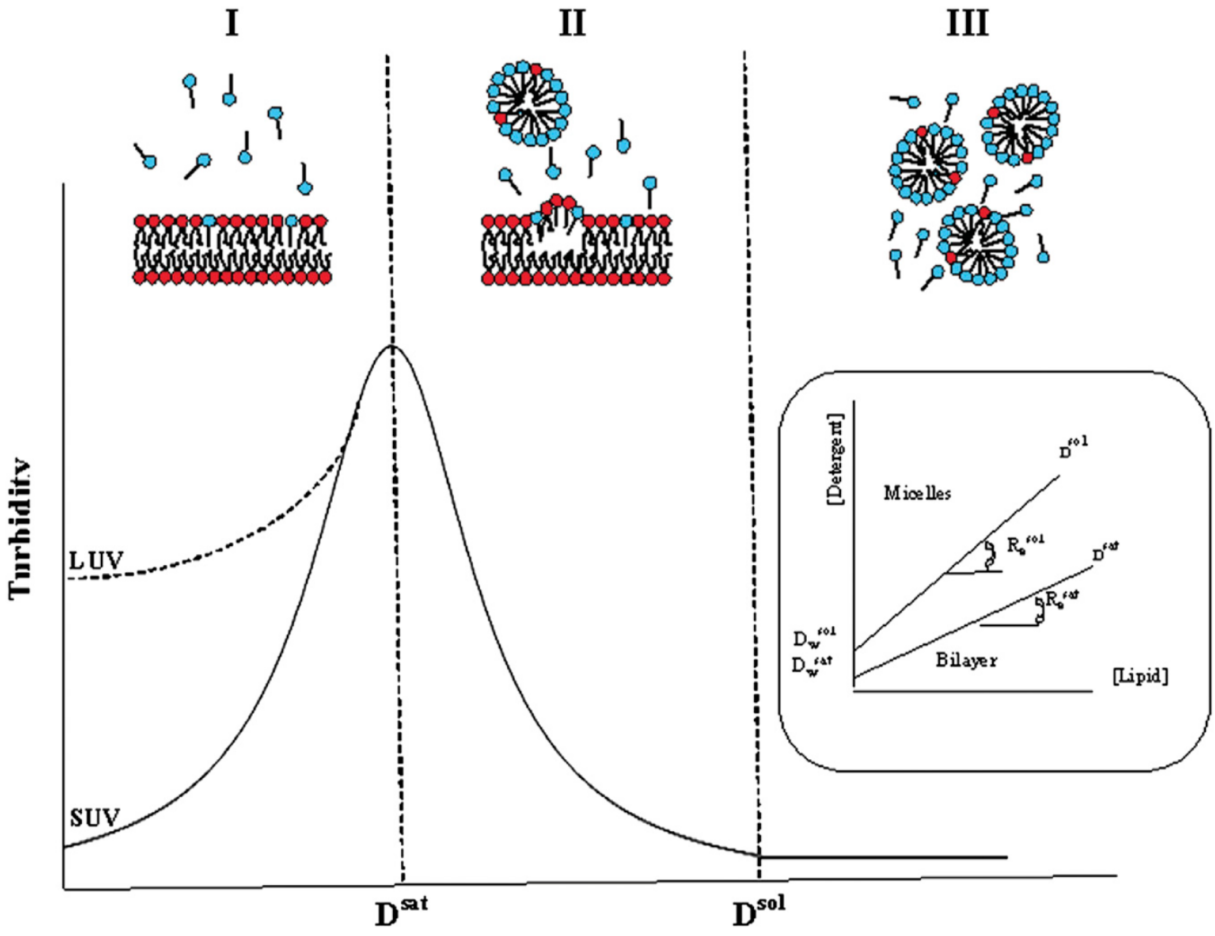

Figure 2.10: Turbidity is measured as the detergent-lipid ratios increase and structural changes occur in the liposome. (Reproduced with permission [44].)

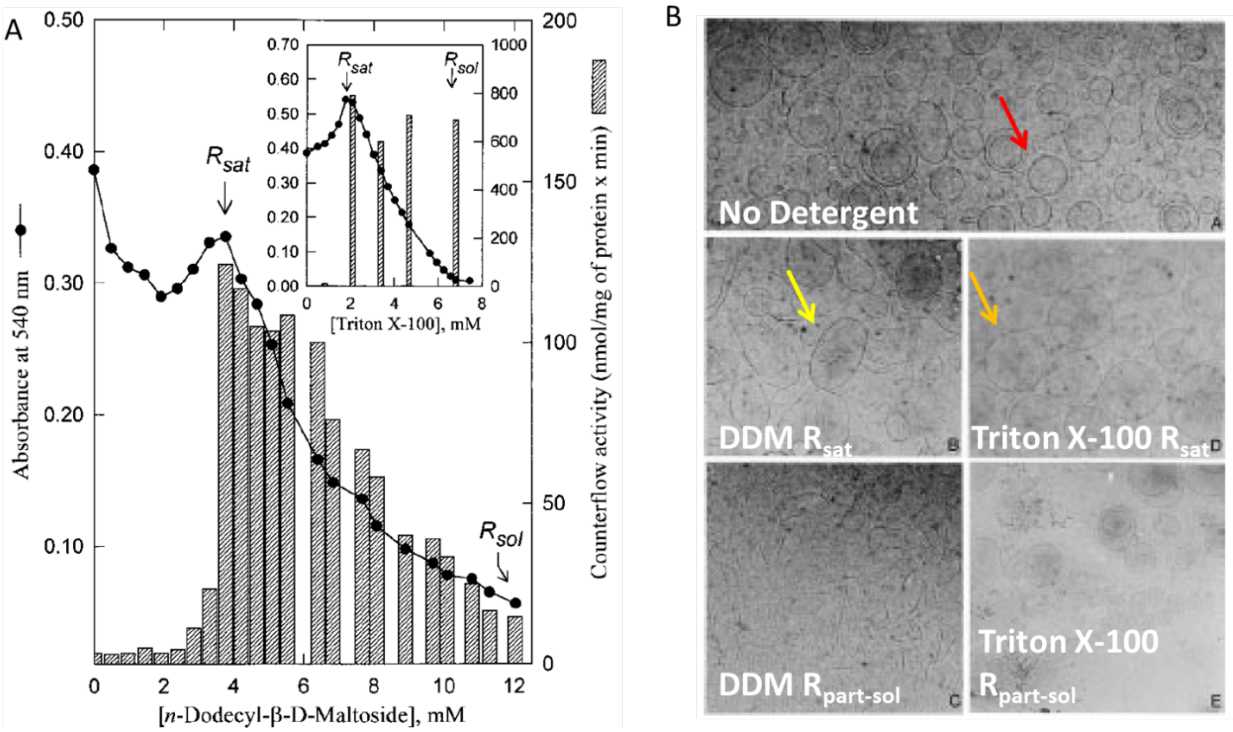

Figure 2.11: Reconstitution of lactose trasnport protein (LacS) into vesicles. A) Black dots and line represent the absorption curve for increasing concentrations of DDM into liposomes. The underlay bars indicate activity measurements for the counterflow of lactose through the vesicle. The inset represents the absorption and activity using Triton X-100 for reconstitution. B) Cryo-TEM images of liposomes at points of no detergent (A), the onset of solubilization (B, D), and partial solubilization (C,E) with DDM and Triton X-100. (Reproduced with permission [35].)

structures before and after detergent addition, cryo-TEM images are given (Figure 2.11B). In Figure 2.11B-A, there are well formed, fairly monodispersed vesicles. In Figure 2.11B-B and Figure 2.11B-D, at the onset of solubilization with DDM and Triton X-100, respectively, the liposomes have swollen; here, DDM has become slightly ovular. Continued DDM and Triton X-100 addition yield no distinct shapes by partial solubilization (Figure 2.11B-C and Figure 2.11B-D). At full solubilization, absolutely no distinguishable shapes are expected to be seen.

Similarly, cytochrome-c oxidase (COX) from beef heart was reconstituted into soy-bean sourced phosphatidylcholine vesicles – formed by sonication – using the detergent-reconstitution method by Rubinson et al. Small-angle neutron scattering was performed on the reconstituted protein. By analyzing the scattering curve of the protein shape, researchers

were able to determine COX proteins are dimers forming in the membrane. This differs from the crystal structure, which is monomeric. Additionally, biochemical assays confirm the functionality of COX as a dimer [58].

Some other proteins which have been successfully reconstituted into liposomes are an ATP-binding cassette (ABC) transporter, a truncated AgrC histidine kinase, a pro-apoptotic Bax protein, and a G protein-coupled receptor [19, 69, 61, 49]. These studies have demonstrated proof of incorporation of proteins into liposomes and the activity of the proteins as well.

Additionally, Photosystems I and II have been reconstituted into liposomes, which is of great importance in research regarding bio-photovoltaics in membranes [37, 53, 30, 14, 54]. The ability to create a transmembrane electric field with a photosystem was first postulated in 1966 by P. Mitchell [50]. PSI from pea chloroplast, along with bacteriorhodopsin and bacteriochlorophyll from *Rhodospirillum rubrum* was first reconstituted into liposomes in 1976 by Barsky *et al.* [37]. The method involved hydration of soybean phospholipids and detergent, followed by sonication, the addition of solubilized proteins, then further sonication. Dialysis was performed to drastically reduce the detergent concentration. The proteoliposososomes were pelleted by centrifugation and resuspended. The resulting proteoliposomes were assayed for protein activity by a change in concentration of the phenyldicarborane anion (PCB^-). In PSI systems, a PCB^- reduction reaction can only occur in the presence of substrates which can bind and donate to PSI. In Figure 2.12, this occurs only when phenazinemethosulfate (PMS) is present to accept the reductant and react with PSI for charge separation under light conditions. This reaction is maximized after the addition of ascorbate, which acts a donor and enables repeated charge separation by accepting electrons passed across the membrane by PSI.

Subsequent works in the field were performed by Orlich and Hauska in 1980 [53], who successfully reconstituted spinach PSI and demonstrated the activity by measuring oxygen uptake rate and fluorescence of 9-aminoacridine (9AA), a dye which fluoresces in the reduced state. Figure 2.13 shows a decrease in dye fluorescence with PSI activity in the presence of PMS and ascorbate. They also found that valinomycin increased activity by assisting in H^+ transport out of the vesicle, while photo-phosphorylation uncoupler

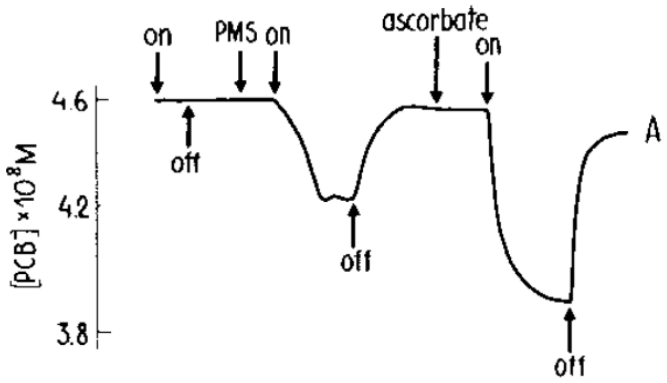

Figure 2.12: PCB^- uptake by PSI in liposomes, without PMS, with PMS, and with PMS and ascorbate under light conditions (on). (Reproduced with permission [37].)

decreased it. Additionally, in this work, PSI and ATP-ase were co-reconstituted for photo-phosphorylation, and ATP formation was measured [53].

Other investigators have shown that proteoliposomes can reunite separately solubilized spinach light-harvesting complexes with the P700 reaction center, thus increasing the rate of photo-oxidation [29]. Additionally, permeable and impermeable electron acceptors and donors have been used to show that 90% of PSI reaction centers in vesicles are oriented with their stromal hump outside of the membrane [60].

Cladera et al. added to this body of work by comparing the efficiency of Triton X-100 and octylglucoside (OG) detergents in reconstituting PSI into extruded liposomes of 9:1 (mol/mol) egg phosphatidylchline and egg phosphatic acid. In Figure 2.14, fluorescence reduction of 9AA is measured with proteoliposomes formed with each detergent at the onset of, partial, and full solubilization of liposomes, as discussed previously. The most efficient proteoliposome formation was partial solubilization with OG. Furthermore, homogeneous PSI directionality was observed in this work [14].

The most recently published work involving PSI in a membrane has used a computational modeling approach to quantitatively describe light-induced proton gradient across a PSI-proteoliposome membrane. This was verified experimentally by following a similar method as described previously [54]. Figure 2.15 shows the alignment of experimental and model data for photo-reduction of PSI in the presence of PMS, ascorbate, and 9AA.

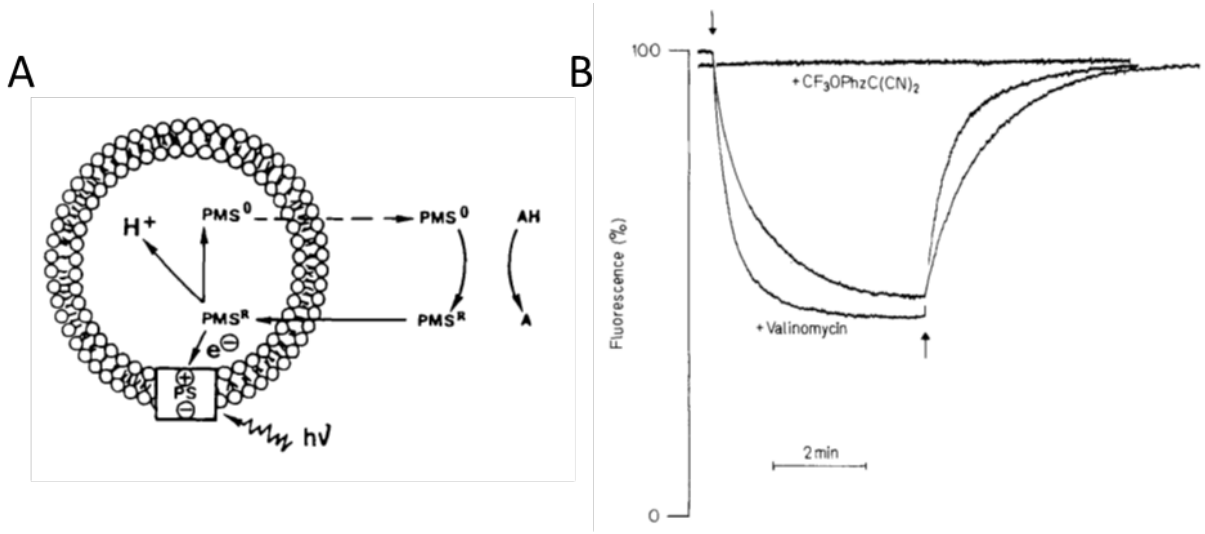

Figure 2.13: (A)Reaction chemistry of PSI in a liposome in which PMS is reduced by 9AA (labeled AH) leading to a fluorescence reduction. PMS photo-reduces PSI, forming a proton gradient (Reproduced with persmission[14]. (B) A decrease in 9AA dye fluorescence percentage occurs when PSI proteoliposomes are reduced in the presence of PMS and ascorbate, and $CF_3OPh_zC(CN)_2$, or valinomycin as indicated. (Reproduced with permission [53].)

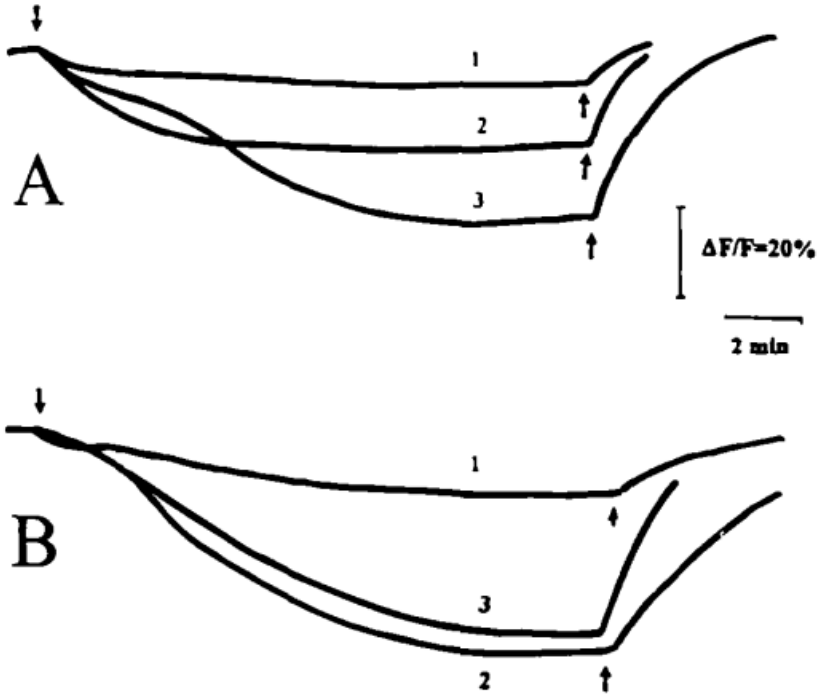

Figure 2.14: There is a decrease in 9AA fluorescence for PSI proteoliposomes formed by (A) Triton X-100 and (B) OG. Curves 1, 2, and 3 correspond to the onset of solubilization, half solubilization, and total solubilization, respectively. (Reproduced with permission [14].)

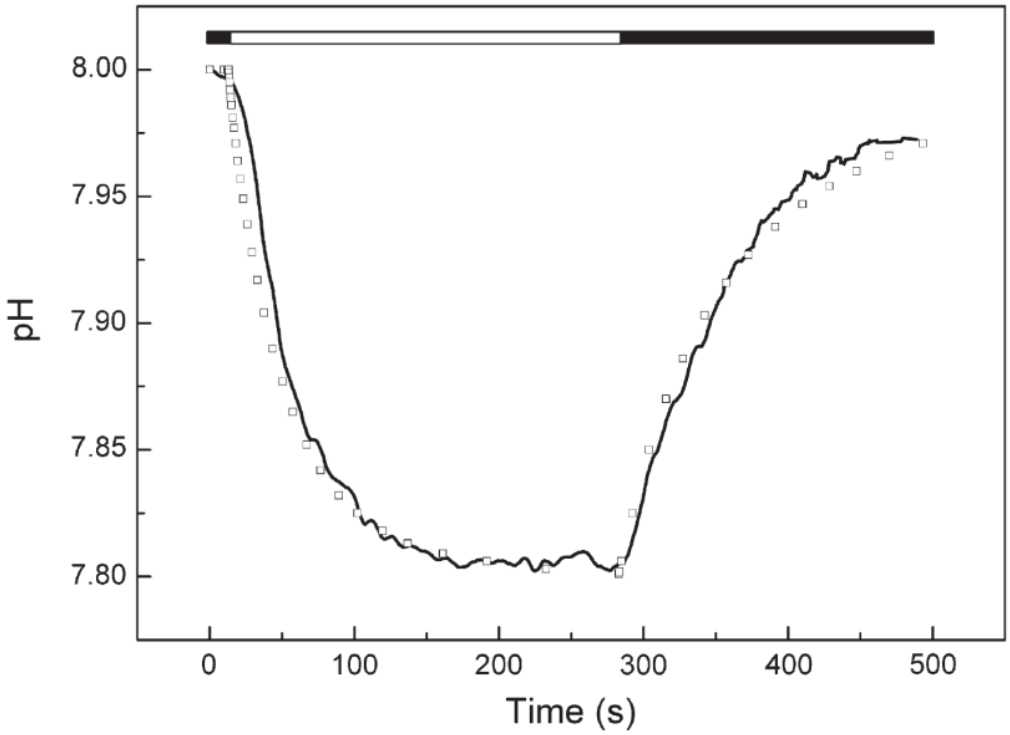

Figure 2.15: PSI-vesicles showing light induced proton concentration changes for a computational model (open squares) and experimental data (black line). The open section of the upper bar indicates illumination. (Reproduced with permission [54].)

References

[2] Olaf S Andersen and Roger E Koeppe. "Bilayer Thickness and Membrane Protein Function: An Energetic Perspective". In: *Annual Review of Biophysics and Biomolecular Structure* 36.1 (2007), pp. 107–130.

[3] Adrian Badura et al. "Photocurrent generation by photosystem 1 integrated in crosslinked redox hydrogels". In: *Energy and Environmental Science* 4.7 (2011), pp. 2435–2440.

[4] David R. Baker et al. "Comparative photoactivity and stability of isolated cyanobacterial monomeric and trimeric photosystem i". In: *Journal of Physical Chemistry B* 118.10 (2014), pp. 2703–2711.

[5] Pavol Balgavý et al. "Bilayer thickness and lipid interface area in unilamellar extruded 1,2-diacylphosphatidylcholine liposomes: A small-angle neutron scattering study". In: *Biochimica et Biophysica Acta - Biomembranes* 1512.1 (2001), pp. 40–52.

[6] Denice C. Bay and Raymond J. Turner. "Membrane composition influences the topology bias of bacterial integral membrane proteins". In: *Biochimica et Biophysica Acta - Biomembranes* 1828.2 (2013), pp. 260–270.

[7] Jeremy Berg, John L Tymoczko, and Lubert Stryer. *Biochemistry*. 6th ed. New York: W.H. Freeman and Company, 2006.

[8] H.M. Berman et al. "The Protein Data Bank". In: *Nucleic Acids Research* 28 (2000), pp. 235–242.

[9] E.J. Boekema et al. "Refined analysis of the trimeric structure of the isolated Photosystem I complex from the thermophilic cyanobacterium Synechococcus sp." In: *Biochimica et Biophysica Acta* 974 (1989), pp. 81–87.

[10] Klaus Brettel and Winfried Leibl. "Electron transfer in photosystem I". In: *Biochimica et Biophysica Acta* 1507 (2001), pp. 100–114.

[11] Parag R Chitnis. "Photosystem I: Function and Physiology". In: *Annual Review of Plant Physiology and Plant Molecular Biology* 52 (2001), pp. 593–626.

[12] C. S. Chong and Konrad Colbow. "Light scattering and turbidity measurements on lipid vesicles". In: *BBA - Biomembranes* 436 (1976), pp. 260–282.

[13] Peter N. Ciesielski et al. "Enhanced photocurrent production by Photosystem I multilayer assemblies". In: *Advanced Functional Materials* 20.23 (2010), pp. 4048–4054.

[14] J Cladera et al. "Functional reconstitution of Photosystem I reaction center from cyanobacterium Synechocystis sp PCC 6803 into liposome using a new reconstitution procedure". In: *Journal of Bioenergetics and Biomembranes* 28.6 (1996), pp. 503–515.

[15] Rolan Douce, R. Barry Holtz, and Andrew A. Benson. "Isolation and properties of the envelope of Spinach Chloroplasts*". In: *the Journal of Biological Chemistry* 248.20 (1973), pp. 7215–7222.

[16] Robert C Ford and Andreas Holzenburg. "Investigation of the structure of trimeric and monomeric photosystem I reaction centre complexes". In: *The EMBO Journal* 7.8 (1988), pp. 2287–2293.

[17] Y. Gavel et al. "The 'positive-inside rule' applies to thylakoid membrane proteins". In: *FEBS Letters* 282.1 (1991), pp. 41–46.

[18] Baosheng Ge et al. "Designer Amphiphilic Short Peptides Enhance Thermal Stability of Isolated Photosystem-I". In: *PLoS ONE* 5.4 (2010), pp. 1–9.

[19] Eric R. Geertsma et al. "Membrane reconstitution of ABC transporters and assays of translocator function". In: *Nature Protocols* 3.2 (2008), pp. 256–266.

[20] John H. Golbeck. *Photosystem I, The Light-Driven Plastocyanin:Ferredoxin Oxidoreductase*. Vol. 24. Springer, 2006.

[21] John H. Golbeck. "Structure and function of photosystem I". In: *Annual Review of Plant Physiology and Plant Molecular Biology* 43 (1992), pp. 293–324.

[22] Zoltan Gombos et al. "Characterization of the Fad12 mutant of Synechocystis that is defective in 12 acyl-lipid desaturase activity Zoltan". In: *Biochimica et Biophysica Acta* 1299 (1996), pp. 117–123.

[23] Pavlo I. Gordiichuk et al. "Solid-state biophotovoltaic cells containing photosystem i". In: *Advanced Materials* 26.28 (2014), pp. 4863–4869.

[25] Ingo Grotjohann and Petra Fromme. "Structure of cyanobacterial Photosystem I". In: *Photosynthesis Research* 85.1 (2005), pp. 51–72.

[26] Darlene Gunther et al. "Pueraria lobata (Kudzu) Photosystem I Improves the Photoelectrochemical Performance of Silicon". In: *Industrial Biotechnology* 9.1 (2013), pp. 37–41.

[27] Bradley J Harris, Xiaolin Cheng, and Paul Frymier. "All-Atom Molecular Dynamics Simulation of a Photosystem". In: *Journal of Physical Chemistry B* 118 (2014), pp. 11633–11645.

[28] Helmut Heller, Michael Schaefer, and Klaus Schulten. "Molecular Dynamics Simulation of Bilayer of 200 Lipids in the Gel and in the Liquid-Crystal Phases". In: *Journal of Physical Chemistry* 97 (1993), pp. 8343–8360.

[29] Satoshi Hoshina and Shigeru Itoh. "Characterization of Photosystem I Chlorophyll-Protein Complexes Reconstituted into Phosphatidylcholine Liposomes". In: *Plant and Cell Physiology* 28.4 (1987), pp. 599–609.

[30] Satoshi Hoshina, Prasanna Mohanty, and David C Fork. "Temperature dependent changes in absorption and fluorscence properties of the cyanobacterium Anacystis nidulans". In: *Photosynthesis Research* 5 (1984), pp. 347–360.

[31] Masaki Ihara et al. "Light-driven Hydrogen Production by a Hybrid Complex of a [NiFe]-Hydrogenase and the Cyanobacterial Photosystem I". In: *Photochemistry and Photobiology* 82.3 (2006), p. 676.

[32] Ifeyinwa J. Iwuchukwu et al. "Self-organized photosynthetic nanoparticle for cell-free hydrogen production". In: *Nature Nanotechnology* 5 (2010), pp. 73–79.

[33] Patrick Jordan et al. "Three-dimensional structure of cyanobacterial photosystem I at 2.5Å resolution". In: *Nature* 411.6840 (2001), pp. 909–917.

[34] Sook Heun Kim et al. "Effect of sonication and freezing-thawing on the aggregate size and dynamic surface tension of aqueous DPPC dispersions". In: *Journal of Colloid and Interface Science* 311.1 (2007), pp. 217–227.

[35] Jan Knol, Klaas Sjollema, and Bert Poolman. “Detergent-mediated reconstitution of membrane proteins”. In: *Biochemistry* 37 (1998), pp. 16410–16415.

[36] Shuhei Koeda et al. “Application of peptide gemini surfactants as novel solubilization surfactants for Photosystems i and II of cyanobacteria”. In: *Langmuir* 29 (2013), pp. 11667–11680.

[37] Andrey A Kondrashin, Vitaly D Samuilov, and Vladimir P Skulachev. “Reconstitution of Biological of Electric Current Molecular Generators”. In: *Journal Biological Chemistry* 217.22 (1976), pp. 7066–7071.

[38] Tim Kothe et al. “Engineered electron-transfer chain in photosystem 1 based photocathodes outperforms electron-transfer rates in natural photosynthesis”. In: *Chemistry - A European Journal* 20.35 (2014), pp. 11029–11034.

[39] Henning Krassen et al. “Photosynthetic hydrogen production by a hybrid complex of photosystem I and [NiFe]-hydrogenase”. In: *ACS Nano* 3.12 (2009), pp. 4055–4061.

[40] Danilo D. Lasic. *Liposomes in Gene Delivery*. 1st ed. CRC Press, 1997.

[41] Rosemary K Le. “Photosystem I-Based Applications for the Photo-catalyzed Production of Hydrogen and Electricity”. In: *Dissertation* (2014).

[42] Rosemary K. Le et al. “Sortase-mediated ligation of PsaE-modified Photosystem I from Synechocystis sp. PCC 6803 to a conductive surface for enhanced photocurrent production on a gold electrode”. In: *Langmuir* 31.3 (2015), pp. 1180–1188.

[43] Gabriel Leblanc et al. “Enhanced photocurrents of photosystem i films on p-doped silicon”. In: *Advanced Materials* 24.44 (2012), pp. 5959–5962.

[44] Dov Lichtenberg, Hasna Ahyayauch, and Félix M. Goñi. “The mechanism of detergent solubilization of lipid bilayers”. In: *Biophysical Journal* 105.2 (2013), pp. 289–299.

[45] Dov Lichtenberg et al. “Detergent solubilization of lipid bilayers: A balance of driving forces”. In: *Trends in Biochemical Sciences* 38.2 (2013), pp. 85–93.

[46] C. E. Lubner et al. “Solar hydrogen-producing bionanodevice outperforms natural photosynthesis”. In: *Proceedings of the National Academy of Sciences* 108.52 (2011), pp. 20988–20991.

[47] Amy K. Manocchi et al. “Photocurrent generation from surface assembled Photosystem I on alkanethiol modified electrodes”. In: *Langmuir* 29.7 (2013), pp. 2412–2419.

[48] L. Mendiola-Morgenthaler, W Eichenberger, and A Boschetti. “Isolation of chloroplast envelopes from Chlamydomonas. Lipid and polypeptide composition”. In: *Plant Science* 41 (1985), pp. 97–104.

[49] Tajib Mirzabekov et al. “Paramagnetic proteoliposomes containing a pure, native, and oriented seven-transmembrane segment protein, CCR5”. In: *Nature Biotechnology* 18.6 (2000), pp. 649–654.

[50] Peter Mitchell. “Chemiosmotic coupling in oxidative and photosynthetic phosphorylation”. In: *Biological Reviews* (1966).

[51] Dibyendu Mukherjee et al. “Controlling the morphology of Photosystem I assembly on thiol-activated Au substrates”. In: *Langmuir* 26.20 (2010), pp. 16048–16054.

[52] Ryan C. Oliver et al. “Dependence of micelle size and shape on detergent alkyl chain length and head group”. In: *PLoS ONE* 8.5 (2013), pp. 1–10.

[53] Gabriele Orlich and Gunter Hauska. “Reconstitution of Photosynthetic Energy Conservation: I. Proton Movements in Liposomes Containing Reaction Center of Photosystem I from Spinach Chloroplasts”. In: *European Journal of Biochemistry* 111 (1980), pp. 525–533.

[54] Cristian Pablo Pennisi, Elias Greenbaum, and Ken Yoshida. “Analysis of light-induced transmembrane ion gradients and membrane potential in Photosystem I proteoliposomes”. In: *Biophysical Chemistry* 146.1 (2010), pp. 13–24.

[55] Shuo Qian and William T. Heller. “Peptide-induced asymmetric distribution of charged lipids in a vesicle bilayer revealed by small-angle neutron scattering”. In: *Journal of Physical Chemistry B* 115.32 (2011), pp. 9831–9837.

[56] Jean Louis Rigaud, Bruno Pitard, and Daniel Levy. “Reconstitution of membrane proteins into liposomes: application to energy-transducing membrane proteins”. In: *BBA - Bioenergetics* 1231.3 (1995), pp. 223–246.

[57] Jean-Louis Rigaud et al. "Detergent removal by Bio-Beads". In: *European Biophysics Journal* 27 (1998), pp. 305–319.

[58] Kenneth A. Rubinson et al. "Structure determination of functional membrane proteins using small-angle neutron scattering (SANS) with small, mixed-lipid liposomes: Native beef heart mitochondrial cytochrome c oxidase forms dimers". In: *Protein Journal* 32.1 (2013), pp. 27–38.

[59] Patrick O. Saboe et al. "Two-dimensional protein crystals for solar energy conversion". In: *Advanced Materials* 26.41 (2014), pp. 7064–7069.

[60] Tsuyoshi Sasaki et al. "Characterization of Photosystem I Reaction Center Complex Reconstituted Into Phosphatidylcholine Liposomes; Effect of Proteolytic Enzymes on the Reaction Center Proteins". In: *Photosynthesis: Mechanisms and Effects*. Dordrecht: Springer Netherlands, 1998, pp. 619–622.

[61] Dmitri Satsoura et al. "Interaction of the full-length Bax protein with biomimetic mitochondrial liposomes: A small-angle neutron scattering and fluorescence study". In: *Biochimica et Biophysica Acta - Biomembranes* 1818.3 (2012), pp. 384–401.

[62] Alexander Schwarze et al. "Requirements for construction of a functional hybrid complex of photosystem I and [NiFe]-hydrogenase". In: *Applied and Environmental Microbiology* 76.8 (2010), pp. 2641–2651.

[63] Annela M. Seddon, Paul Curnow, and Paula J. Booth. "Membrane proteins, lipids and detergents: not just a soap opera". In: *Biochimica et Biophysica Acta - Biomembranes* 1666.1-2 (2004), pp. 105–117.

[64] Hila Toporik et al. "Large photovoltages generated by plant photosystem i crystals". In: *Advanced Materials* 24.22 (2012), pp. 2988–2991.

[65] M Angeles Urbaneja et al. "Detergent solubilization of phospholipid vesicle. Effect of electric charge." In: *The Biochemical journal* 270.2 (1990), pp. 305–308.

[66] Ilya R Vassiliev, Mikhail L Antonkine, and John H Golbeck. "Iron-sulfur clusters in type I reaction centers". In: *Biochimica et Biophysica Acta* 1507 (2001), pp. 139–160.

[67] Alice Verchère et al. “Reconstitution of membrane proteins in liposomes”. In: *Methods in Enzymology* 372.2000 (2003), pp. 65–86.

[68] Erik Wallin and Gunnar von Heijne. “Genome-wide analysis of integral membrane proteins from eubacterial, archaean, and eukaryotic organisms”. In: *Protein Science* 7 (1998), pp. 1029–1038.

[69] Lina Wang et al. “Functional reconstitution of Staphylococcus aureus truncated AgrC Histidine kinase in a model membrane system”. In: *PLoS ONE* 8.11 (2013), pp. 1–12.

[70] Xiaoqiang Wang et al. “Solubilization and Stabilization of Isolated Photosystem I Complex with Lipopeptide Detergents”. In: *PLoS ONE* 8.9 (2013), pp. 1–12.

[71] Zhenle Yang et al. “Photochemical activities of plant photosystem I particles reconstituted into phosphatidylglycerol liposomes”. In: *Journal of Photochemistry and Photobiology B: Biology* 78.2 (2005), pp. 125–134.

[72] A L Zilber and R Malkin. “Organization and topology of photosystem I subunits.” In: *Plant Physiology* 99.3 (1992), pp. 901–911.

Chapter 3

Preparation of Functional PSI with a Sortase Ligation Tag

Abstract

Photosystem I (PSI) is of interest in a variety of renewable energy applications. One such is conjugating PSI to hydrogenase for hydrogen production across a synthetic membrane. The conjugation utilizes a mutant PSI with a C-terminus peptide sequence of LPETG on the stromal subunit, PsaE from *Synechocystis* PCC 6803. Here, sortase A ligates the LPETG tag on PSI to a triglycine (GGG) peptide sequence on GFP, which is used as a surrogate to hydrogenase in order to demonstrate the presence and accessibility of the LPETG tag on PSI. The rate of re-reduction of PSI with the sortase ligation tag has been measured using laser flash photolysis in the presence of common redox mediators. Furthermore, a structural characterization of the mutant and wild type PSI was performed to verify that the point mutation and purification procedure maintained the structural integrity of the protein complex.

3.1 Introduction

Renewable sources of electrical and chemical energy are necessary for continued industrial and cultural growth. Fortunately, nature has provided a robust protein, called PSI, that captures light energy and stores it in chemical bonds at a quantum efficiency nearing unity [18]. PSI is part of the photosynthesis system in plants and algae. The protein has been used with success to catalyze light conversion by many researchers in a variety of systems [15, 3, 13, 10, 6, 21]. In one such system, a peripheral subunit of PSI, PsaE, has been tagged with a peptide sequence of LPETG on the C-terminus [12]. The modification enables covalent biding to a glycine tagged unit. Le *et al.* developed this mutant and used it to successfully orient PSI trimers onto a gold electrode, thereby uniformly directing light driven current flow [12]. Use of the LPETG-peptide sequence on PSI in liposomes has been proposed for the direct production of hydrogen across the membrane by attachment of a hydrogenase enzyme to the PsaE subunit. In this work, the successful conjugation of GGG-tagged green fluorescent protein (GFP) to LPETG-PsaE PSI has been demonstrated. Readily available GGG-GFP was used as a surrogate to a GGG-hydrogenase protein. In performing this ligation, it was demonstrated that soluble protein-protein ligation is possible with mutant PSI. The kinetics of re-reduction of the PSI mutant were also measured by using laser flash photolysis at increasing concentrations of the sacrificial donor. In this chapter, the structural integrity of mutant PSI has been characterized and compared with either published or found results of wild type PSI. Circular dichroism saw similar purified protein folding between the mutant and the protein database structure. Additionally, spectroscopy showed similar chlorophyll and protein absorption and fluorescent peaks for the mutant protein. These experiments show that mutant PSI maintains structural integrity and is can be conjugated with another soluble protein.

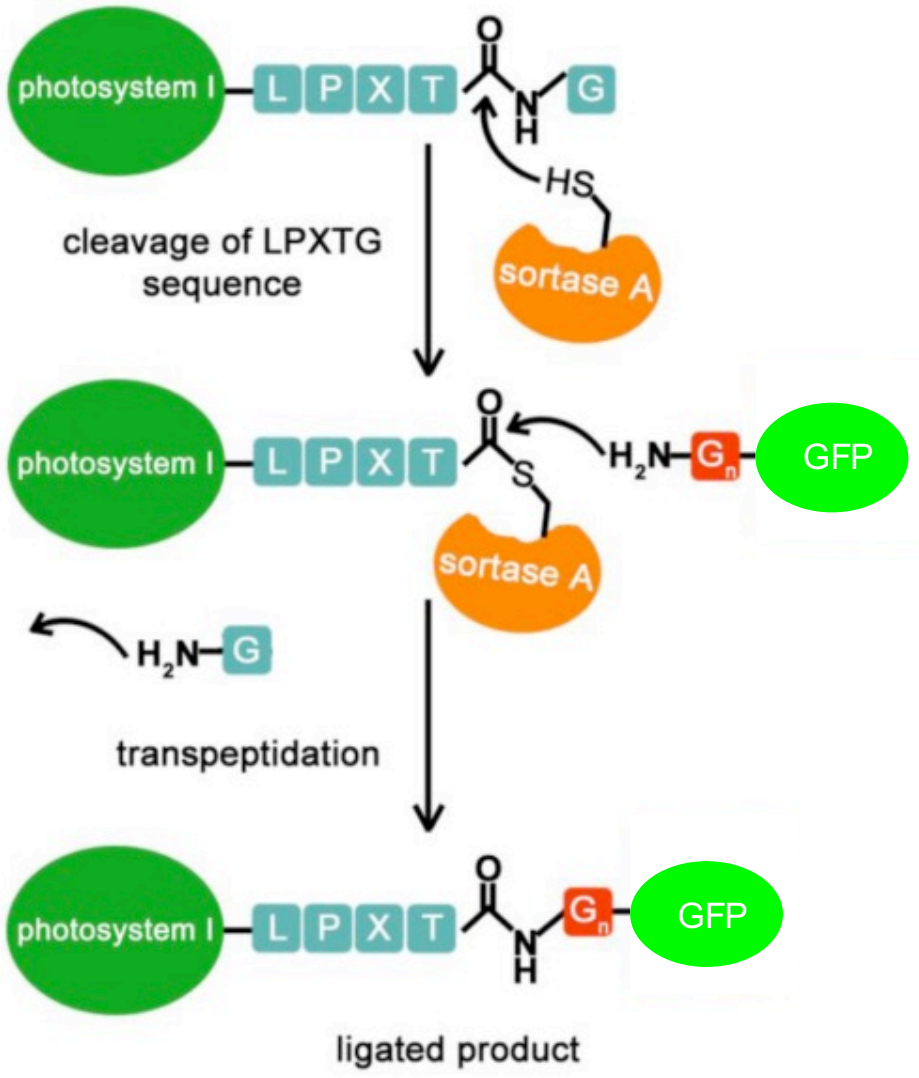

Figure 3.1: Schematic demonstrating the ligation mechanism of PSI modified with an LPXTG termini to a glycine decorated gold surface using sortase A enzyme. Figure adapted from Le *et al.* [12]

3.2 Materials and Methods

3.2.1 Purification of Modified PSI from *Synechocystis* sp. PCC 6803

Model cyanobacterium *Synechocystis* sp. PCC 6803 (ATCC: 27184) by Le *et. al* with PSI carrying a modified LPETG-6xHis peptide sequence on the c-terminus of the PsaE subunit was grown in a selective 50 μg/mL kanamycin BG-11 media [12] . Growth was performed in a New Brunswick BioFlow3000 bioreactor (Eppendorf, Inc.) at 30 °C under 350 rpm impeller agitation, a 150 mL/min airflow rate, and 25 $\mu E/m^2/s$ illumination with fluorescent lights. Cells were harvested, pelleted, and frozen at -80 °C prior to PSI extraction. PSI was extracted from the mutant psaE 6803 strain following modified protocols [12, 9, 11]. 10 g of frozen cells were resuspended by vortex mixing in buffer A (50 mM MES-NaOH, pH 6.0; 10 mM $MgCl_2$; 5 mM $CaCl_2$; 25 % v/v glycerol) to a final chlorophyll a (Chl$a$) concentration at 1 mg/mL.

Chl$a$ was determined by methanol extraction by mixing resuspended cells with 90 % methanol in a 1:10 dilution. The cell-methanol mixture was incubated for 2 min in a 60 °C water bath, then microcentrifuged at 21,000 xg for 1 min. The supernatant was carefully transferred to a 1 mL quartz cuvette, and the absorbance was measured at 665 nm with a UV-Vis spectrophotometer. The concentration in μg/mL of (Chl$a$) was determined to be 13.9 times Abs_{665} using an extinction coefficient at 72 mg/L in methanol [8].

Cells were incubated on ice with HALT protease inhibitor cocktail designed for his-tagged proteins (Thermo Scientific) at 100 μL HALT per 10 mL cell suspension for 1 hour. A French press was used to lyse cells in three cycles at 25,000 psi. The cell lysate was collected on ice and centrifuged at 19,000 xg for 30 min at 4 °C. The cell lysate pellet was retained and resuspended in buffer A and 1 % (w/v) n-dodecyl-β-D-maltoside (DDM) on a platform rocker for 30 min at 4 °C. The solubilized membrane fraction was centrifuged at 15,000 xg for 30 min. The supernatant was equilibrated with buffer A, pH 7.8, 0.04 % (w/v) DDM, 5 mM histidine, and a HisPur Cobalt (Thermo Scientific) column was prepared by equilibrating with buffer A, pH 7.8, 0.04 % (w/v) DDM, 5 mM histidine.

The equilibrated supernatant containing solubilized membrane proteins and his-tagged PSI was applied at 5 mL of resin bed per 20 mL of supernatant. The flow-through was reapplied, then the column was washed with nine bed volumes until UV-vis measurements at 280 nm reached a baseline. The protein was eluted from the column using buffer A, pH 7.8, 0.04 % (w/v) DDM, 100 mM histidine. The elution fractions were pooled and dialyzed with 6-8000 MWCO Spectra/Por dialysis membrane tubing (Spectrum Laboratories, Inc.) in 2 L buffer A with 0.04 % (w/v) DDM with gentle stirring for 2 h, twice, and overnight at 4 °C.

3.2.2 Sortase I Purification and Ligation

The enzyme Sortase A with a 6xHis tag was expressed and purified as described by Levery *et al.* [14]. BL21 DE3 *E. coli* cells were transformed with the pHTT27 vector (gift from Dr. Olaf Scheewing at the University of Chicago to Dr. Eric Boder) and expressed with 1 mM isopropyl-β-D-1- thiogalactopyranoside (IPTG) for 4 hours after reaching an OD_{600}. Cells were pelleted and frozen overnight at -20 °C, then B-per reagent from Thermo Scientific was used to isolate the soluble protein fraction. Sortase was purified from the lysate using His-Pur^{TM} resin from Thermo Scientific^{TM}. A buffer exchange was performed with the protein fractions into 50 mM Tris, 150 mM NaCl, pH 8 using Spectra/Por 6-8 kDa molecular weight cutoff, 40 mm width dialysis tubing (SpectrumLabs, part no. 132660), replacing the buffer twice after two hours, followed by overnight dialysis.

Sortase enzyme was used to ligate GFP with a GGG peptide sequence on the N-terminus (GGG-GFP) (a gift from Dr. Eric Boder's lab) to a GFP with an LPETG peptide sequence on the C-terminus (LPETG-GFP) (also a gift from Dr. Eric Boder's lab) or PSI with an LPETG peptide sequence on the C-terminus of the PsaE subunit (LPETG-PsaE PSI) as described by Levary *et al.* [14]. The reaction occurred by mixing equimolar ratios of each peptide sequence, i.e., 3 μM GGG-GFP and 1 μM LPETG-tagged PsaE in trimeric PSI, with 1.2 to 14.4 μM sortase, 60 mM $CaCl_2$ in tris-buffered saline (50 mM Tris-Cl, pH 7.6;150 mM NaCl). The reaction mixture was incubated 4 hours at 42 °C on an orbitor.

3.2.3 Protein Denaturing Electrophoresis

PSI trimers in 0.04 % DDM buffer were mixed at a 1-to-1 ratio with loading buffer (100 mM Tris pH 6.8, 15 % glycerol, 5 %β-mercaptoethanol, 2 % sodium dodecyl sulfate, dot Orange-G). Prepared samples were vortexed and placed into a heating block at 42°C for 30 min. Prior to loading, samples were centrifuged at 1000 x g for 1 min. A 4-12 % Bis-Tris SDS-PAGE electrophoresis gel was prepared according to package protocol with 1X MES running buffer in the inner and outer chambers. 10 μL of prepared sample was loaded into each lane well. Additionally, 6 μL protein standard marker was used. Electrophoresis was run at 200 V for 45 minutes. A quick Coomassie staining protocol was used. The stain was prepared as 0.1 % Coomassie R-250, 10 % acetic acid, 40 % methanol. The destain solution was prepared as 20 % methanol, 10 % acetic acid. After electrophoresis, the gel was removed from the cassette and covered with stain. It was microwaved for 40 s and cooled for 5 min on an orbitor at 4°C. The gel was rinsed, then covered with a destain solution, microwaved for 40 s and cooled for 5 min on an orbitor at 4°C with a knotted Kimwipe®. The destain solution was discarded, refreshed, and allowed to sit 3-4 hour until there was a clear background, also in the presence of a Kimwipe®.

3.2.4 Structural Characterization of PSI

To confirm growth and purification of LPETG-PsaE PSI maintained the structural integrity similar to that of WT PSI also from *Synechocystis* sp. PCC 6803 absorbance spectroscopy, dynamic light scattering, cryo-fluoremetry, and circular dichroism were performed on both PSI samples. WT PSI was obtained from lab stocks. The absorbance spectrum of LPETG-PsaE PSI and WT PSI purification products were recorded using a Thermo-Scientific NanoDrop 2000C spectrophotometer at room temperature. The size distribution of LPETG-PsaE PSI and WT PSI purification products were recorded using a Wyatt Technology DynaPro NanoStar fixed angle dynamic light scattering instrument at 20 °C. The data was fit with the standard isotropic sphere model at optimal resolution.

Steady-state fluorescence emission spectra of purified PSI at 77K were measured with a Hitachi 850 fluorescence spectrophotometer (Hitachi, Japan). Protein was dark adapted

to promote the reduced stated and diluted to 6 μg Chl/mL prior to spectra measurements. Samples were frozen in a liquid nitrogen Dewar vessel and the emission spectra were recorded from 650 to 800 nm with excitation at 440 nm.

The secondary structure of PSI was observed using an Aviv Circular Dichroism spectrometer, Model 202. Spectra were collected at room temperature in a 1.00 mm quartz cuvette, cleaned with methanol. Wavelengths 190-260 nm were recorded for 6 scans with a 1 nm step every second. PSI samples were prepared in 10 mM potassium phosphate buffer, pH 7.8, 0.04 % DDM.

3.2.5 Laser Flash Photolysis

PSI activity was measured on a custom-built pump-probe spectrometer similar to that of Xu *et al.* [22] and depicted in Figure 3.2. The absorbance of PSI was measured by using a laser at 830 nm, excited by an Nd:Yag laser fitted with a frequency doubler to yield an excitation beam at 532 nm. At this wavelength, the change in absorbance was measured before and after the excitation laser pulse. Samples were prepared with 0.2 uM LPETG-PaE PSI, 50 mM ascorbate (Asc), 50 mM methyl viologen (MV), and 2.9 - 8.6 mM 2,6-dichlorophenolindophenol (DCPIP) in 0.04% DDM. A single-turnover excitation in PSI was triggered with a Spectra Physics Q-switched Nd:YAG laser with the frequency doubled to 532 nm to provide a saturating laser flash with a pulse width of 6–9 ns. A probe beam was emitted from a Newport 150 mW diode and filtered to 705 nm, then split to pass through the sample and to a reference detector. Neutral density filters limited the laser power that reached the sample and reference detectors. Data sets were averaged 8–32 times with 5 s between each laser flash. Signals were detected with an OSI Optoelectronics PIN-10D photodiode and were amplified using a Femto DHPCA-100 high speed variable gain amplifier. Signals were digitized and recorded using a Tektronix 3012B oscilloscope and a LabView program written in-house. Data sets were fit with a 1^{st} order exponential model.

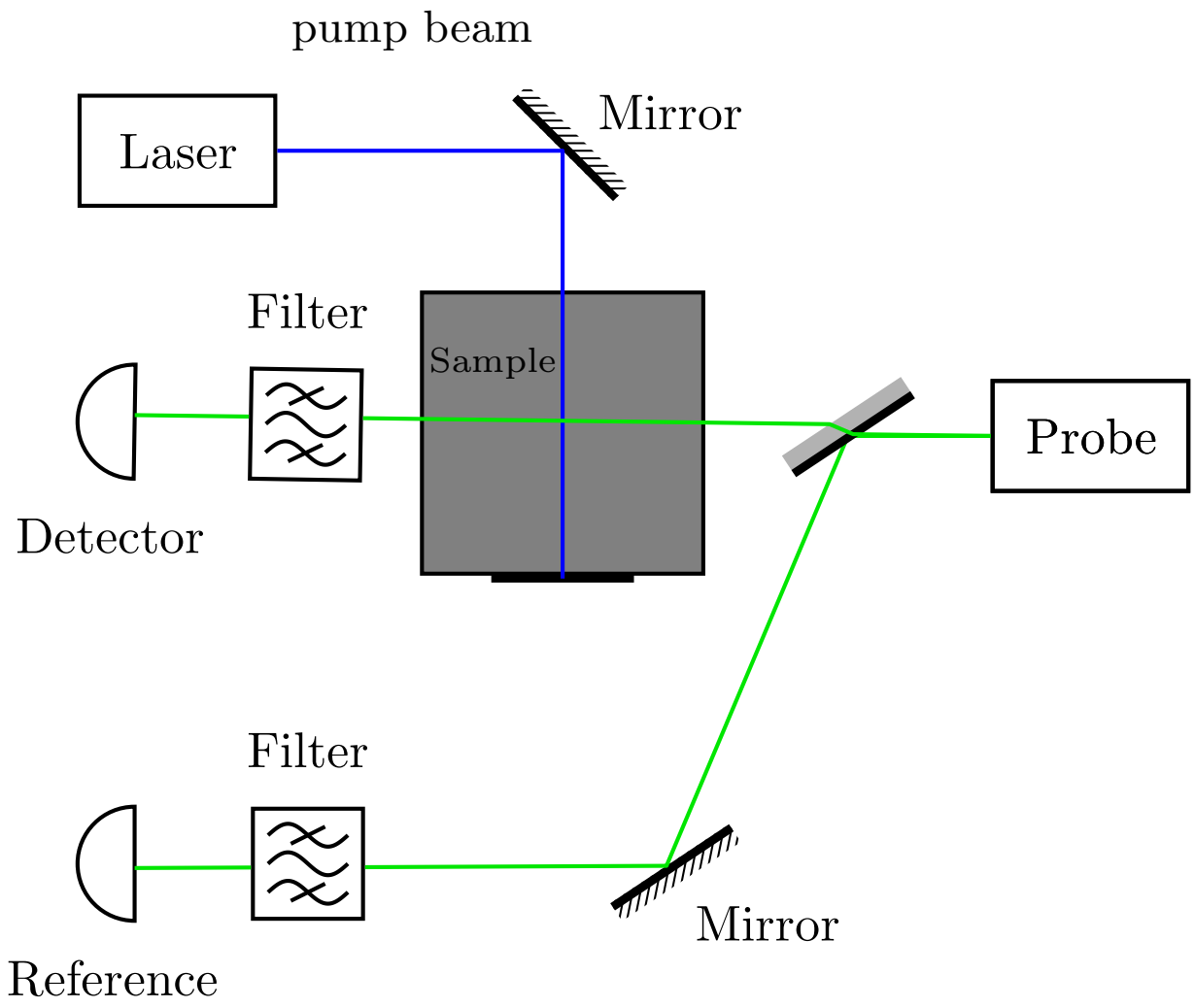

Figure 3.2: Schematic of a custom-made laser-flash photolysis set-up.

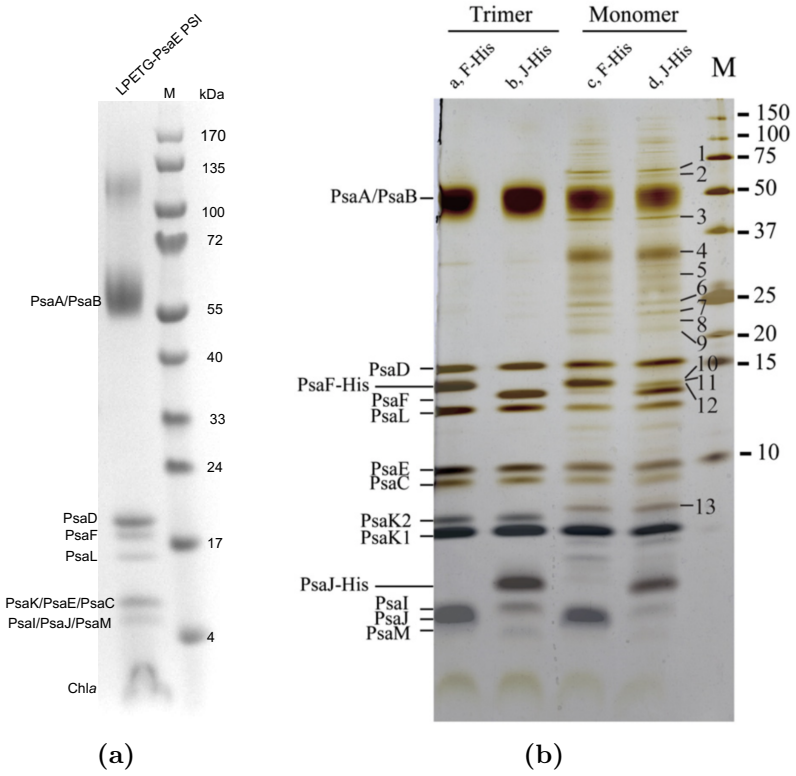

(a) **(b)**

Figure 3.3: Protein subunits of (a) purified LPETG-PsaE PSI compared with (b) his-tagged PsaF and PsaJ by Kubota *et al.* [11]. All PSI is from *Synechocystis* PCC 6803.

3.3 Results and Discussion

3.3.1 Protein Subunits and LPETG-tag Accessibility

Denaturing protein gels were used to verify the preparation procedure of functional PSI mutant. Figure 3.3(a) shows LPETG-PsaE PSI purified using a histidine binding column, as described in Section 3.2.1. Lanes 1 and 2 contain 0.3 μM and 0.6 μM PSI in 0.04 % (w/v) DDM. Two concentrations were used to observe any contaminant and lower molecular weight subunits. Lane 3 is a molecular weight marker with the key written to the right. The molecular weights of the bands are compared with Kubota *et al.* [11]. In both gels, PsaA and PsaB are indicated by bands near 50 kDa, and the smaller subunits are primarily distributed less than 24 kDa as labeled.

Figure 3.4 is a denaturing protein gel of mutant PSI demonstrating functional accessibility of the LPETG peptide sequence on the PsaE subunit. A band at 40 kDa in lanes 6, 7, and

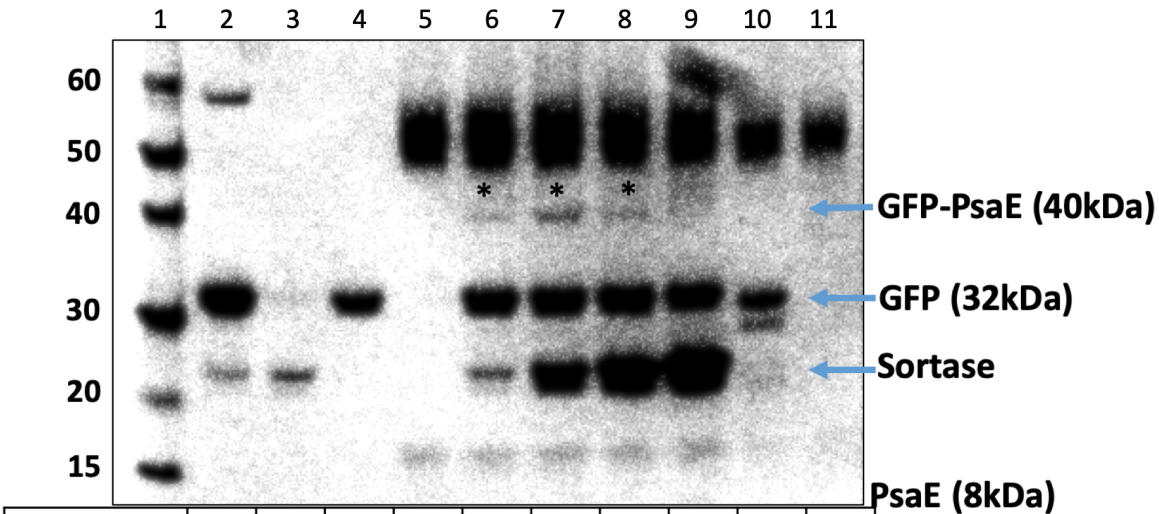

GGG-GFP	+	-	+	-	+	+	+	+	+	-
LPETG-GFP	+	-	-	-	-	-	-	-	-	-
Mut. PSI	-	-	-	+	+	+	+	+	-	-
WT PSI	-	-	-	-	-	-	-	-	+	+
Sortase	+	+	-	-	+	+	+	+	+	-

Figure 3.4: Denaturing protein gel demonstrating ligation of the LPETG-PsaE subunit of PSI to GGG-GFP using the enzyme, sortase.

8 demonstrates that there was a ligation of 32 kDa GGG-GFP and 8 kDa LPETG-PsaE at 0.2, 0.6, and 1.2 enzyme: reactant (E:R), respectively. Lane 2 is a sortase catalyzed ligation of LPETG-GFP to GGG-GFP. The ligation product is nearly double the weight (59 kDa) of the single GFP protein band at 30 kDa. Sortase is observed at 24 kDa. Lanes 3, 4, 5, and 11 are the single proteins, sortase, GFP, mutant PSI, and wild-type (WT) PSI, respectively. Lane 10 contains WT PSI with GGG-GFP and sortase. As would be expected, there is no ligation product. This protein gel demonstrates the ability to successfully grow and purify functionalized PSI and bind it with the corresponding peptide sequence.

3.3.2 Absorbance and Scattering Characterization of PSI

Figure 3.5 demonstrates room temperature absorbance spectrometry for purified LPETG-PsaE PSI (—) and WT PSI (—) in 0.04 % DDM. The absorbance peaks for both samples are at wavelengths of 440 nm and 680 nm with observed shoulders around 475 nm and 640 nm. These are characteristic peaks for Chl$a$ and Chl$b$ pigments in PSI [2]. These absorbance

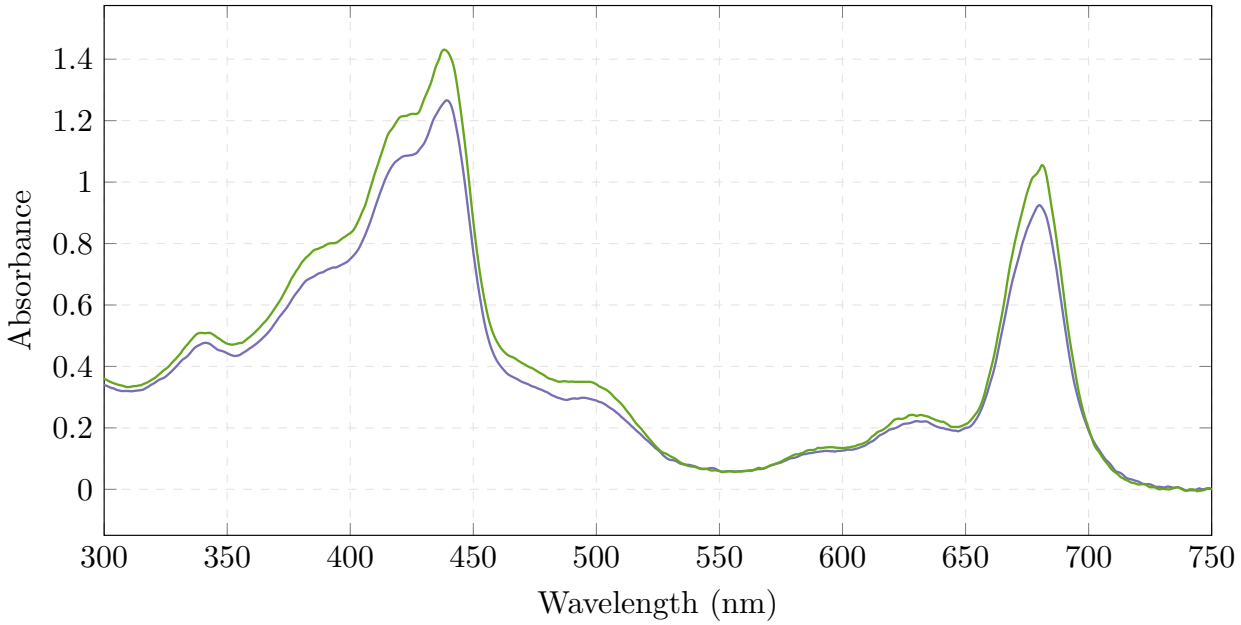

Figure 3.5: Room temperature absorbance spectrum of purified LPETG-PsaE PSI (——) and WT PSI (——) in 0.04 % DDM.

peaks indicate that LPETG-PsaE PSI has been solubilized in detergent and has maintained Chl*a* and Chl*b* association with the protein subunits. Changes to the microenvironment in PSI around either of these chlorophyll pigments would be indicated by changes in the amplitude or wavelength of the absorption peak [23]. Disassociation is indicated by a shift to a lower energy absorbance peak [24].

Figure 3.6 shows the size distribution of purified LPETG-PsaE PSI in 0.04 % DDM with an average diameter of 35 nm. This aligns with the known diameter of trimeric PSI at 22 nm, surrounded by peripheral detergent belt, around 6-7 nm in each direction [7, 19]. It is also similar to a study that found a diameter of 30 nm and a height of 9 nm for trimeric PSI solubilized in DDM[16]. Additionally, the left bins in Figure 3.6 with an average diameter of 13 nm are detergent micelles, as identified identified in Mukherjee *et al.* [16].

Figure 3.7 demonstrates low temperature fluorescence of LPETG-PsaE PSI (——) and WT PSI (——) in 0.04% DDM. Additionally, it shows that both purifications lack contamination with PSII, which fluoresces at 695 nm [20]. In both purification samples, the PSI complex fluorescence peak is at 721 nm. However, there is an unexplained shift in the peak for chlorophyll fluorescence, in which WT PSI fluoresces at 675 nm and mutant, LPETG-PsaE

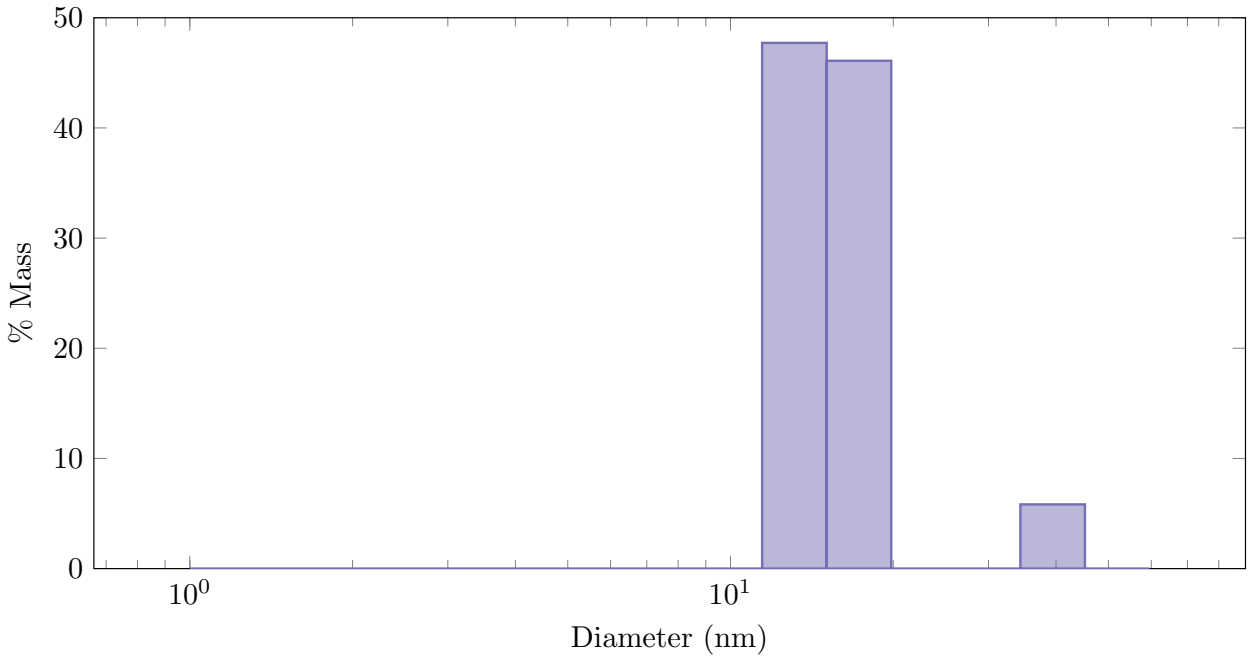

Figure 3.6: Size distribution of purified LPETG-PsaE PSI with 0.04 % DDM.

PSI fluoresces at 673 nm. PSI complexes are known to undergo a 3-5 nm blue shift in the chlorophyll association and PSI complex regions when the protein is bound to *in vitro* membranes [17]. Additionally, there is an increase in fluorescence for chlorophyll association after binding in a liposome [17]. A similar shift would be expected after incorporating PSI into liposomes as well.

3.3.3 Secondary Structure of PSI

Figure 3.8 shows the recorded data from ultraviolet circular dichroism of LPETG-PsaE PSI dilutions in order to observe mutant protein folding. α-helices span the membrane and affect chlorophyll light absorbing pigments and the electron transport chain. The Ladokhin *et al.* method was used to determine the % alpha of 0.3 μM (—), 0.03 μM (—), and 0.015 μM PSI trimer (—) were -44.6, -46.8, and -46.9, respectively. This method uses the mean residue ellipticity (θ) at 222 nm. In a membrane, the % helices have been observed to increase and simultaneously, the % disorder was observed to decrease [17]. Additionally, it possible to observed aggregation through a decrease in % helices and an increase in % disorder.

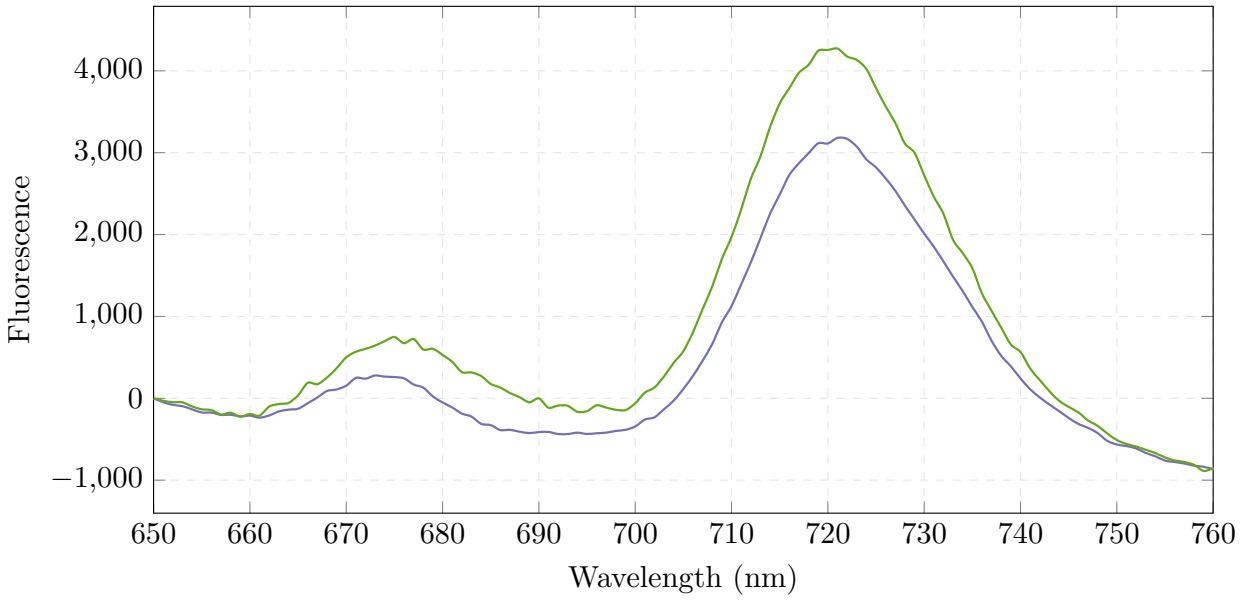

Figure 3.7: Low temperature fluorescence spectra of LPETG-PsaE PSI (——)and WT PSI (——) in 0.04% DDM.

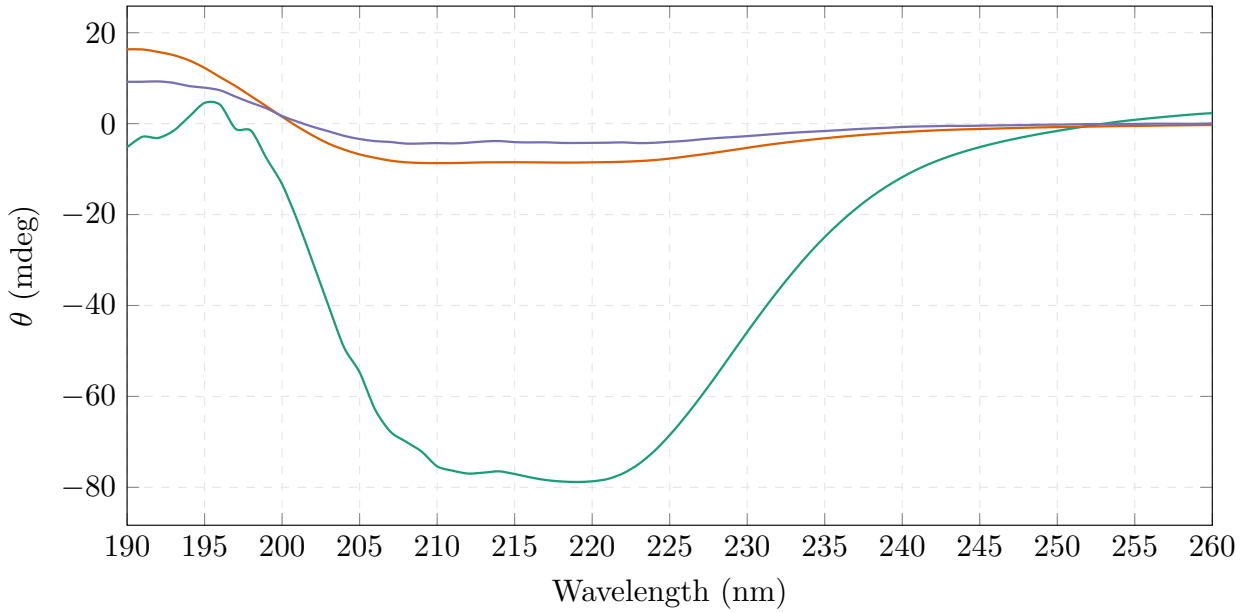

Figure 3.8: Circular dichroism spectra of LEPTG-PsaE PSI in 0.04 % DDM at 0.3 μM (——), 0.03 μM (——), and 0.015 μM PSI trimer (——). The averaged secondary structures are 46 % α helices, 18 % β sheets, and 36 % random coil.

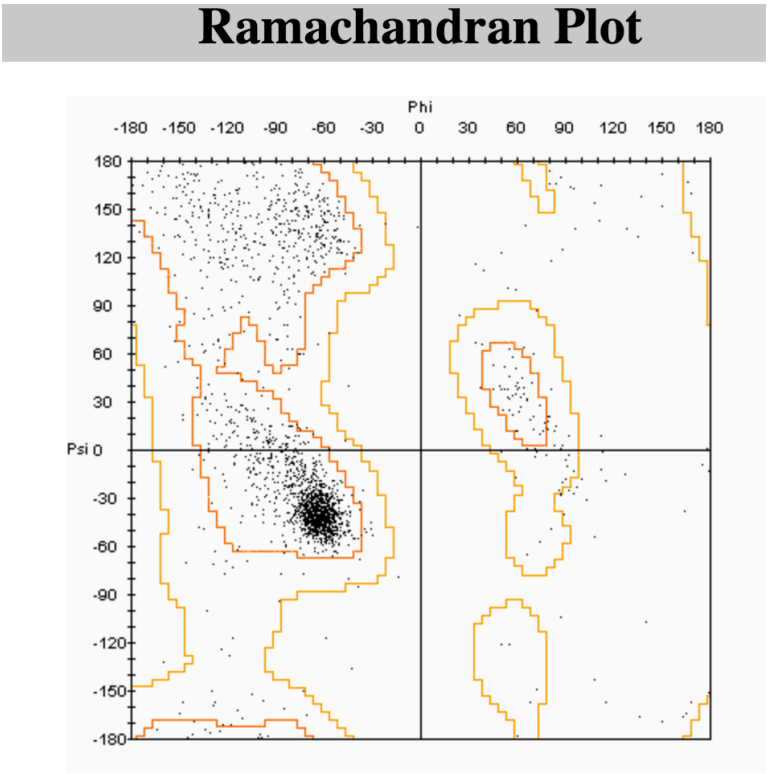

Figure 3.9: Analysis of the secondary structure of PDB 1JB0 using this method resulted in 53 % α helix, 5 % 3-1 helix, 16 % coil, 19 % turn, and 6 % strand.

Measurements closely align with a STRIDE analysis of the secondary structure solved in the protein database. STRIDE is an automatic algorithm which assigns proteins secondary structure using atomic coordinates based on hydrogen bond energy and statistically derived backbone torsion angle information [5]. With a Ramachandran plot, α helices are determined based on the pattern of hydrogen bonds between backbone amide and carboxyl groups in a string of covalently bound amino acids, which are defined by 3.6 residues per turn. Analysis of the secondary structure of PDB ID: 1JB0 [1] using this method resulted in 53 % α helix, 5 % 3-1 helix, 16 % coil, 19 % turn, and 6 % strand. Therefore, mutant PSI was within an expected range for the % α helices.

3.3.4 Re-reduction Potential of LPETG-PsaE PSI

Laser flash photolysis was used to observe the redox activity of LPETG-PsaE PSI. In PSI, P700 is a special pair of chlorophyll pigments that are photoexcited by a laser flash to an excited singlet state and is subsequently oxidized to $P700^{+}$ in the presence of an

electron acceptor, such as methyl viologen (MV). Here, the kinetics of the P700 redox state were observed by measuring changes in absorbance at 830 nm. In the presence of 2,6-dichlorophenolindophenol (DCPIP), $P700^+$ is re-reduced to P700 after photo-oxidation. This reaction is shown in Figure 3.10, in which ascorbate (Asc) is present to re-reduce DCPIP. In Figure 3.11, P700 oxidation in LPETG-PsaE PSI was induced by laser is flash at 50 μs and the change in absorbance is observed at 830 nm. The dependence of DCPIP concentration on the rate of re-reduction is observed. In all cases, DCPIP was in excess. A first order exponential describes that data and is shown with a gray dotted line. The observed rate constant for each DCPIP concentration was then shown in Figure 3.12.

The kinetics which govern donor association and electron transfer to and from P700 are described by a two-step mechanism [4] :

$$\mathrm{DCPIP^-} + \mathrm{PSI}_{ox} \overset{k_{eq}}{\rightleftharpoons} [\mathrm{DCPIP^-}...\mathrm{PSI}_{ox}] \overset{k_1}{\rightarrow} \mathrm{DCPIP} + \mathrm{PSI}_{red} \tag{3.1}$$

In the first step, there is an equilibrium reaction for association and dissociation of DCPIP with the binding site on PSI. In the second step, there is an intra-protein electron transfer within PSI. In this experiment, the DCPIP concentration for all measurement is 3 orders of magnitude greater than the concentration of PSI, and the observed rate of re-reduction linearly increases with DCPIP concentration, as seen in Figure 3.12. Thus the kinetics are described by a pseudo-first order rate constant, k_1 by the following reaction:

$$\mathrm{DCPIP^-} + \mathrm{PSI}_{ox} \overset{k_1}{\rightarrow} \mathrm{DCPIP} + \mathrm{PSI}_{red} \tag{3.2}$$

In which the rate constant can be written as:

$$\frac{d[\mathrm{PSI}]}{[\mathrm{PSI}]} = -k_1[\mathrm{DCPIP}]dt \tag{3.3}$$

And redefined using k_{obs} because the concentration of DCPIP does not significantly change as it is significantly in excess of PSI.

$$\frac{d[\mathrm{PSI}]}{[\mathrm{PSI}]} = -k_{obs}dt \tag{3.4}$$

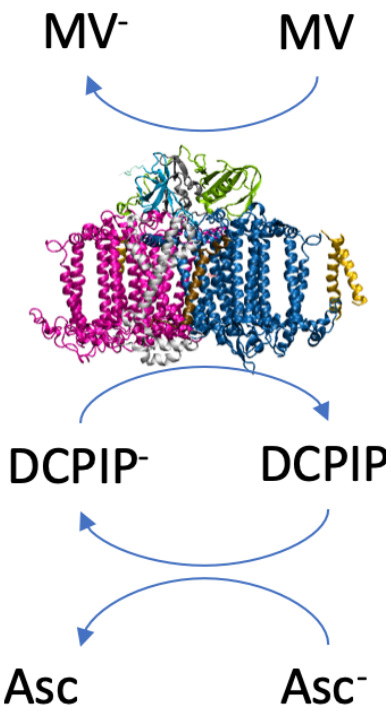

Figure 3.10: Chemical reaction for the light induced reduction and oxidation of PSI, in which the sacrificial donor 2,6-Dichlorophenolindophenol (DCPIP) is re-reduced by ascorbate (Asc), and methyl viologen (MV) accepts an electron from the stromal side of PSI

.

This can be written as

$$\frac{[\mathrm{PSI}]}{[\mathrm{PSI}_0]} = e^{-k_{obs}t} \tag{3.5}$$

And the reaction rate, k_1, for LPETG-PsaE PSI in 0.04 % DDM is $0.024\,s^{-1}$, and was found by $k_{obs}/[\mathrm{DCPIP}]$ for the linear fit in Figure 3.12. This value provides a point of comparison for PSI activity before insertion into a liposome. Previous research indicates that the k_1 would be expected to increase in a lipid bilayer [24].

3.4 Conclusions

The ability to purify mutant PSI with an LPETG peptide sequence on the PsaE subunit from *Synechocystis* PCC 6803 has been shown. The PSI protein complex had subunits with expected molecular weights, and the LPETG-tag was accessible and bound to an enzyme with the corresponding GGG peptide sequence using sortase enzyme. This was observed

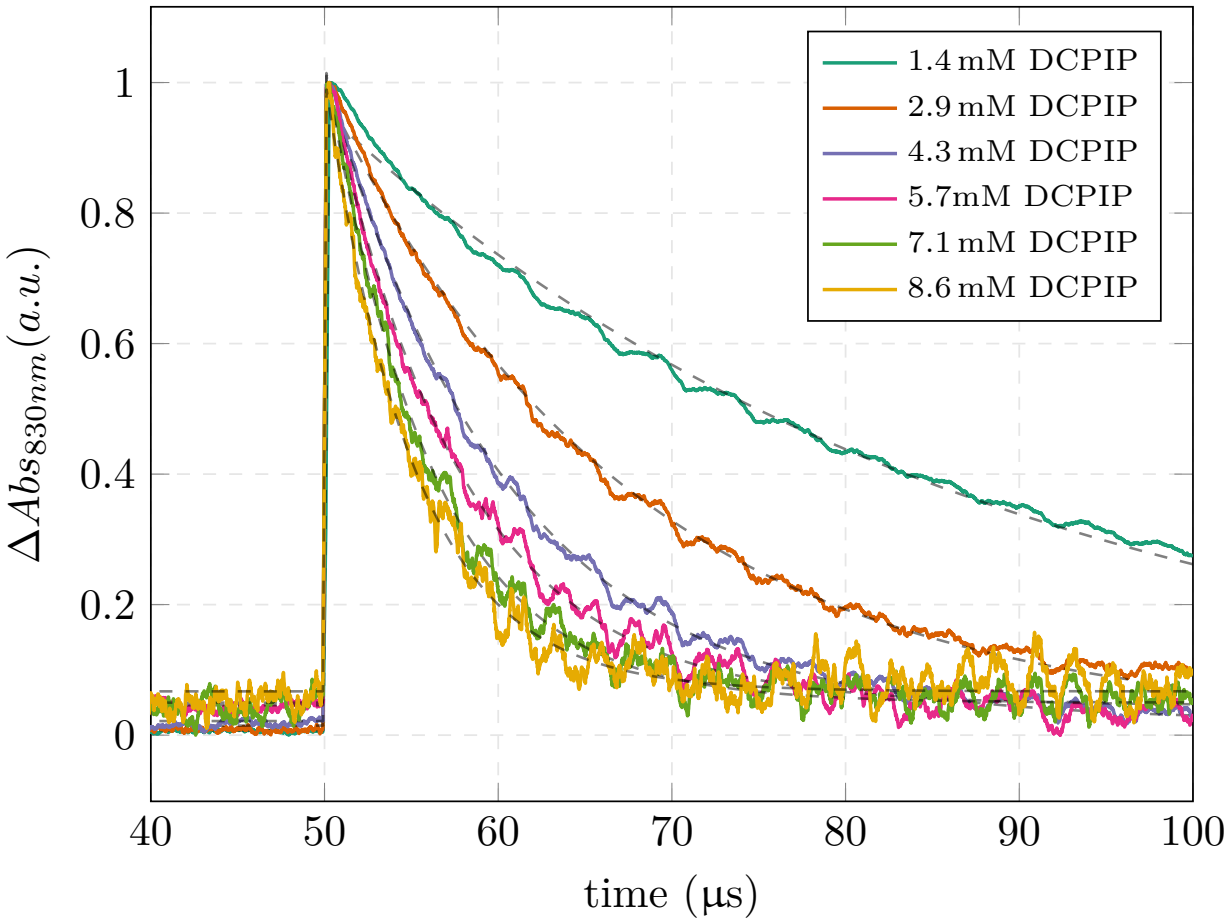

Figure 3.11: Laser flash photolysis of LPETG-PsaE PSI at varying donor (DCPIP) concentrations to observe the oxidation state of P700.

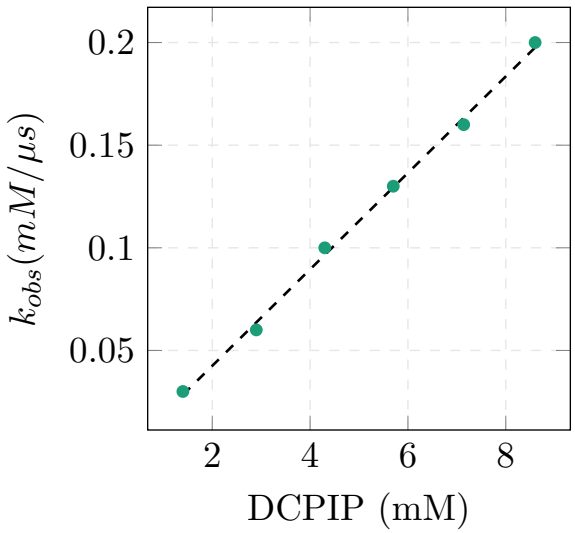

Figure 3.12: Dependence in the observed rate constants of PSI with DCPIP concentration.

by an additive molecular weight shift when attached to GGG-GFP. Further analysis of PSI structure and chlorophyll association was observed using absorbance and cryogenic fluorescence which saw little change in the absorption peaks between WT and mutant PSI. Secondary structure analysis with CD aligned closely with the predicted helices percentage from the PDB structure. These analysis demonstrated that the mutant PSI maintained the structural integrity and function of WT PSI, and the observations made here can be compared with PSI after insertion into liposomes.

References

[1] H.M. Berman et al. "The Protein Data Bank". In: *Nucleic Acids Research* 28 (2000), pp. 235–242.

[2] Stefano Caffarri et al. "A comparison between plant Photosystem I and Photosystem II architecture and functioning". In: *Current protein & peptide science* (2014).

[3] Peter N. Ciesielski et al. "Enhanced photocurrent production by Photosystem I multilayer assemblies". In: *Advanced Functional Materials* 20.23 (2010), pp. 4048–4054.

[4] Antonio Diaz et al. "Thermodynamic Study By Laser-Flash Photolysis of Plastocyanin and Cytochrome C6 Oxidation By Photosystem". In: *European Journal of Biochemistry* 222 (1994), pp. 1001–1007.

[5] Dmitrij Frishman and Patrick Argos. "Knowledge-based protein secondary structure assignment". In: *Proteins, Structure, Function, and Genetics* 23 (1995), pp. 566–579.

[6] Ludmila Frolov et al. "Fabrication of a photoelectronic device by direct chemical binding of the photosynthetic reaction center protein to metal surfaces". In: *Advanced Materials* 17 (2005), pp. 2434–2437.

[7] John H Golbeck. "Photosynthetic Reaction Centers: So little time, so much to do". In: *Photosystem I in Bioenergetics*. American Biophysical Society, 2003. Chap. 3, pp. 1–31.

[8] D. O. Hall and K. K. Rao. *Photosynthesis*. 6th ed. New York: Cambridge University Press, 1999, p. 43.

[9] Ifeyinwa J. Iwuchukwu et al. "Optimization of photosynthetic hydrogen yield from platinized photosystem i complexes using response surface methodology". In: *International Journal of Hydrogen Energy* 36 (2011), pp. 11684–11692.

[10] Ifeyinwa J. Iwuchukwu et al. "Self-organized photosynthetic nanoparticle for cell-free hydrogen production". In: *Nature Nanotechnology* 5 (2010), pp. 73–79.

[11] Hisako Kubota et al. "Purification and characterization of Photosystem I complex from Synechocystis sp. PCC 6803 by expressing histidine-tagged subunits". In: *Biochimica et Biophysica Acta - Bioenergetics* 1797.1 (2010), pp. 98–105.

[12] Rosemary K. Le et al. "Sortase-mediated ligation of PsaE-modified Photosystem I from Synechocystis sp. PCC 6803 to a conductive surface for enhanced photocurrent production on a gold electrode". In: *Langmuir* 31.3 (2015), pp. 1180–1188.

[13] Sahng Ha Lee, Jae Hong Kim, and Chan Beum Park. "Coupling photocatalysis and redox biocatalysis toward biocatalyzed artificial photosynthesis". In: *Chemistry - A European Journal* 19.14 (2013), pp. 4392–4406.

[14] David A. Levary et al. "Protein-Protein Fusion Catalyzed by Sortase A". In: *PLoS ONE* 6.4 (2011), pp. 3–8.

[15] Amy K. Manocchi et al. "Photocurrent generation from surface assembled Photosystem I on alkanethiol modified electrodes". In: *Langmuir* 29.7 (2013), pp. 2412–2419.

[16] Dibyendu Mukherjee, Mark May, and Bamin Khomami. "Detergent-protein interactions in aqueous buffer suspensions of Photosystem I (PS I)". In: *Journal of Colloid and Interface Science* 358.2 (2011), pp. 477–484.

[17] ELIANE NABEDRYK et al. "Conformation and Orientation of Chlorophyll-Proteins in Photostem I by Circular Dichroism and Polarized Infrared Spectroscopies". In: *Biochimica et Biophysica Acta* 767 (1984), pp. 640–647.

[18] Nathan Nelson. "Plant Photosystem I – The Most Efficient Nano-Photochemical Machine". In: *Journal of Nanoscience and Nanotechnology* 9 (2009), pp. 1709–1713.

[19] H. Hasko Paradies. "Shape and size of a nonionic surfactant micelle. Triton X-100 in aqueous solution". In: *The Journal of Physical Chemistry* 84.6 (2005), pp. 599–607.

[20] Eberhard Schlodder et al. "Fluorescence of the various red antenna states in Photosystem I complexes from cyanobacteria is affected differently by the redox state of P700". In: *Biochimica et Biophysica Acta - Bioenergetics* (2011).

[21] Nao Terasaki et al. "Plugging a molecular wire into photosystem I: Reconstitution of the photoelectric conversion system on a gold electrode". In: *Angewandte Chemie - International Edition* 48 (2009), pp. 1585–1587.

[22] Wu Xu et al. “Electron transfer in cyanobacterial Photosystem I. II. Determination of forward electron transfer rates of site-directed mutants in a putative electron transfer pathway from A0 through A1 to FX”. In: *Journal of Biological Chemistry* 278.30 (2003), pp. 27876–27887.

[23] Zhenle Yang et al. “Effect of phosphatidylglycerol on molecular organization of photosystem I”. In: *Biophysical Chemistry* 115.1 (2005), pp. 19–27.

[24] Zhenle Yang et al. “Photochemical activities of plant photosystem I particles reconstituted into phosphatidylglycerol liposomes”. In: *Journal of Photochemistry and Photobiology B: Biology* 78.2 (2005), pp. 125–134.

Chapter 4

Effects of Lipid Shape on Detergent Solubilization in Mixed-Lipid Liposomes

This chapter is revised based on a paper to submitted by Samantha Clark, Matthias M. L. Arras, Andy Sarles, and Paul Frymier. My primary contributions to the paper include: (1) development of the problem into a work, (2) identification of the study areas and objectives, (3) design and conducting of the experiments, (4) gathering and recording measurements, (5) processing, analyzing and interpretation of experimental data, (6) pulling reviewer contributions into a single papers, and (7) writing and editing.

Abstract

The effects of lipid charge and head group size on liposome partitioning by detergents are an important consideration for applications such as liposomal drug delivery or proteoliposome formation. Yet the solubilization of mixed-lipid liposomes - those containing multiple types of lipids - by detergents has received insufficient attention. This study examines the incorporation into and subsequent dissolution of mixed-lipid liposomes comprised of both egg phosphatidylcholine (ePC) and egg phosphatidic acid (ePA) by the detergent Triton-X100 (TX). Liposomes were prepared with mixtures of the two lipids, ePC and ePA, at molar ratios from 0 to 1, then step-wise solubilized with TX. Changes in turbidity, size distribution, and molar heat power at a constant temperature throughout the solubilization process were assessed. The data suggest that the difference in lipid shapes (shape factors = 0.74 and 1.4 [21, 12]) affects packing in membranes influences how much TX can be incorporated before liposomes disruption. As such, liposomes containing the observed ratios of ePA incorporated higher concentrations of TX before initiating dissolution into detergent and lipid mixed-micelles. The cause was concluded to be increased mismatching in the bilayer from the conical shape of ePA compared to the cylindrical shape of ePC. Additionally, the degree to which ePA is approximated as conical versus cylindrical was modulated with pH. It was confirmed that less conical ePA behaved more similarly to ePC than more conical ePA. The understanding gained here on lipid shape in liposome incorporation of TX enables research to use *in vitro* liposomes that more closely mimic native membranes.

4.1 Introduction

Previous work utilizes the membrane protein Photosystem I (PSI) [11, 17, 10, 24, 23] found in plants, algae, and photosynthetic bacteria to initiate charge-separation upon illumination. To increase the photoactivity of PSI requires methods to incorporate this protein into liposomes, which are similar to the protein's native environment. A common method used for the insertion of large membrane proteins such as PSI into liposomes is detergent-mediated reconstitution [18, 36, 39]. In this method, liposomes are saturated with detergent molecules to disrupt lipid-lipid interactions and ease the incorporation of proteins into the membranes. Disruption of the liposomes via detergent is commonly referred to as liposome solubilization. There is an optimum stage of liposome disruption for protein incorporation, dependent on the detergent-to-lipid ratio (D:L), beyond which liposomes are fully disrupted into micelles containing a mixture of lipid and detergent molecules [26, 38, 28, 20]. Previous research has investigated a wide range of interactions between lipids, like phosphatidylcholine (PC), phosphatidic acid (PA), and phosphatidylglycerol, and detergents, like Triton X-100 (TX), dodecyl maltoside, octyl glucoside, and cholamidopropyl dimethylammonio propanesulfonate both experimentally [2, 6, 1, 35, 3, 14, 15, 18], and using computational molecular dynamic simulations [42, 37]. Amongst these, a common mechanism has been elucidated that describes detergent-liposome interactions in a three-stage model [27, 41, 38]. This model is explained in detail in Section 4.2.4.

Despite extensive knowledge on single lipid-single detergent mixtures, little is known about how mixtures of lipid types in mixed-lipid liposomes influence detergent solubilization. Insights into these interactions will better enable protein reconstitution into liposomes that more closely resemble native membrane lipid mixtures in order to enhance protein stability and function [39]. One system of mixed-lipid liposomes made of 16:0PC and 16:0PG has been solubilized with bile salt [15], yet more systems need to be understood.

In this study, the interactions of the detergent, TX, with mixed-lipid liposomes made with varying ratios of egg PC (ePC) and egg PA (ePA) lipids are examined. These lipids were chosen because they have been used to successfully incorporate PSI into mixed-lipid liposomes with a fixed 9:1 ratio of ePC:ePA [4]. Despite initial success, there is a

need to utilize higher ratios of ePA to more closely mimic the charge composition of the cyanobacterial thylakoid membrane with which PSI is located [9].

Additionally, PC is a relevant test lipid because it is commonly used in *in vitro* applications, and it is a nonionic phospholipid that is the most abundant lipid in the majority cell membranes [6]. Here, the inclusion of PA represents the negatively charged lipid fraction, which typically composes 10-20 % of the lipids in *in vivo* membranes [25]. From a physical chemistry standpoint, these lipids are interesting because the shape of ePC is cylindrical in the bilayer and the shape of ePA is conical in the bilayer under physiological conditions [16]. The shape factor, which is the hydrocarbon volume divided by the optimal head area and the critical chain length, of each of these lipids is 0.74 and 1.4, respectively [16, 21, 12]. Furthermore, the degree of ionization of the PA head group can be easily modulated with pH [40, 22, 44]. The ionization changes the volume of the counterions associated with the PA head group, and therefore the cone angle of the lipids in the bilayer. The shapes, structures and ionization potentials of PC and PA are shown in Figure 4.1. The lipids are representatively depicted with two acyl chains that each consist of 18-carbon chain and 1 unsaturated bond (18:1), which is one of the predominant fatty acids present in naturally occurring ePC and ePA, seen in Figure 4.1(a). In addition to the successful use of ePC and ePA in reconstituting PSI mentioned above [4], naturally occurring lipids were selected because they better simulate the heterogeneity of *in vivo* membranes, which contain many lipids types and a diverse assortment of fatty acid chains. No systematic study of detergent solubilization with ePC and ePA mixed-lipid liposomes at varying headgroup ratios has been found.

Using absorbance spectrometry, dynamic light scattering, and isothermal titration calorimetry, D:L ratios are identified at which phase transitions occur for detergent reconstitution of ePC:ePA mixed-lipid liposomes. TX concentration at R_{sat} and R_{sol} are observed to significantly increases when the concentration of ePA in the liposomes is greater than 25 %. The difference in lipid shape provides an explanation: ePA lipids, which have conical molecular shapes, form defect-rich bilayers that facilitate greater incorporation of TX. Conversely, ePC lipids have cylindrical shapes that favor increased areas of contact with adjacent lipids and result in a lower probability of TX insertion. Additionally, the

influence of headgroup charge on TX solubilization of ePA membranes is examined; it was determined that a more negative net charge results in decreases in TX concentration at R_{sat} and R_{sol}.The shape model was also used to explain that as negative charges increase, there is a concomitant increase in counter-ions that increases the effective head group size and decreases mismatch in the ePA bilayer.

4.2 Materials and Methods

4.2.1 Materials

Potassium phosphate, sodium sulfate, and potassium sulfate were purchased from Fisher Scientific to prepare aqueous buffer solutions of 25 mM KH_2PO_4-KOH pH 7, 50 mM Na_2SO_4, 50 mM K_2SO_4 in ultrapure de-ionized water. Lipid derivatives from chicken eggs of phosphatidylcholine (ePC) and phosphatidic acid (ePA) were purchased from Avanti Polar Lipids, Inc. as powders with purity greater than 99 %. Additionally, powder lipids, 1,2-dipalmitoyl-sn-glycero-3-phosphochline (16:0PC) and 1,2-dipalmitoyl-sn-glycero-3-phosphate (sodium salt) (16:0PA), were also purchased from Avanti Polar Lipids, Inc. at greater than 99 % purity. 16:0PC and 16:0PA are purified lipids of the predominant fatty acid chain in egg of both PC and PA. The detergent, Triton X-100 ($<$ 3 % polyethylene glycol), was purchased from Sigma-Aldrich, as was chloroform (99.8 % pure) used to solvate the lipid powders. All compounds were used without further purification. Figure 4.1 shows some basic properties of the lipids PA and PC, and the saturation distribution of ePC and ePA derivatives from Avanti. It can be seen that the apolar part of ePC and ePA is within 1.5 % deviation identical. As introduced earlier, the fatty acid chain length and the degree of saturation are written as the number of carbon atoms : the number of unsaturated bonds.

	ePC	ePA
14:0	0.2	0.0
16:0	32.7	34.2
16:1	1.1	1.0
18:0	12.3	11.5
18:1	32.0	31.5
18:2	17.1	18.5
20:2	0.2	0.0
20:3	0.3	0.0
20:4	2.7	2.7
22:6	0.4	0.7
Unkn	1.0	0.0

(a) Fatty acid distribution

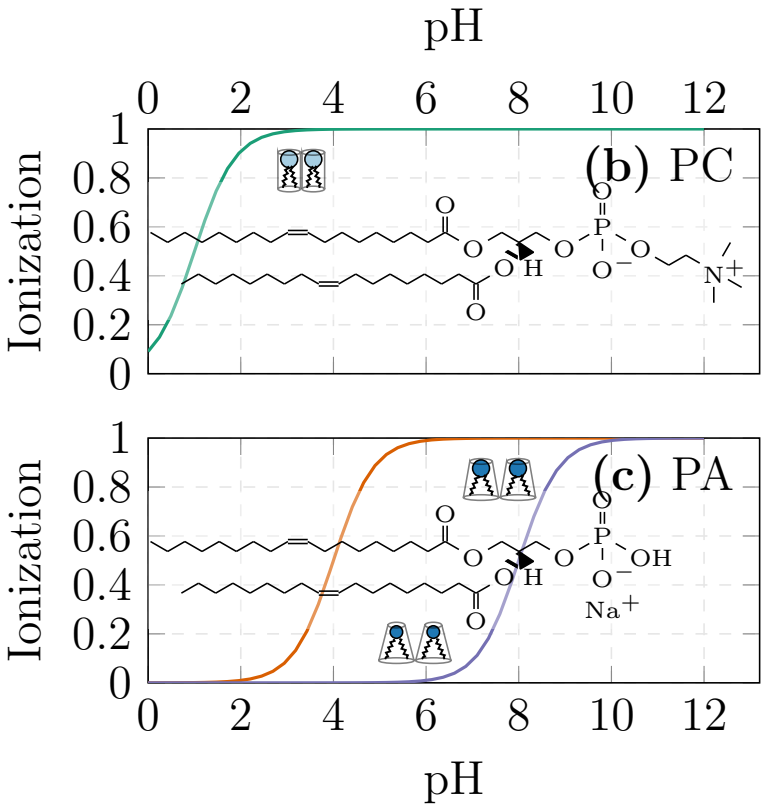

Figure 4.1: (a) Fatty acid distribution of natural ePC and ePA derivatives, as analyzed by Avanti Polar Lipids. (b) Chemical and shape structures of phosphatidylcholine (PC) and (c) phosphatidic acid (PA) lipids overlaying the ionization potential of the lipids with $pK_a \approx 1$ (—), $pK_a = 4$ (—), $pK_a = 8$ (—).

4.2.2 Liposome Preparation

Lipid powders were suspended in chloroform, then mixed and aliquoted in small glass flasks. The chloroform was completely evaporated overnight in a vacuum desiccator to form a thin lipid film on the flask walls. For the mixed-lipid liposome samples, the lipids were mixed together in inorganic solvent at the appropriate ratios prior to solvent evaporation. All lipid films were hydrated at 20 mg/mL in potassium phosphate buffer pH 7.2 (25 mM KH_2PO_4-KOH pH 7, 50 mM Na_2SO_4, 50 mM K_2SO_4). Vials were vortexed on low with a Fisher Scientific analog vortex mixer and heated 10 °C above the known phase transition temperature for 10 minutes to form multi-lamellar vesicles (MLVs) [43]. MLV solutions were put through 4 freeze-thaw cycles between -20 °C and room temperature. The stock lipids were mixed and diluted to 4 mg/mL with potassium phosphate buffer at pH 4.6, 7.2, or 10.2 for use. The liposomes were extruded using an Avanti Mini-Extruder system outfitted with a Whatman Nuclepore Track-Etch membrane (model 800309). All samples were extruded at room temperature. The lipid solution was passed 31 times through the membrane apparatus outfitted with 100 nm pore filters to form large unilamellar vesicles (LUVs). LUVs were used in subsequent experiments the day they were prepared.

4.2.3 Differential Scanning Calorimetry

The phase transition of the lipid mixtures was examined to probe the organization of lipids in multicomponent solutions using differential scanning calorimetry (DSC). Measurements were made using a TA Instruments NanoDSC calorimeter on samples prepared with 4 mg lipid per mL, and a reference containing deionized water. All lipid suspensions were prepared from stock MLV solutions of each of the lipids. Additionally, the samples and reference were placed under vacuum for 15 minutes with a stir bar rotating at 600 rpm in order to release any dissolved air. Sample and reference volumes of 0.5 mL were loaded into the calorimeter and held under a fixed pressure of 0.3 MPa to reduce bubble formation. The DSC scan protocol was as follows: cooling and equilibrating at 30 °C for 10 min, followed by three heating and cooling cycles to 70 °C and back. The first, second, and third cycles had scan rates of 1, 0.25,

and 0.25 °C/min, respectively. The temperature was held for a 10 min equilibration period at each endpoint during heating and cooling cycles.

4.2.4 Absorbance Spectrophotometry

The composition-dependent equilibrium transition of liposomes in the presence of varying detergent concentrations can be described following a three-stage model. This model describes morphological changes that occur as the lipid bilayer is disrupted (solubilized) into micelles [18, 36, 28, 20]. The stages of detergent-liposome interactions are depicted in Figure 4.2. They are labeled (I) saturation (or onset of solubilization), (II) partial solubilization, and (III) full solubilization. The morphological changes are illustrated schematically moving along the graph with increasing detergent concentration (x-axis) and the observed absorbance using spectrophotometry (y-axis). Stage I is signified by partitioning and insertion of detergent monomers into the liposomal bilayer, which results in swelling of the liposomes and a concomitant increase in light scattering measured with a spectrophotometer. In Stage II, there is a coexistence of detergent monomers, liposomes, and micelles containing a mixture of lipid and detergent molecules. Stage II is seen with decreasing observed absorbance. In Stage III, there is complete dissociation of liposomes into mixed lipid-detergent micelles in which further detergent addition does not influence observed absorbance, thus Stage III is marked by a baseline absorbance. Saturation (R_{sat}) is the ratio of detergent to lipid at the maximum detergent concentration that liposome bilayers can incorporate before mixed lipid-detergent micelles begin forming. It is seen as the transition point from Stage I to Stage II. Liposome solubilization (R_{sol}) is the ratio of detergent to lipid at the point of complete disruption of all lamellar phases. It is seen as the transition point from Stage II to Stage III. Previous studies indicate that the most successful protein incorporation occurs during the second stage of detergent-mediated solubilization [18, 39, 4]. It is, therefore, relevant to map these transitions. The detergent concentration necessary for the onset of each stage is influenced by lipid-lipid interactions within the bilayer and lipid interactions with the surrounding aqueous environment. Variable lipid characteristics, such as charge, head group size, and length and degree of saturation of fatty acid chains, can be selected to influence membrane properties and solubilization [7].

In this work, the stages of solubilization with the detergent, TX, were determined for equilibrated liposomes. TX dilutions were prepared at 2.4 – 120 mg/ml and added to aliquots of liposomes in duplicate at detergent to lipids (D:L) ratios of 0 – 6 w/w. These were mixed 10 times using a pipette and equilibrated at room temperature for 30 minutes. The final lipid concentration of all aliquots was 3.2 mg/ml. The absorbance of the lipid-detergent emulsions was measured at 400 nm using a Thermo-Scientific NanoDrop 2000C spectrophotometer at room temperature. Accompanying NanoDrop2000 software was used in the UV-Vis mode to do a full spectrum sweep between 190 - 840 nm to observe any sample placement issues, such as air bubbles, and record the absorbance at 400 nm. Three measurements were taken for each sample and averaged for a final absorbance at each D:L ratio. The data was then normalized to an initial liposome absorbance of 1. This procedure was replicated three times for each lipid composition and pH. The average of multiple runs was graphed with standard deviations to determine the affinity of detergent to each lipid composition and pH. Liposome saturation (R_{sat}) and solubilization (R_{sol}) were determined from the resulting absorbance vs. D:L solubilization curves. R_{sat} was determined at the peak of the curve. R_{sol} was defined to be the first D:L less than or equal to the average of the last three data points plus standard deviation of 0.007. 0.007 was determined by the instrument and samples margin of error by performing repeated measurements on the same sample.

4.2.5 Dynamic Light Scattering

Dynamic light scattering (DLS) was used to analyze the change of the liposome size distribution throughout the lipid-detergent solubilization process. Samples were prepared in the same manner as for absorbance spectrometry at appropriate D:L ratios. Emulsions were given approximately thirty minutes to equilibrate prior to measuring the diameter and distribution in a Wyatt Technology DynaPro NanoStar fixed angle dynamic light scattering instrument. 10 µl samples at 3.33 mg lipid per ml were measured at 20 °C for 20 acquisitions of 10 seconds each. Three sample preparations were made for each lipid mixture and buffer. The data were fit with the standard isotropic sphere model at optimal resolution and each preparation was averaged to compare the diameter across stages of each liposome preparations' solubilization with TX.

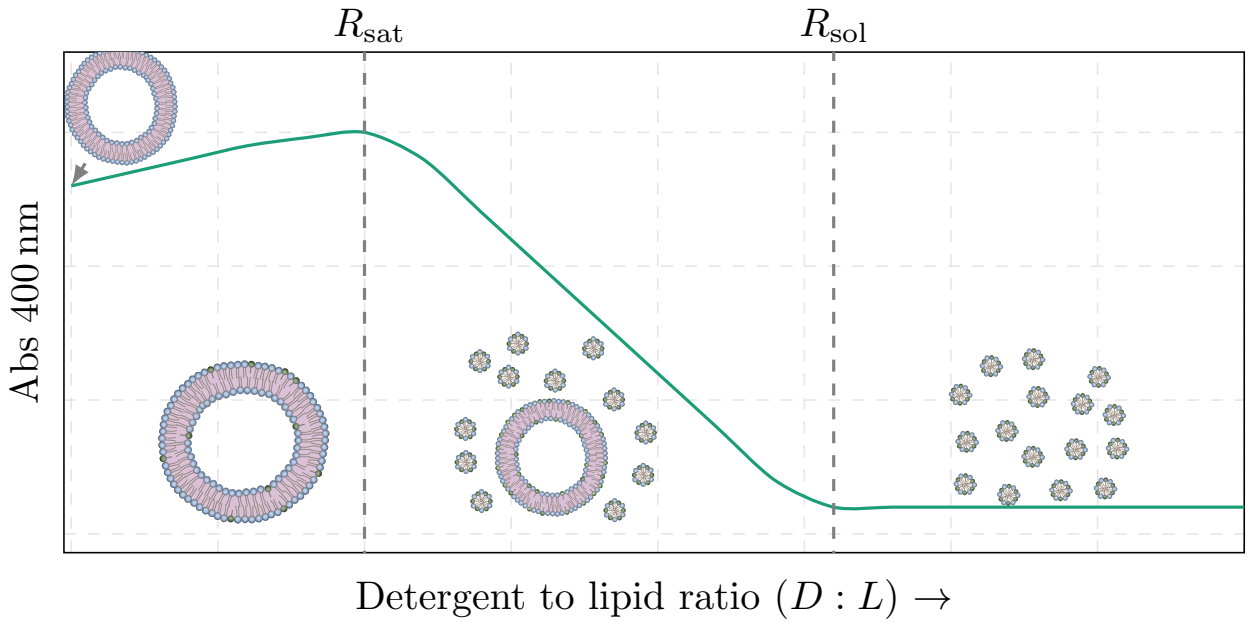

Figure 4.2: Demonstration of morphological changes in detergent solubilization of liposomes observed throughout turbidity measurements with absorbance spectrophotometry recorded at 400 nm. Stages I, II, and III are panels left to right. Adapted from Seddon *et al.* [39].

4.2.6 Isothermal Titration Calorimetry

To observe the binding affinity of detergent with liposomes and assess the change in enthalpy as the surfactant partition lipid membranes, isothermal titration calorimetry (ITC) is considered a preferred method [8, 5]. Following the protocol of Heerklotz *et al.* [13], adapted by Nirromand *et al.* [33], the characteristic heat signal under TX titration into preformed liposomes was observed using a VP-ITC instrument manufactured by MicroCal Inc. (Northampton, MA). To prepare samples, 4 mg/ml extruded liposomes and a 154 mM TX solution were degassed under reduced pressure with constant stirring for 10 minutes, slightly below the experimental temperature, at 23 °C. Following degassing, the calorimeter sample cell and injector-syringe chamber were loaded with 1.4 mL of the liposome solution and 300 µL of the detergent solution. A series of TX injections were made at 30 minute intervals following this sequence: 2.0, 3.0, 3.0, 3.0, 3.0, 4.0, 2.0, 3.0, 3.0, 2.0, 4.0, 4.0, 4.0, 4.0, 2.0, 3.0, 4.0, 3.0, 4.0, 3.0, 3.0, 3.0, 7.0, 4.0, 5.0, 5.0, 6.0, 4.0, 6.0, 4.0, 7.0, 6.0, 5.0, 7.0, 13.0, 10.0, 20.0, 22.0, 25.0, 25.0, 30.0 µL. This series of injections was chosen to optimize

enthalpic data in regions of interest, i.e. near R_{sat} and R_{sol}. The change in applied heat to maintain a constant sample cell temperature was recorded and analyzed using the associated MicroCal Inc. software. Integration of the heat signal describes the change in enthalpy for each injection.

4.3 Results and Discussion

4.3.1 Phase Transitions of Lipids and Lipid-Mixtures

Phase transition temperatures of lipid solutions were determined using differential scanning calorimetry (DSC) to confirm the mixed-lipid preparation method yields liposomes containing both PC and PA. With DSC, a change in the transition temperature was observed of lipid bilayers containing either PC or PA lipids individually and bilayers containing both PC and PA lipids together. DSC was performed using model PC and PA lipids with fatty acid chains made of 16 carbon atoms and no double bonds (16:0). 16:0PC and 16:0PA were selected because they are the most abundant species of lipids in ePC (32.7 mol % 16:0) and ePA (34.2 mol % 16:0), and they exhibit melting point transitions above 0 °C. The detergent-liposome association experiments discussed later were performed on naturally derived lipids from egg yolks (ePC and ePA), which contain a variety of fatty acid chains and have melting point transitions below 0 °C, rendering liquid (water) DSC unsuitable.

Figure 5.2, shows the molar heat capacity (MHC) of colloidal dispersions of multi-lamellar vesicles (MLV) of 16:0PC, 16:0PA, and 1:1 16:0PC-16:0PA mixed-lipid MLVs. 16:0PC (—) exhibits a sharp, narrow, endothermic peak at 42 °C, and a small, pre-transition peak with a maximum at 35 °C. 16:0PA (—) exhibits a single peak with a maximum at 64 °C. These single species melting points are consistent with literature values [43]. The 1:1 16:0PC-16:0PA mixed-lipid MLVs (—) has a single broad peak with a maximum located at 54 °C. Per McElhaney *et. al.* [30], the transition arises from reversible melting of fatty acid chains as they change from the rigid, fully extended, gel state, to the more fluid and disordered, liquid-crystalline state. The melting transition leads to thinning of the bilayer and a marked

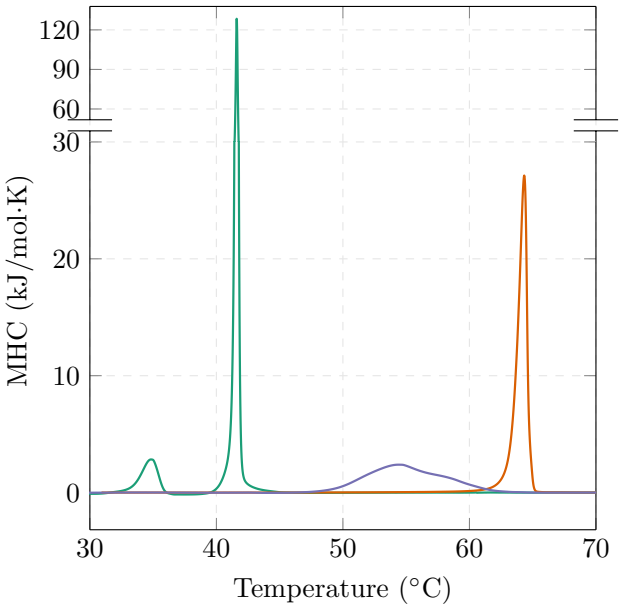

Figure 4.3: Lipid phase transitions determined using DSC of PC MLVs (—), PA MLVs (—), and 1:1 16:0PC-16:0PA mixed-lipid MLVs (—). All final lipid concentrations are 4 mg per mL.

increase in lateral diffusion of lipids. In the 16:0PC sample, the region between the two peaks is characterized by periodic ripples in the membrane [30].

The respective melting temperatures for 16:0PC and 16:0PA MLVs are separated by approximately 20 °C. The broader peak in the 1:1 16:0PC-16:0PA mixed-lipid MLV sample indicates there is a mixture of MLVs containing both lipids together in the membranes. This indicates a lack of cooperativity between the phospholipid molecules in the bilayer during lipid melting [29]. The melting temperature of 1:1 mixed-lipid MLVs of 16:0PC-16:0PA (54 °C) is closer to 16:0 PA (64 °C), than to 16:0 PC (42 °C), and the 16:0PC pre-transition was not present. The lack of a pre-transition is expected, as the presence of other lipid compounds in solution is known to eliminate a pre-transition [32]. These results show that the preparation protocol for mixed-lipid MLVs yields membranes mixtures of both lipids. While Figure 5.2 is for pure lipid species (16:0 only), the rest of the work in this paper is on mixed-fatty acid chains. Following the same preparation procedure, the liposomes will contain both lipids together in the bilayers [29].

4.3.2 Turbidity Evidence of Mixed-Lipid Liposome Disruption by TX

Turbidity changes in liposome solutions were quantified using optical absorbance with spectrophotometry at 400 nm at varying ratios of D:L for mixed-lipid vesicles with varying ratios of ePC and ePA. In this technique, absorbance decreases with decreasing particle size and increases with increasing particle size (see section 4.2.4). As the initial amounts of detergent are added to the liposomes, detergent monomers penetrate the bilayers. In the lowest D:L ratio (0.12), the TX concentration is an order of magnitude above the detergent critical micelle concentration of 0.15 mg/ml in pure water. In Figure 4.4, the curve shapes for mixtures of ePC and ePA are characteristic of general detergent association and break-down of liposomes. Here, the D:L ratios (R_{sat} and R_{sol}) that characterize the stages of solubilization are much lower for liposomes containing only ePC lipids and are higher for liposomes containing any amount of ePA lipids. In liposomes containing a mixture of both lipids, the D:L ratios at which the stages of solubilization occur are most similar to that of ePA-only liposomes. Additionally, the normalized absorbance at 400 nm in Stages I and II are also markedly higher for all ePA-containing samples than for ePC alone. In Stage III, the normalized absorbance is similar for all samples, marking the complete conversion of liposomes into mixed micelles.

Figure 4.5(a) shows the detergent to lipid ratios at peak detergent saturation, R_{sat}, for the mixed-lipid liposomes (see section 4.2.4). R_{sat} is plotted as a function of lipid composition with an increasing percentage of ePA; the remaining is ePC. In Figure 4.5, mixed-lipid liposomes containing only 25 % conical ePA lipids incorporate nearly twice as much TX as cylindrical ePC liposomes alone. 50 % ePA incorporates a similar concentration of TX as 25 % ePA, whereas 75 % and 100 % ePA liposomes reach R_{sat} with even more TX.

In Figure 4.5(b), R_{sol} is displayed for each lipid composition in Figure 4.4. This is the ratio of detergent to lipid at the first point that liposomes are completely solubilized into mixed-micelles. R_{sol} is higher for 100 % ePA than 100 % ePC (0% ePA). One can also see a skewed parabolic curve for mixed-lipid liposomes with 0, 25, 75, and 100 % ePA. Additionally, error bars are standard deviations and do not include instrumental or systematic error.

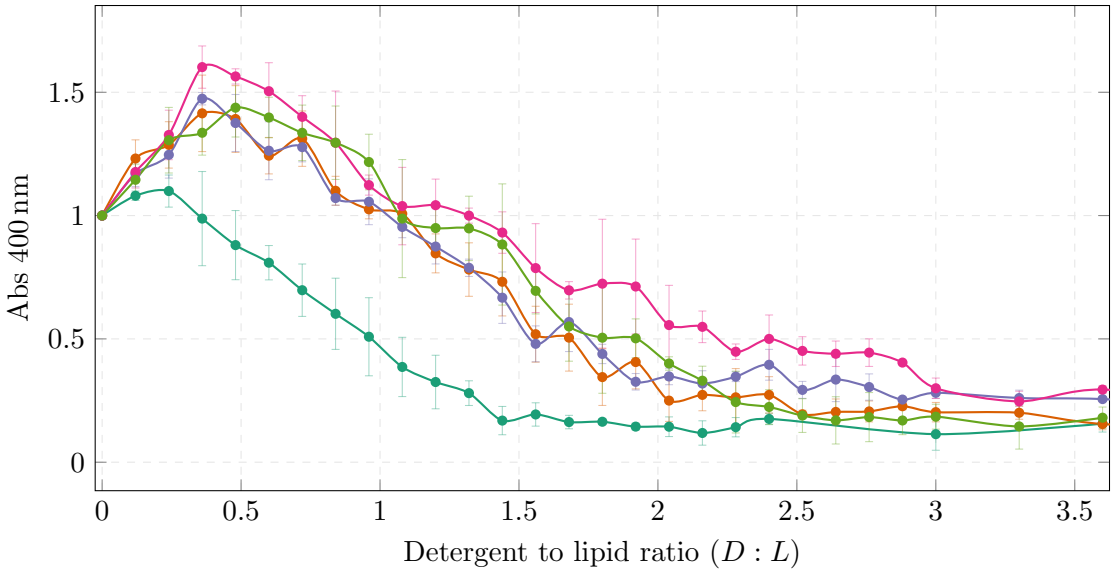

Figure 4.4: Turbidity changes in mixed-lipid ePC:ePA liposomes at 100:0 (•),75:25 (•), 50:50 (•), 25:75 (•), and 0:100 (•) induced by TX detergent addition and measured using absorbance spectrometry at 400 nm. Data-point connecting lines are guides to the eye.

The difference in D:L ratios for saturating and solubilizing liposomes can be explained by the shape of each lipid. As seen in Figure 4.1, ePC has a cylindrical shape and ePA has a conical shape. In the liposomes, of the order of 100 nm, the lipids interact as in a planar bilayer [37]. The cylindrical ePC lipids form a bilayer with cylinders stacked side-by-side with little space for TX to insert. Thus ePC liposomes reach R_{sat} and R_{sol} at low D:L ratios with little increase in normalized absorbance at R_{sat}. Conversely, ePA lipids have a conical shape that forms gaps between the phospholipid heads in bilayers that more easily accept TX [21, 31]. ePA-only liposomes reach R_{sat} and R_{sol} at the highest D:L ratios and a high normalized absorbance at R_{sat}. This shows there is significant swelling as TX is incorporated into ePA bilayers, and that ePA bilayers can take on more TX before disrupting into mixed-micelles. Mixed-lipid liposomes, with at least 25 % or more conical ePA, have openings for TX to more easily incorporate into the bilayer resulting in liposomes behaving more similarly to ePA-only than ePC-only.

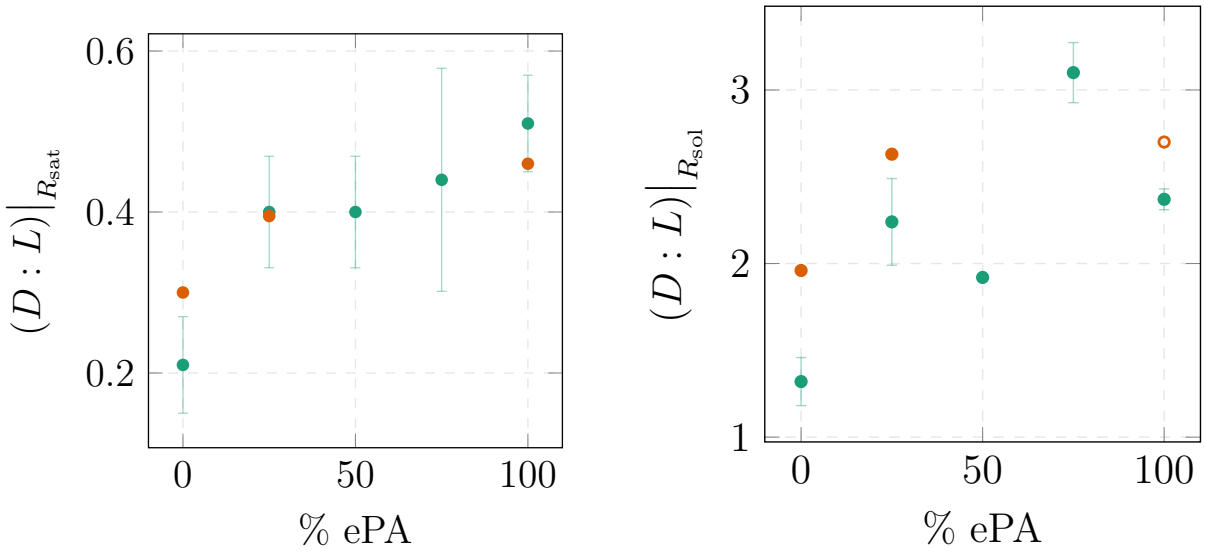

(a) R_{sat} **(b)** R_{sol}

Figure 4.5: D:L ratio at A) R_{sat}, liposome saturation, and B) R_{sol}, liposome solubilization, for mixed ePC and ePA lipid liposomes. Values obtained via absorbance (•) and isothermal titration calorimetry (• , ◦), displayed as % ePA; the remainder is % ePC.

4.3.3 Size Distribution of Mixed-Lipid Liposomes and Mixed-Micelles

DLS was used to observe changes in particle size distribution as mass averages before and after liposome solubilization with TX. Figure 4.6 shows the distribution averages of liposomes made with mixtures of ePC and ePA lipids after extrusion, without TX (top row) and with TX in Stage III (bottom row). Liposomes were formed via extrusion through 100 nm pores. In this process, much larger concentric lipid vesicles are restructured into a reasonably monodisperse liposome population that is slightly larger than 100 nm, as seen in the top row of Figure 4.6. Here, the average diameter weighted by % mass was determined from each liposome distribution and shown in the first column of Table 4.1. The standard deviation is calculated from the average diameter of each of the lipid mixture preparations. The average diameter of all liposomes was 121 nm. There was little variation in liposome diameter throughout the lipid mixtures examined. Following complete solubilization, liposomes were redistributed into mixed-micelles by high concentrations of TX. This occurs in Stage III of solubilization, also seen in Section 4.3.2. Mixed-micelles are aggregated detergent and

lipid mixtures with the lipid and detergent hydrophobic regions in the center of a sphere-like shape surrounded by the lipid and detergent hydrophillic regions. The distribution of the diameter of mixed-micelles for each lipid mixture is shown in Figure 4.6 (bottom row). The average diameter for each lipid composition is in the second column of Table 4.1. The average diameter for all mixed-micelles is $19 \pm 1\,\text{nm}$.

Lipid shape plays a role in both the process of liposome saturation and solubilization, but there were insignificant differences in the resulting mixed-micelle size based on lipid shape or percentage of each lipid type. Once the lipid bilayer structure is broken down, the two lipid types behave similarly in micelles. However, the presence of either lipid nearly doubles the diameter of the mixed-micelles versus TX only micelles, which have a diameter of $11 \pm 1\,\text{nm}$ in the buffer used here. Assuming a perfect sphere, lipids increase the TX micelle volume by a factor of 5, from $700\,\text{nm}^3$ to $3{,}600\,\text{nm}^3$, and the surface area increases by a factor of 3, from $380\,\text{nm}^2$ to $1134\,\text{nm}^2$ Several structural aspects of lipids could affect this, including long carbon chains, known to increase aggregation number, and strong head group repulsion, which can increase the distance between head groups [34]. The lipids, ePC and ePA, have different shapes based on their head groups, but they have a similar fatty acid distribution. In mixed-micelles, it may be the similar fatty acid distribution of these two lipids that result in similarly sized mixed-micelles. In other words, lipid shape is important during the liposome solubilization process, but lipid tails seem to dictate the size of the Stage III mixed-micelles.

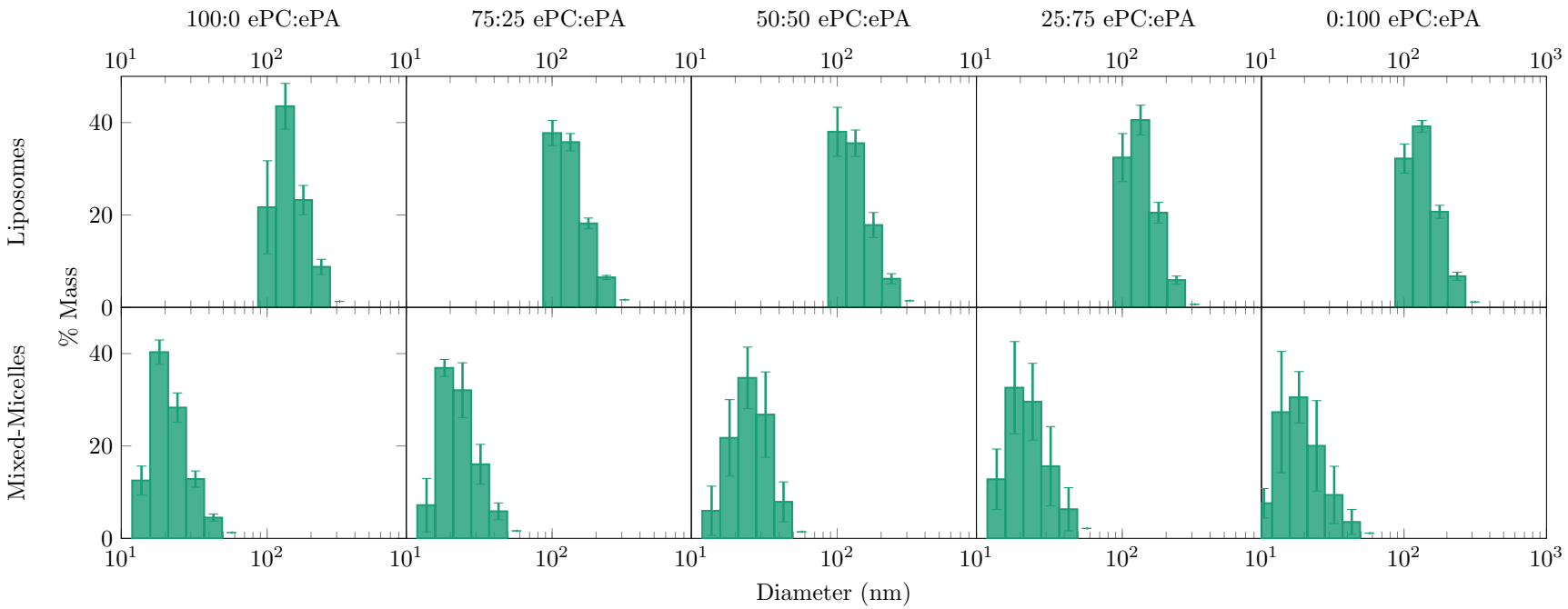

Figure 4.6: Particle size distribution measured using dynamic light scattering of mixed-lipid liposome samples as extruded liposomes (top row) and mixed-micelles in Stage III (bottom row).

Table 4.1: Average diameter of ePC:ePA mixed-lipid liposomes and mixed-micelles made with TX in Stage III.

% ePA	Liposomes Avg d (nm)	Mixed-Micelles Avg d (nm)
100	121.7 ± 3.5	17.8 ± 2.3
75	120.0 ± 2.7	19.4 ± 1.4
50	118.7 ± 4.6	19.7 ± 0.7
25	120.2 ± 1.5	18.1 ± 5.3
0	126.1 ± 2.8	19.9 ± 3.4

4.3.4 Calorimetry Evidence of Mixed-Lipid Liposome Disruption by TX

To gain understanding on the influence of ePA and ePC on TX solubilization, isothermal titration calorimetry (ITC) was performed. ITC was used to monitor the partition of detergent into bilayers, as well as the formation of mixed-micelle structures as the detergent is titrated into a solution with pre-formed liposomes. The equilibrated processes of saturation and solubilization release and absorb net heat that was observed through changes in compensation heating power (Δp) required to maintain a fixed temperature. In Figure 4.7, these transitions were observed for 100:0, 75:25, 0:100 ePC:ePA liposomes. The top row, (a), shows the raw data of Δp applied during each injection of TX, which is always followed by an equilibration period. The injection volumes were varied to optimize the resolution in the R_{sat} region, as seen in previously published protocols [33, 13]. The heat power curves throughout the titration exhibited the same characteristic solubilization shape, starting with a positive Δp endothermic region (Stage I), followed by a negative Δp exothermic region (Stage II), and lastly, a small, positive Δp endothermic region (Stage III), barely or not reached for 25 and 100 % ePA samples due to chamber volume limitations. Stages I, II, and III mentioned here correspond to the stages described by the absorbance solubilization curve, shown in Figure 4.2. In Stage I, Δp for both 25 and 100 % ePA liposomes was higher and the stage persisted over more TX titrations than for 100% ePC liposomes. This corresponds to observations made in Sections 4.3.2 and 4.3.3 in which higher concentrations of TX are required to transition to Stage II. As the time-based injections varied in volume, it is useful to look at D:L throughout the titrations in Figure 4.7(b).

In Figure 4.7(b), raw heat power data was used to calculate the heats of injection per mole of TX as a function of D:L on a weight basis. The D:L transitions for R_{sat} and R_{sol} were determined at the breakpoints for a sharp decrease and a stabilization in Q ($\Delta p = 0$ or $Q = 0$), respectively. For 100:0, 75:25, and 0:100 ePC:ePA, R_{sat} was determined to be 0.30, 0.40, and 0.46 w/w D:L, and R_{sol} was determined to be 1.96 w/w D:L, 2.63 w/w D:L, and was not reached in the 0:100 ePC:ePA sample, but can be estimated to be around 2.7. The data is shown in Figure 4.5 for comparison to the absorbance results. These values are at slightly higher than absorbance spectrometry observations in Section 4.3.2. Nevertheless, the trend of both absorbance and ITC data sets are the same, in which pure ePC reaches R_{sat} and R_{sol} at the lowest D:L of all the samples. Also, the R_{sat} and R_{sol} values of 25% or more ePA lipids are closer to that of ePA-only samples.

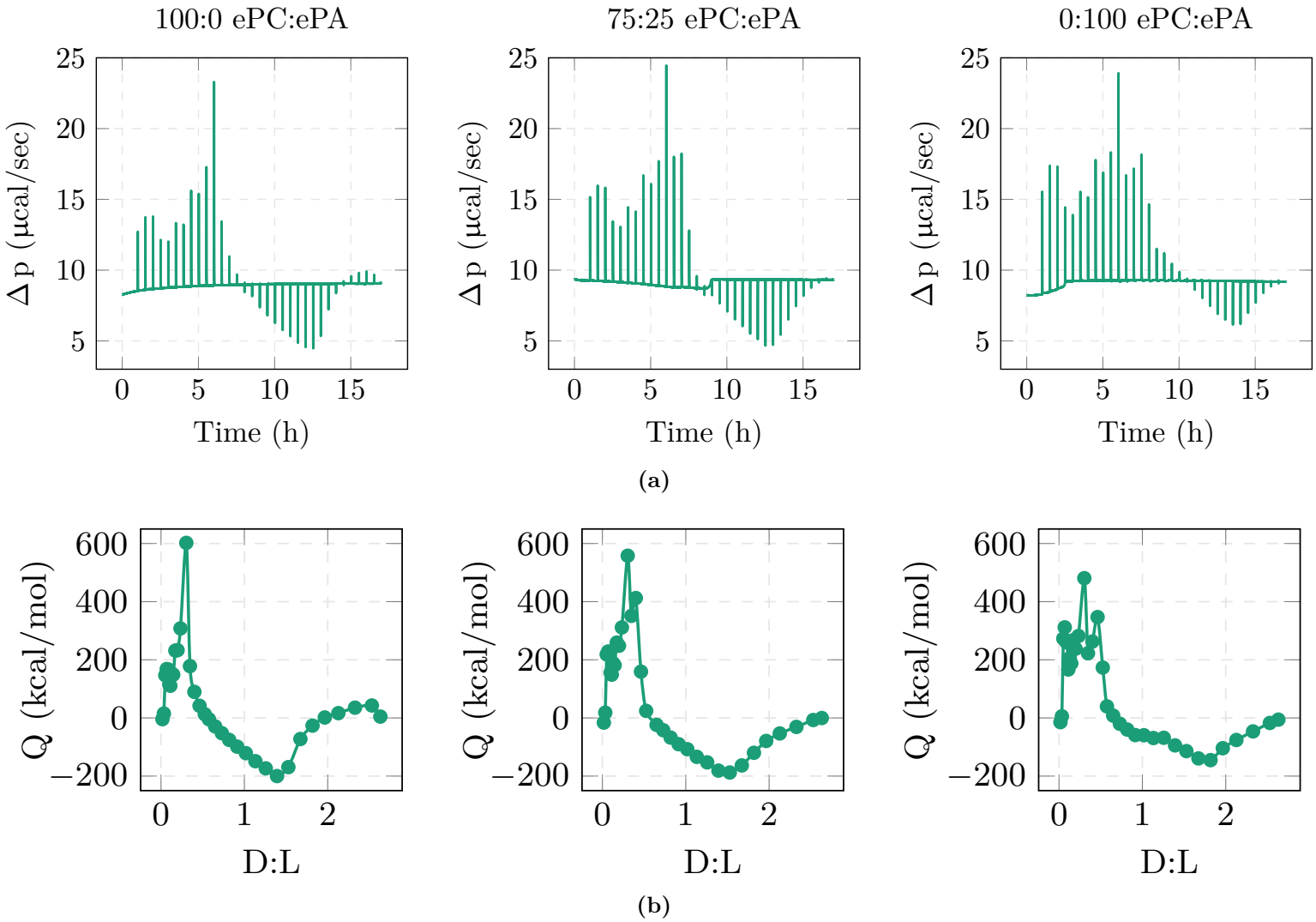

Figure 4.7: Isothermal titration calorimetry for solubilization of preformed liposomes with step-wise titrations of TX. Liposomes made with (left to right) 100:0, 75:25, and 0:100 ePC:ePA. (a) Raw data of compensation heat power, Δ p (µcal/sec), versus time in hours. (b) Heats of injection, Q (kcal/mol TX), versus D:L ratio (w/w). The solid lines are again a guide to the eye.

4.3.5 Triton X-100 Association with ePA as a Function of pH and Charge

The primary differences between ePC and ePA lipids are charge and head group size and shape. This leads to different overall lipid shapes and packing within bilayers. The ePA headgroup is smaller than the ePC headgroup, as discussed above this lends to an overall conical shape of ePA lipids and a cylindrical shape of ePC lipids. Since ePA, a charged lipid, liposomes require a higher concentration of TX to solubilize than ePC liposomes, the effect of the charge on solubilization was examined by adjusting the pH, and thus, the lipid ionization, as depicted in Figure 4.1(c). Absorbance solubilization curves of 0:100 ePC:ePA liposomes at pH 6, 7 and 8 can be seen in Figure 4.8. ePA liposomes at pH 8 are saturated and solubilized at the lowest D:L ratio of the tested buffers. ePA liposomes at pH 7 are saturated and solubilized at a higher D:L, and lastly, ePA liposomes at pH 6 are saturated and solubilized at the highest D:L. The absorbance curves shifts to the right as the pH decreases for ePA liposomes. Additionally, the absorbance maxima increase slightly with decreasing pH. The change in peak absorbance at 400 nm compared to the pristine extruded liposome is 0.58, 0.44, and 0.38 for increasing pH from 6 to 7 to 8. This means that decreasing the pH allows the liposomes to swell more before the onset of solubilization occurs. R_{sat} and R_{sol} were determined as described above and are graphed in Figure 4.9. A roughly linear relationship is seen for R_{sat} and R_{sol}, and as pH increases, the D:L ratio required to achieve these states decreases. The D:L ratios at R_{sat} and R_{sol} were approximately 1.8 times higher at pH 6 than at pH 8.

Changes in D:L at R_{sat} and R_{sol}, and a change in maximum absorbance of ePA varying pH shows that ePA charge affects the interaction of TX with the bilayers. The ionization potential in Figure 4.1, shows that at lower pH's, ePA is in a less negative state. At the lowest pH observed, pH 6, the R_{sat}, R_{sol} and maximum absorbance of liposomes was the highest measured. At this pH, ePA is less negatively charged than at pH 7 and 8, and thus there are fewer counter-ions present in the bilayer. The decrease in counter-ions makes the shape of ePA more conical [19]. As discussed in Section 4.3.2, there is a strong correlation between lipid shape and $R_{\text{sat}}/R_{\text{sol}}$, and here, the more conical ePA has more mismatches in

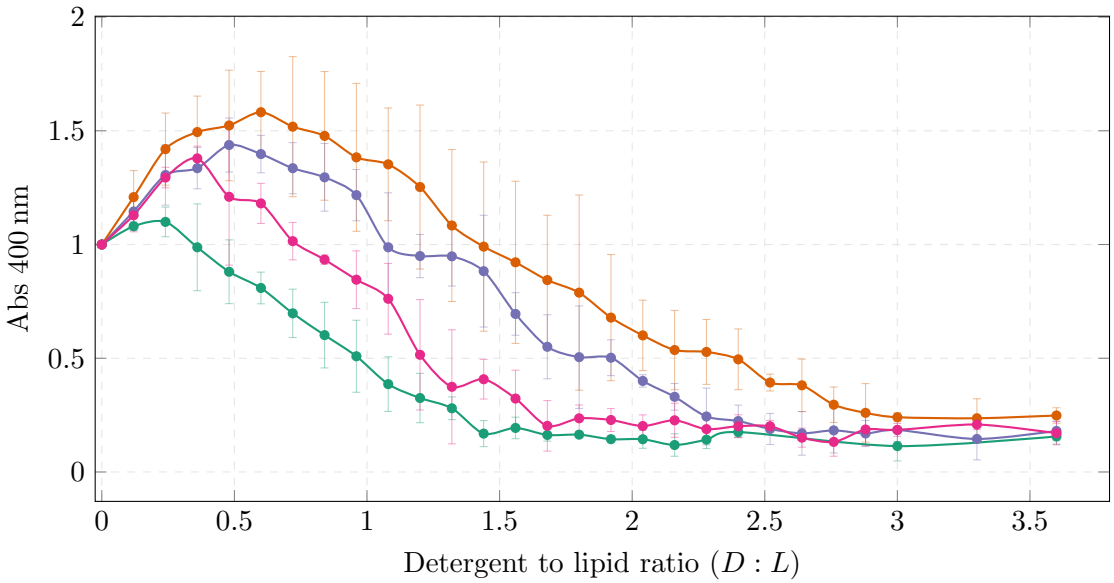

Figure 4.8: Turbidity changes in ePA liposomes at pH 6 (•), pH 7 (•), and pH 8 (•) and ePC liposomes (•), induced by detergent addition and measured using absorbance spectrometry at 400 nm. The solid lines are a guide to the eye.

the bilayer. This enables higher concentrations of TX to be incorporated in the liposomes before disrupting into mixed-micelles. Conversely, ePA at the highest pH observed, pH8, is in a more negatively charged state and has more counter-ions present. The increased counter-ions lend to a less conical shape, which increases the resistance to TX incorporation into the bilayer. Further, the solubilization curve of ePC liposomes is also shown in Figure 4.8. It is seen that the cylindrical shape of the lipids in liposomes are saturated and solubilized with less TX than conically shaped ePA lipids.

4.3.6 Size Distribution of ePA Liposomes and Mixed-Micelles with Varying pH

Figure 4.10 shows the size distribution of ePA liposomes at pH 6, 7, and 8 measured using DLS. As expected for the preparation procedure, each liposome sample was substantially monodisperse. The average diameter for each buffer solution was calculated from the diameter of each sample preparation based on % mass distributions. The averages are shown in Table 4.2. Each population was near 122 nm after preparation, showing there is no significant difference in freshly prepared liposome size by varying pH. Once the liposomes

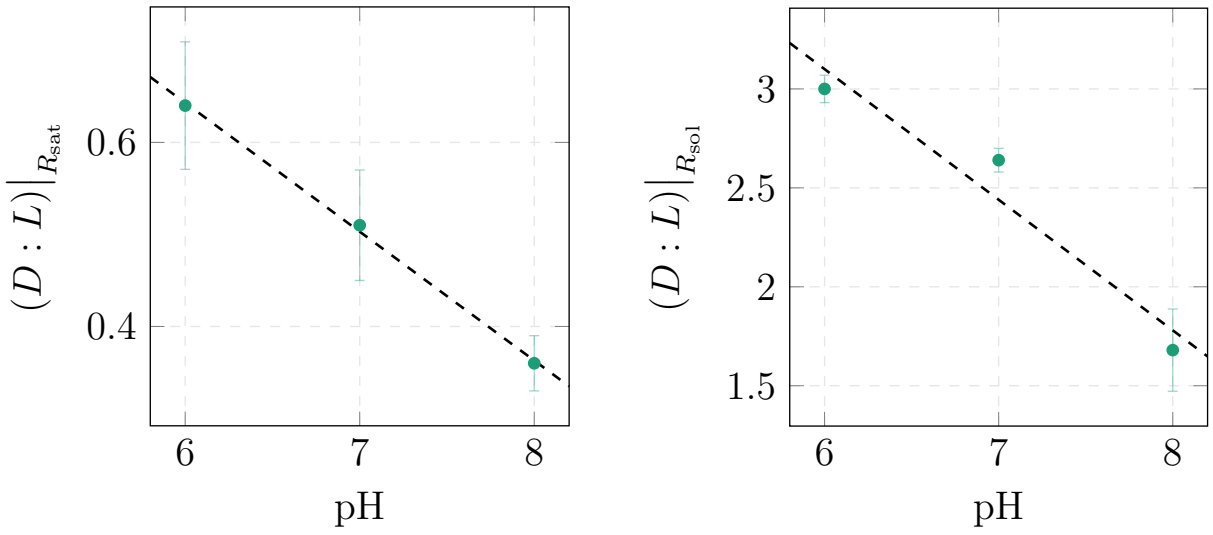

(a) R_{sat} **(b)** R_{sol}

Figure 4.9: D:L ratio at (a) liposome saturation and (b) solubilization for ePA at pH 6, 7 and 8.

are fully solubilized in Stage III, the mixed-micelles size is similar for ePA at pH 6, 7, and 8. This supports the influence of fatty acid length on micelle size and the lack of influence of lipid shape in these mixed-micelles.

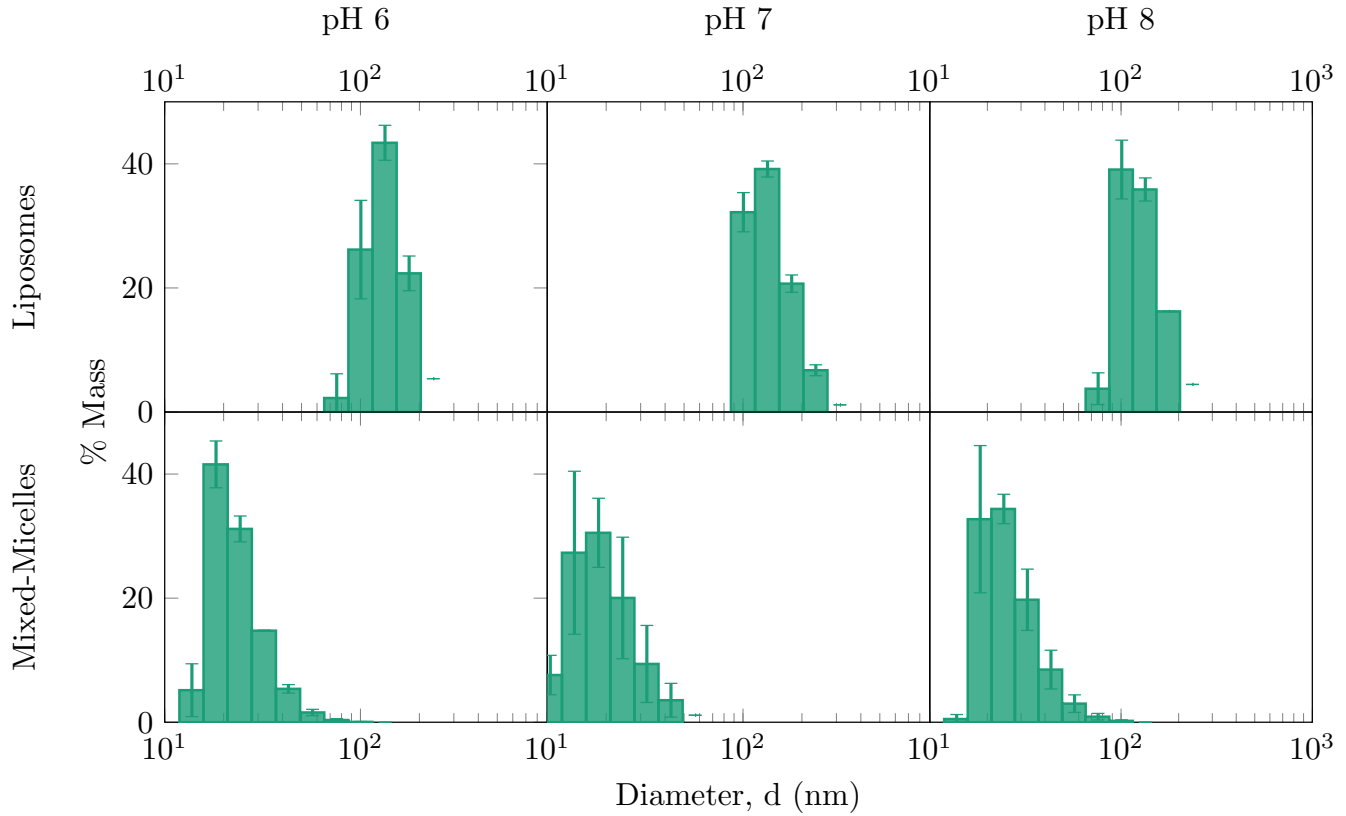

Figure 4.10: Particle size distribution of ePA liposomes (top row) at pH 6 (left column), pH 7 (middle column), and pH 8 (right column), and mixed-micelles in Stage III (bottom row).

Table 4.2: Average diameter of ePA liposomes and mixed-micelles in Stage III at pH 6, 7, and 8.

pH	Liposomes Avg d (nm)	Mixed-Micelles Avg d (nm)
6	120.6 ± 3.4	19.0 ± 2.2
7	121.7 ± 3.5	17.8 ± 2.3
8	123.3 ± 2.1	18.3 ± 2.2

4.4 Conclusions

TX is a non-ionic amphiphilic molecule with a long hydrophilic polyethylene oxide chain and a bulky aromatic hydrocarbon group. It was incorporated into liposomes of varying compositions made of ePC and ePA lipids. Absorbance spectrometry shows that ePC liposomes are solubilized with significantly less TX than ePA-only and mixed-lipid ePC:ePA liposomes at ratios of 25:75, 50:50, or 75:25. The TX response of liposomes containing any amount of ePA tested here more closely resembles that of 0:100 than 100:0 ePC:ePA liposomes. Additionally, during ITC, the heat power response to TX titration of 25 % ePA liposomes more closely resembles 100 % ePA than 100 % ePC. Thus, the influence of ePA, even at low concentrations, makes ePC liposomes less sensitive to disruption by TX.

The differences in ePA and ePC interactions in liposomes with TX are explained by lipid shape in Figure 4.11. The structure of ePC lipids consists of a mobile, zwitterionic phosphotidyl choline head group and a combination of saturated and unsaturated fatty acid chains, as seen in Figure 4.1(b). The overall structure of the lipid is cylindrical. The liposome size used here, which is greater than 100 nm in diameter, has little curvature effect on the individual lipid interactions. This enables the efficient packing of cylindrical lipids, as seen in Figure 4.11(a). The packing of cylinders increases the difficulty of TX to incorporate into the liposome and results in reduced swelling at R_{sat}, lower possible incorporation of TX into bilayers, and liposomes that transition to mixed-micelles at lower ratios of TX to lipid. Conversely, the structure of ePA lipids is made up of a small, immobile phosphatic acid head group and a combination of saturated and unsaturated fatty acid chains, seen in Figure 4.1(c). The generally accepted structure is conical [16], which creates defects in the bilayer between neighboring conical lipids and favors the incorporation of TX into the liposome

bilayers, Figure 4.11(b). Easier incorporation of TX, allows the liposomes to accommodate higher concentrations of TX and swell more before disrupting into mixed-micelles. The influence of the conical ePA shape also has a drastic effect on R_{sat} when ePA is mixed with ePC in liposomes. The three ratios of ePC:ePA mixed-lipid liposomes observed showed that the conical shape significantly enhanced the maximum uptake of liposomes before disruption, Figure 4.1(d). While the arrangement of ePC and ePA lipids within the bilayer is not yet known, data in Figures 4.4 and 4.7 suggest the addition of even 25% conical lipid drastically increases the density of defects in the bilayers and increases R_{sat} and maximum swelling before bilayer disruption.

Additionally, the influence of lipid charge in ePA on TX solubilization was probed by varying the pH. The net charge of ePA transitions from -1 to -2 between pH 6 and 8, as seen in Figure 4.1(c). TX absorbance solubilization curves of ePA liposomes at pH 6, 7, and 8, in Figure 4.8, show that there is a linear relationship between charge and $R_{\text{sat}}/R_{\text{sol}}$. More negatively charged ePA liposomes are saturated and solubilized at higher D:L ratios. Increased ease of detergent saturation and solubilization in more negatively charged bilayers can be explained by increased counter-ion affinity at the head groups, which alters the shape of the lipids in the bilayers. PA is known to have a conical shape due to the small phosphatidic acid head group. Addition of a counter-ion at lower pH causes an increase in head group size and makes the overall lipid shape less conical, as seen in Figure 4.11(c). Less conical ePA lipids, pH 6, pack together more tightly, which reduces insertion of TX into liposomes. Conversely, more conical ePA lipids, pH 8, have more defects in liposome layers that ease the incorporation of TX. As discussed with ePC liposomes, fewer defects in liposome bilayers result in a lower association of TX monomers before liposomes begin restructuring into mixed-micelles.

In summary, these results show that a lipid shape model can be used to explain detergent solubilization characteristics of single-lipid and mixed-lipid liposomes, which is a necessary early step in creating native-like liposomes that incorporate proteins for functional purpose.

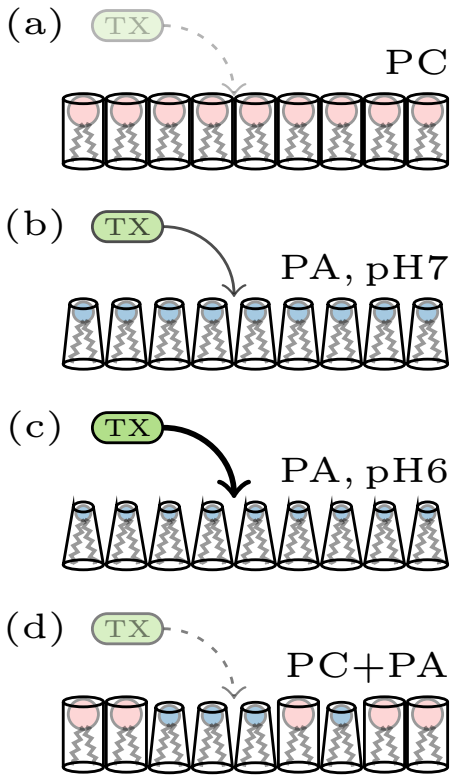

Figure 4.11: Illustration of the influence of lipid shape in the outer liposomes leaflet on TX incorporation.

References

[1] Hasna Ahyayauch et al. "Detergent solubilization of phosphatidylcholine bilayers in the fluid state: Influence of the acyl chain structure". In: *Biochimica et Biophysica Acta - Biomembranes* 1758 (2006), pp. 190–196.

[2] Hasna Ahyayauch et al. "Lipid bilayers in the gel phase become saturated by Triton X-100 at lower surfactant concentrations than those in the fluid phase". In: *Biophysical Journal* 102.11 (2012), pp. 2510–2516.

[3] Thomas M. Bayer, Gerd Dieter Werner, and Erich Sackmann. "Solubilization of DMPC and DPPC vesicles by detergents below their critical micellization concentration". In: *Biochimica et Biophysica Acta* 984 (1989), pp. 214–224.

[4] J Cladera et al. "Functional reconstitution of Photosystem I reaction center from cyanobacterium Synechocystis sp PCC 6803 into liposome using a new reconstitution procedure". In: *Journal of Bioenergetics and Biomembranes* 28.6 (1996), pp. 503–515.

[5] Magali Deleu et al. "Complementary biophysical tools to investigate lipid specificity in the interaction between bioactive molecules and the plasma membrane: A review". In: *Biochimica et Biophysica Acta - Biomembranes* 1838 (2014), pp. 3171–3190.

[6] Allison Dickey and Roland Faller. "Examining the contributions of lipid shape and headgroup charge on bilayer behavior". In: *Biophysical Journal* 95 (2008), pp. 2636–2646.

[7] William Dowhan, Mikhail V. Bogdanov, and Eugenia Mileykovskaya. "Functional Roles of Lipids in Membranes". In: *Biochemistry of Lipids, Lipoproteins and Membranes*. Ed. by Neale D. Ridgway and Roger S. McLeod. 6th ed. Elsevier, 2015, pp. 1–40.

[8] Piotr Draczkowski, Dariusz Matosiuk, and Krzysztof Jozwiak. "Isothermal titration calorimetry in membrane protein research". In: *Journal of Pharmaceutical and Biomedical Analysis* 87 (2014), pp. 313–325.

[9] Zoltan Gombos et al. "Characterization of the Fad12 mutant of Synechocystis that is defective in 12 acyl-lipid desaturase activity Zoltan". In: *Biochimica et Biophysica Acta* 1299 (1996), pp. 117–123.

[10] Bradley J. Harris, Xiaolin Cheng, and Paul Frymier. "Structure and Function of Photosystem I-[FeFe] Hydrogenase Protein Fusions: An All-Atom Molecular Dynamics Study". In: *Journal of Physical Chemistry B* 120.4 (2016), pp. 599–609.

[11] Bradley J Harris, Xiaolin Cheng, and Paul Frymier. "All-Atom Molecular Dynamics Simulation of a Photosystem". In: *Journal of Physical Chemistry B* 118 (2014), pp. 11633–11645.

[12] Helmut Hauser and Guy Poupart. *The Structure of Biological Membranes*. Ed. by Philip L. Yeagle. 2nd ed. Boca Raton, Fla.: CRC Press, 2005, pp. 38–40.

[13] Heiko Heerklotz, Alekos D. Tsamaloukas, and Sandro Keller. "Monitoring detergent-mediated solubilization and reconstitution of lipid membranes by isothermal titration calorimetry". In: *Nature Protocols* 4.5 (2009), pp. 686–697.

[14] Jonas R. Henriksen et al. "Understanding detergent effects on lipid membranes: A model study of lysolipids". In: *Biophysical Journal* 98 (2010), pp. 2199–2205.

[15] Annegret Hildebrand et al. "Solubilization of negatively charged DPPC/DPPG liposomes by bile salts". In: *Journal of Colloid and Interface Science* 279 (2004), pp. 559–571.

[16] J. N. Israelachvili, S. Marcelja, and R. G. Horn. "Physical principles of membrane organization". In: *Quarterly Reviews of Biophysics* 13.2 (1980), pp. 121–200.

[17] Ifeyinwa J. Iwuchukwu et al. "Self-organized photosynthetic nanoparticle for cell-free hydrogen production". In: *Nature Nanotechnology* 5 (2010), pp. 73–79.

[18] Jan Knol, Klaas Sjollema, and Bert Poolman. "Detergent-mediated reconstitution of membrane proteins". In: *Biochemistry* 37 (1998), pp. 16410–16415.

[19] Edgar E. Kooijman et al. "Modulation of membrane curvature by phosphatidic acid and lysophosphatidic acid". In: *Traffic* 4 (2003), pp. 162–174.

[20] Ulrich Kragh-hansen, Marc Maire, and Jesper V Møller. "The Mechanism of Detergent Solubilization of Liposomes and Protein-Containing Membranes". In: *Biophysical Journal* 75.6 (1998), pp. 2932–2946.

[21] V V Kumar. "Complementary molecular shapes and additivity of the packing parameter of lipids". In: *Protocol National Acadamy of Science USA* 88.January (1991), pp. 444–448.

[22] Katariina Lähdesmäki et al. "Membrane simulations mimicking acidic pH reveal increased thickness and negative curvature in a bilayer consisting of lysophosphatidylcholines and free fatty acids". In: *Biochimica et Biophysica Acta - Biomembranes* 1798.5 (2010), pp. 938–946.

[23] Rosemary K. Le et al. "Analysis of the solution structure of Thermosynechococcus elongatus Photosystem I in n-dodecyl-β-d-maltoside using small-angle neutron scattering and molecular dynamics simulation". In: *Archives of Biochemistry and Biophysics* 550-551 (2014), pp. 50–57.

[24] Rosemary K. Le et al. "Sortase-mediated ligation of PsaE-modified Photosystem I from Synechocystis sp. PCC 6803 to a conductive surface for enhanced photocurrent production on a gold electrode". In: *Langmuir* 31.3 (2015), pp. 1180–1188.

[25] A. G. Lee. "Lipid-protein interactions in biological membranes: A structural perspective". In: *Biochimica et Biophysica Acta - Biomembranes* 1612.1 (2003), pp. 1–40.

[26] Dov Lichtenberg. "Characterization of the solubilization of lipid bilayers by surfactants". In: *BBA - Biomembranes* 821.3 (1985), pp. 470–478.

[27] Dov Lichtenberg, Robert J. Robson, and Edward A. Dennis. "Solubilization of phospholipids by detergents structural and kinetic aspects". In: *BBA - Reviews on Biomembranes* 737.2 (1983), pp. 285–304.

[28] Dov Lichtenberg et al. "Detergent solubilization of lipid bilayers: A balance of driving forces". In: *Trends in Biochemical Sciences* 38.2 (2013), pp. 85–93.

[29] P. Losada-Pérez et al. "Phase transitions of binary lipid mixtures: A combined study by adiabatic scanning calorimetry and quartz crystal microbalance with dissipation monitoring". In: *Advances in Condensed Matter Physics* 2015 (2015), p. 14.

[30] R N McElhaney. “The use of differential scanning calorimetry and differential thermal analysis in studies of model and biological membranes.” In: *Chemistry and Physics of Lipids* 30.2-3 (1982), pp. 229–259.

[31] D A N Morris et al. “Interaction of lysophosphatidylcholine with phosphatidylcholine bilayers.” In: *Biochim. Biophys. Acta.* 599 (1980), pp. 380–390.

[32] Mohammad Hadi Nematollahi et al. “Changes in physical and chemical properties of niosome membrane induced by cholesterol: A promising approach for niosome bilayer intervention”. In: *Royal Society of Chemistry Advances* 7 (2017), pp. 49463–49472.

[33] Hanieh Niroomand, Dibyendu Mukherjee, and Bamin Khomami. “Tuning the photoexcitation response of cyanobacterial Photosystem I via reconstitution into proteoliposomes”. In: *Scientific Reports* 7.865 (2017), pp. 1–13.

[34] Ryan C. Oliver et al. “Dependence of micelle size and shape on detergent alkyl chain length and head group”. In: *PLoS ONE* 8.5 (2013), pp. 1–10.

[35] M. Aránzazu Partearroyo et al. “Solubilization of phospholipid bilayers by surfactants belonging to the Triton X series: Effect of polar group size”. In: *Journal of Colloid and Interface Science* 178.1 (1996), pp. 156–159.

[36] Marie-Therese Paternostre, Michel Roux, and Jean-Louis Rigaud. “Mechanisms of membrane protein insertion into liposomes during reconstitution procedures involving the use of detergents. 1. Solubilization of large unilamellar liposomes (prepared by reverse-phase evaporation) by Triton X- 100, Octyl Glucoside, and Sodiu”. In: *Biochemistry* 27.8 (1988), pp. 2677–2688.

[37] Antonio Pizzirusso et al. “Biomembrane solubilization mechanism by Triton X-100: A computational study of the three stage model”. In: *Physical Chemistry Chemical Physics* 19.44 (2017), pp. 29780–29794.

[38] Jean Louis Rigaud, Bruno Pitard, and Daniel Levy. “Reconstitution of membrane proteins into liposomes: application to energy-transducing membrane proteins”. In: *BBA - Bioenergetics* 1231.3 (1995), pp. 223–246.

[39] Annela M. Seddon, Paul Curnow, and Paula J. Booth. "Membrane proteins, lipids and detergents: not just a soap opera". In: *Biochimica et Biophysica Acta - Biomembranes* 1666.1-2 (2004), pp. 105–117.

[40] John J H Shin and Christopher J R Loewen. "Putting the pH into phosphatidic acid signaling". In: *BioMed Central Biology* 85.9 (2011), pp. 1–10.

[41] John R. Silvius. "Solubilization and functional reconstitution of bioemembrane components". In: *Annual Review of Biophysics and Biomolecular Structure* 21 (1992), pp. 323–348.

[42] Liang Sun et al. "Coarse-grained molecular dynamics simulation of interactions between cyclic lipopeptide Bacillomycin D and cell membranes". In: *Molecular Simulation* 44.5 (2018), pp. 346–376.

[43] Francis Szoka Jr. and Demetrios Papahadjopoulos. "Comparative properties and methods of preparation of lipid vesicles (liposomes)". In: *Annual Review of Biophysics and Bioengineering* 9 (1980), pp. 467–508.

[44] Ting Zhang et al. "Effect of pH and salt on surface pKa of phosphatidic acid monolayers". In: *Langmuir* 34 (2018), pp. 530–539.

Chapter 5

Prediction Model for Saturation of Bimodal Liposome Systems and Detergent Binding Events

This chapter is revised based on a paper to be submitted by Samantha Clark, Matthias M. L. Arras, Andy Sarles, and Paul Frymier. My primary contributions to the paper include: (1) development of the problem into a work, (2) identification of the study areas and objectives, (3) design and conducting of the experiments, (4) gathering and recording measurements, (5) processing, analyzing and interpretation of experimental data, (6) pulling reviewer contributions into a single papers, and (7) writing and editing.

Abstract

In this paper, liposome mixtures prepared from varying ratios of egg phosphotidylcholine (ePC) and egg phosphatidic acid (ePA) were solubilized with the detergent, Triton X-100 (TX). During solubilization, liposomes incorporate detergent between the lipids. The maximum detergent concentration that liposomes can incorporate before they initiate disruption into mixed-micelles is called the saturation concentration, D_{sat}. Determination of D_{sat} is critical in processes like detergent-mediated protein reconstitution into liposomes. For many single liposome systems, D_{sat} has been well-characterized; however the effect of mixtures of liposomes on detergent solubilization is not yet known. Natural systems contain a multitude of membrane types, composed of varying lipid constituents and ratios. Understanding the association of small molecules with a bimodal combination of membrane types present is important for drug targeting and delivery. For this reason, solubilization experiments have been performed and an equilibrium model was derived that describes the data well without requiring non-physical fitting parameters. It requires only the knowledge of the relationship between liposome size change due to detergent uptake and measured signal (e.g. absorbance spectrophotometry signal). Additionally, this model determines the number of detergent molecules present per each liposome population at saturation. This can be utilized in drug delivery applications and solubilization of membranes in cells.

5.1 Introduction

One method that nature uses to regulate the binding of small molecules with cells and organelles is tuning lipid compositions to encourage increased association [7]. Similarly, detergents are known to bind with increased affinity to synthetic liposomes comprised of certain lipid compositions [16]. This has been well studied for a wide range of interactions between lipids like phosphatidylcholine (PC), phosphatidic acid (PA), and phosphatidylglycerol, and detergents like Triton X-100 (TX), dodecyl maltoside, octyl glucoside, and cholamidopropyl dimethylammonio propanesulfonate both experimentally [5, 2, 6, 1, 17, 4, 10, 11, 13], and using computational molecular dynamics simulations [22, 18]. Amongst these, a common three-stage model for detergent incorporation and disassembly of liposomes has been proposed [15, 21, 19]; it is demonstrated in Figure 5.1. In this model, detergent molecules (●) spontaneously incorporate into liposomes (● and ●) upon titration at a fixed lipid concentration increasing the average liposome diameter until the bilayers are saturated with detergent at concentration D_{sat}. Increasing the detergent concentration above D_{sat} leads to partial solubilization characterized by the coexistence of mixed lipid-detergent micelles and reduced-size liposomes. Liposomes become fully solubilized – as mixed lipid-detergent micelles – at a detergent concentration D_{sol}, above which particle size is constant. Rigaud *et al.* developed an empirical method to predict D_{sat} and D_{sol} at any lipid concentration; it is stated as $D_{\text{total}} = D_{\text{water}} + R_{\text{eff}} \cdot [\text{lipid}]$ [24]. In this method, D_{total} is the total concentration of detergent at either D_{sat} and D_{sol}, D_{water} is the concentration of detergent in solution that is not associated with lipids, and $R_{\text{eff}} \cdot [\text{lipid}]$ is a reference value for saturation or solubilization times the lipid concentration. Several other models have also been fitted to this process [25, 3, 9, 8, 10]. Additionally, Kryvola *et al.* estimate the surface density of detergent molecules on each liposome [14]. Each of these models only considers homogeneous liposome populations, and the effect of multiple liposome populations on detergent binding affinity is yet unknown. This effect is an important factor for drug delivery in cells, which contain multiple membranes. Thus, detergent-lipid binding in a bimodal liposome-type system was investigated using absorbance spectrophotometry and dynamic light scattering. Additionally, an equilibrium model was derived to predict D_{sat},

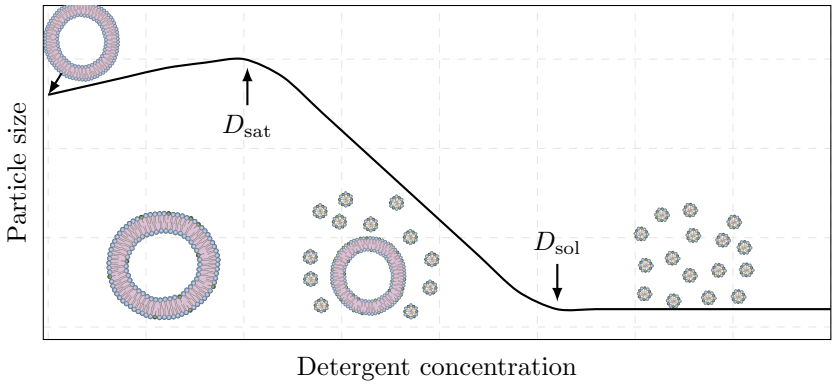

Figure 5.1: Demonstration of morphological changes in detergent solubilization of liposomes observed throughout turbidity measurements with absorbance spectrophotometry recorded at 400 nm. Based on Seddon *et al.* [20].

and other solubilization points, for different ratios of liposomes in the bimodal system. The model also predicts the detergent-lipid ratio for each lipid type and it can be applied to other bimodal or multi-modal mixtures.

5.2 Materials and Methods

5.2.1 Materials

Buffers were prepared from potassium phosphate, sodium sulfate, and potassium sulfate, all purchased from Fisher Scientific. Aqueous buffer solutions for all experiments contained 25 mM KH_2PO_4-KOH pH 7, 50 mM Na_2SO_4, and 50 mM K_2SO_4. Powder lipids were purchased from Avanti Polar Lipids, Inc. These included 1,2-dipalmitoyl-sn-glycero-3-phosphochline (16:0 PC), 1,2-dipalmitoyl-sn-glycero-3-phosphate (sodium salt) (16:0 PA), chicken egg phosphatidylcholine (ePC), and chicken egg phosphatidic acid (ePA). Triton X-100 detergent (¡3 % polyethylene glycol) and chloroform (99.8 % pure) were purchased from Sigma-Aldrich. Detergent and lipids were used without further purification.

5.2.2 Liposome Preparation

Lipid powders were separately dissolved in chloroform and dried in desired aliquots overnight under vacuum desiccation so that a thin lipid film formed on the flask walls.

The prepared lipid films were stored at -20 °C . Just prior to use, lipid films were hydrated in a potassium phosphate buffer, pH 7.2, containing 25 mM KH_2PO_4-KOH pH 7, 50 mM Na_2SO_4, and 50 mM K_2SO_4. Samples were heated above melting temperature (T_m) and vortexed to thoroughly suspend the lipids and form multi-lamellar vesicles (MLVs) [23]. MLVs were subjected to a freeze-thaw cycle (-20 °C to 10 °C above lipid T_m) four times, and then mixed and diluted to the chosen concentration of each lipid. Bimodal preparations were made by combining the two lipid MLV solutions and then extruding above the T_m for every lipid in the mixture. Extrusion was performed with the Avanti Mini-Extruder system housed with a Whatman 100 nm Nuclepore Track-Etch membrane (model 800309) to form large unilamellar vesicles (LUVs). All liposome preparations were used immediately for subsequent experiments.

5.2.3 Differential Scanning Calorimetry

Differential scanning calorimetry (DSC) was used to determine the melting temperature(s), which can be used to observe the number of MLV populations in solution. DSC samples were prepared as outlined in subsection 5.2.2 in the initial steps of liposome preparation. Powdered lipids of 16:0 PC and 16:0 PA were individually dissolved in chloroform and aliquoted and dried under vacuum. The PC lipid cake and PA lipid cake were then hydrated in buffer to form PC MLVs and PA MLVs. For each sample, MLVs were extruded, mixed, and diluted to 4 mg lipid / ml in buffer as stated in the results section 5.3.1. The 1:1 PC-PA mixed-lipid MLVs sample was prepared by combining 16:0 PC and 16:0 PA in chloroform prior to drying and solubilizing in buffer. Each sample and deionized water reference were placed under vacuum for 15 minutes with a stir bar rotating at 600 rpm to degas prior to use. Measurements were made using a TA Instruments' NanoDSC calorimeter with 0.5 mL chambers at 0.3 MPa. Samples were equilibrated at 30 °C for 110 minutes before and in-between each of the 3 heating-cooling cycles, which ran from 30 to 70 °C at scan rates of 1, 0.25, and 0.25 °C/min.

5.2.4 Absorbance Spectrophotometry

The detergent saturation and solubilization concentrations of prepared liposome solutions were determined using absorbance spectrophotometry by measuring changes in turbidity with increasing detergent to lipid (D:L) ratio. This technique observes size dependent changes in absorbance, commonly referred to as Mie-scattering, that occurs during liposome solubilization. For these measurements, liposomes were prepared and equilibrated for 30 minutes. Liposome aliquots were then mixed with TX dilutions at 0 – 20 mM TX to prepare D:L ratios ranging from 0 – 4 mol/mol. The final concentration of the lowest TX-liposome solution was an order of magnitude above the critical micelle concentration of the detergent. The prepared emulsions were equilibrated 30 minutes at room temperature prior to taking absorbance measurements using a Thermo-Scientific NanoDrop 2000C spectrophotometer. A full UV-Vis sweep of each sample ensured there were no irregularities in the sample placement on the pedestal reader, and turbidity data were recorded at a wavelength of 400 nm. Three measurements were taken for each duplicate sample, then averaged and normalized to an initial liposome absorbance of 1 for the final sample absorbance. For each PC:PA lipid composition, three sample sets were taken. An average and standard deviation from these are reported. D_{sat} and D_{sol} were determined from solubilization curves using the detergent concentration at the peak absorbance and the detergent concentration beyond which absorbance no longer changes significantly with increasing detergent.

5.2.5 Dynamic Light Scattering

To compliment turbidity measurements, dynamic light scattering (DLS) was performed to determine the particle size and distribution at concentrations of interest, including extruded liposomes with no TX and fully solubilized liposomes. DLS samples were prepared in the same manner as for absorbance spectrophotometry. Measurements were taken on a Wyatt Technology DynaPro NanoStar fixed angle dynamic light scattering instrument with 20 x 10 second acquisitions at 20 °C. Three sample sets with duplicates were observed for each lipid-detergent composition. Data were fit to a standard isotropic sphere model at optimal resolution, and it is displayed as an average at each TX concentration and lipid composition.

5.3 Results and Discussion

5.3.1 Differential Scanning Calorimetry

The objective of DSC was to demonstrate control over the creation of mixed-lipid liposomes vs multiple populations of single lipid type liposomes. It was performed on model PC and PA lipids with saturated 16 carbon chains (16:0), because, unlike ePC and ePA, which contain a variety of fatty acid chains, the melting temperatures of these species are significantly above 0 °C. Transitions above liquid freezing making them ideal for liquid DSC. Additionally, 16:0 is the most common fatty acid chain in ePC and ePA, comprising 33 and 34 mol% based on analysis by Avanti Polar Lipids, Inc.

Figure 5.2(a) demonstrates the melting temperatures of a pure PC solution and a pure PA solution. The lipids are in the form of multilamellar vesicles (MLVs), which is the precursor to extrusion to form unilamellar liposomes of a similar diameter. In DSC, MLVs yield a narrow enthalpic peak and are standard for measuring lipid transition temperatures. In Figure 5.2(a), transition temperatures of MLVs are determined by the molar heat capacity (MHC) peaks for 16:0 PC (—) and 16:0 PA (—). The peaks are distinctly separated by 22 °C. The major transition of 16:0 PC is at 42 °C and of 16:0 PA is at 64 °C. Additionally, 16:0 PC has a pre-transition at 35 °C. These values are substantiated by literature values [23]. A mixture of these two MLV solutions is also shown in Figure 5.2(a) with 50:50 16:0 PC MLVs: 16:0 PA MLVs (—). This shows distinct transition peaks for both lipids at nearly the same temperatures (42 °C and 64 °C) as for the pure lipids. Thus there was limited if at all mixing of lipids between the two MLV populations when they were together. Later experiments look at the saturation and solubilization of detergent on two separate populations of liposomes, which are formed through extrusion of such a mixture of MLVs. Therefore, the mixture of 50:50 16:0 PC MLVs: 16:0 PA MLVs was extruded to observe if further processing causes mixing of lipids between membranes. An extruded mixture of 50% 16:0 PC MLVs and 50% 16:0 PA MLVs (—) in Figure 5.2(b) shows that there was broadening of the thermal transition region or MHC curves. The single bilayer has fewer lipids to coordinate a transition together, which results in a broader transition region. In multilamellar systems, the coordinated transition releases more energy at the same time.

There are two distinct curves for each of the lipid types and the curves are separated by nearly 5 °C. This indicates that very little mixing occurs during the extruding process, and there are two populations of liposomes. An alternative preparation would be to extrude lipid types separately and then mix them together. The DSC data may show some degree of interliposome mixing, but MLV's were extruded together to obtain LUVs that better suit the conditions of the liposomes.

As a control to verify that DSC would distinguish if there were a single liposome population containing both lipids in lipid bilayers, a preparation known to produce this was followed. It involved mixing 16:0 PC and 16:0 PA lipids together in an organic solvent, drying the mixture under vacuum and solubilizing the lipid cake in buffer. In Figure 5.2(b), DSC of the two lipids dried and hydrated together, called 50:50 PC:PA mixed-lipid MLVs, has one broad transition region at 54 °C (—). Thus, this preparation produced a population of liposomes with both lipids mixed together in the bilayers, whereas the before-mentioned 50:50 16:0 PC MLVs:16:0 PA MLVs produces a bimodal system of two distinct liposome populations. Subsequently discussed liposomes preparations follow the protocol for the extruded mixture of 50:50 16:0 PC MLVs: 16:0 PA MLVs sample in which pre-hydrated lipid MLVs are mixed, and then extruded together forming two distinct liposome populations.

5.3.2 Spectrophotometry Demonstrating Association of TX with a Mixed Liposome Solution

The changes in the morphology of liposomes at increasing ratios of TX were observed using absorbance spectrophotometry at 400 nm, predominantly through Mie-scattering. Here, larger particles scatter more light than smaller particles, which is observed as increased absorbance. Changes in liposome morphology as the D:L ratio increases are schematically depicted in Figure 5.1 with an illustrated absorbance curve. The schematic shows that TX molecules partition and incorporate lipid bilayers, causing an increase in diameter until liposomes are saturated with detergent, D_{sat}. After they are saturated, increasing the TX concentration with fixed lipid concentration causes budding of mixed-lipid and detergent-micelles and liposomes reduce in size. At D_{sol}, liposomes are completely solubilized into

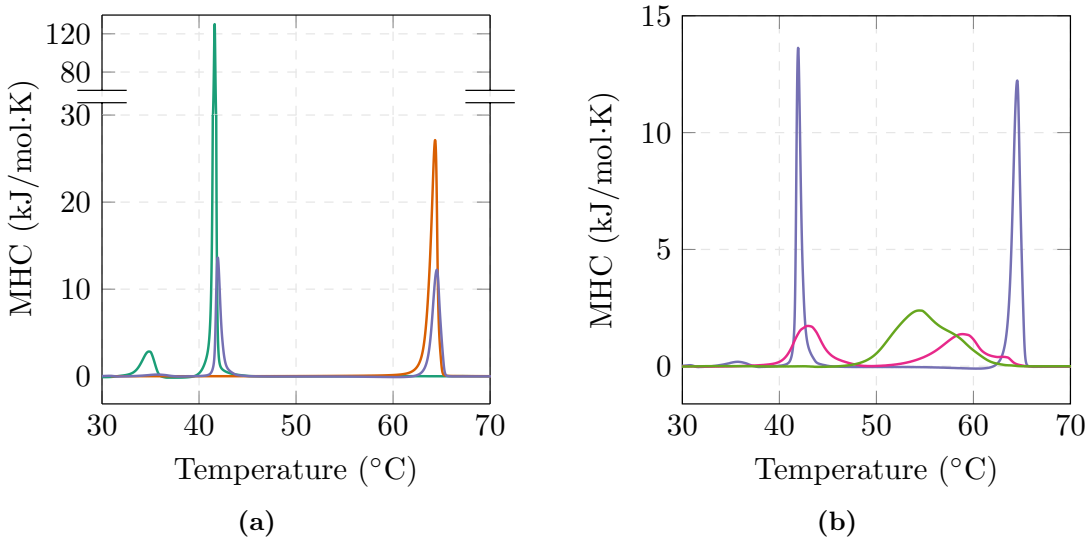

Figure 5.2: Lipid bilayer transitions using DSC of (a) PC MLVs (—), PA MLVs (—), and a 50:50 16:0 PC MLVs: 16:0 PA MLVs (—), and (b) an extruded mixture of 50:50 16:0 PC MLVs: 16:0 PA MLVs (—), 50:50 PC:PA mixed-lipid MLVs (—), and mixture of 50% 16:0 PC MLVs and 50% 16:0 PA MLVs (—), as in (a). All samples contain 4 mg lipid /ml.

mixed-micelles. Further increasing TX concentration has no impact on particle size or absorbance.

In this paper, mixed liposome systems were prepared from ePC and ePA liposomes at ratios of 100:0, 75:25, 50:50, 25:75, and 0:100 ePC:ePA, in which there were two distinct populations of liposomes for each lipid. The liposomes mixtures were combined with TX. Then absorbance was measured to gain insight into the size shifts when multiple populations are present. Figure 5.3 shows the solubilization curves observed for three sample sets each. The curves each follow the expected trend shown in Figure 5.1.

The lowest peak absorbance and the lowest D_{sat}, 1.1 mM TX, were observed for pure ePC liposomes (100:0 ePC:ePA), (•). In the 100:0 ePC:ePA sample, absorbance reduces with TX concentration until it baselines at D_{sol}= 7 mM TX. The 100:0 ePC:ePA sample swelled to saturation with TX at nearly 1.5 times the normalized absorbance of the initial lipid only liposomes. The TX concentration at D_{sat} was 2.7 mM TX, which was over twice as much TX as for ePC (•). At TX concentrations higher than D_{sat}, the slope of the solubilization curve in Stage II was less steep than for ePC only liposomes. The absorbance reached a baseline

at 12.15 mM TX. Additionally, Stage II lasted over a larger range of TX concentrations than for ePC only (9.45 vs. 6.92 mM).

The solubilization curves in Figure 5.4 for solutions containing a mixture of ePA liposomes and ePC liposomes were observed to lie between the individual liposome curves. At first glance, the curves appear to increase monotonically with increase in ePA concentration in that the sample containing 75:25 ePC:ePA liposomes has little increase in absorbance in Stage I, and D_{sat} occurs at low TX concentration. Stage II for 75:25 ePC:ePA has a TX range similar to ePC only liposomes, and D_{sol} is at 1.2 mM TX. Similarly, the liposome mixture of 50:50 ePC:ePA has a higher maximum absorbance than 100:0 and 75:25 ePC:ePA. The D_{sat} of 50:50 ePC:ePA mixed liposomes is at 1.65 mM TX, which is slightly below the midpoint of the D_{sat} values of the individual liposome species. Likewise, D_{sol} of the 50:50 ePC:ePA mixture is also slightly above the midpoint of the D_{sol} of the individual species. The absorbance of the liposome mixture 25:75 ePC:ePA resembles most closely 0:100 ePA liposomes, in that the maximum absorbance is barely below that of ePA only (1.4 vs 1.24 mM). Similarly, Stage II proceeds over a TX range similar to ePA only liposomes and D_{sol} occurs at 9.9 mM TX.

The effect of the composition of liposomes on D_{sat} is graphed in Figure 5.4. As seen in the solubilization curves, D_{sat} increases with an increasing percentage of ePA liposomes. The weighted mean rule of mixtures was applied to the pure species data in Figure 5.4.

The equation for the weighted mean is $D^i_{\text{sat}} = x_i * D^A_{\text{sat}} + (1 - x_i) * D^B_{\text{sat}}$. For D_{sat}, the predictions based on weighted mean overpredicts the data. An ordinary least squares regression determined an r^2 value of 0.128. This $r^2$was calculated as the sum of squared difference between experimental data and predictive model at 25:75, 50:50, and 75:25 ePC:ePA. To find a better prediction of D_{sat} for mixtures of liposomes, an equilibrium model was derived and applied in Section 5.4.

5.3.3 Dynamic Light Scattering Demonstrating Association of TX with a Mixed Liposome Solution

DLS was used to determine that the two populations of ePC liposomes and ePA liposomes were the same size. The liposomes were prepared by extruding solubilized lipids through a

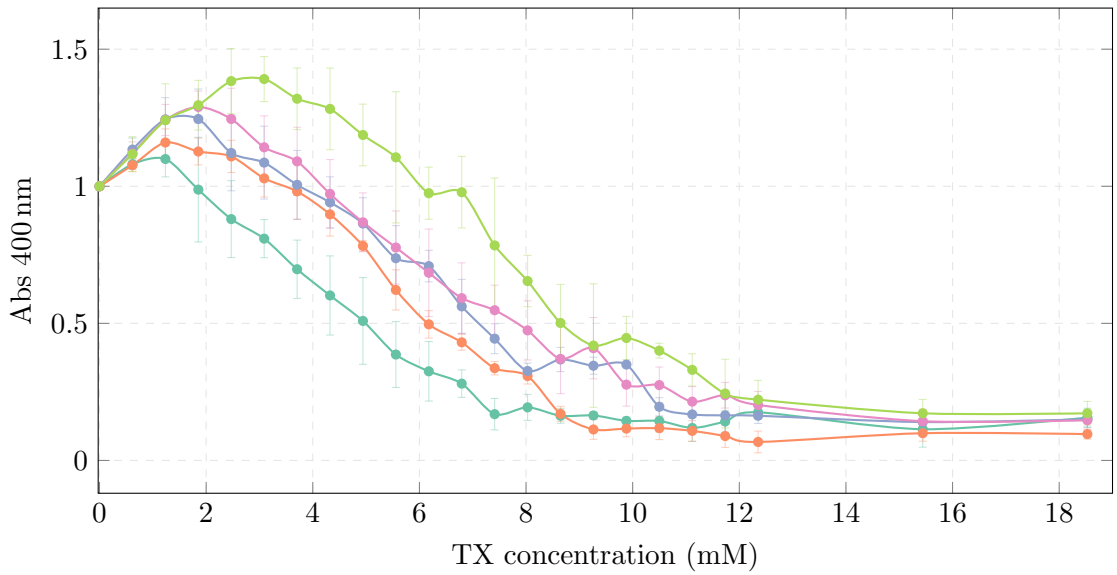

Figure 5.3: Turbidity changes in mixed liposome solutions at 100:0 (•), 75:25 (•), 50:50 (•), 25:75 (•), and 0:100 (•) ePC:ePA induced by TX detergent incorporation. Observed using absorbance spectrometry at 400 nm. Data point connecting lines are guides to the eye.

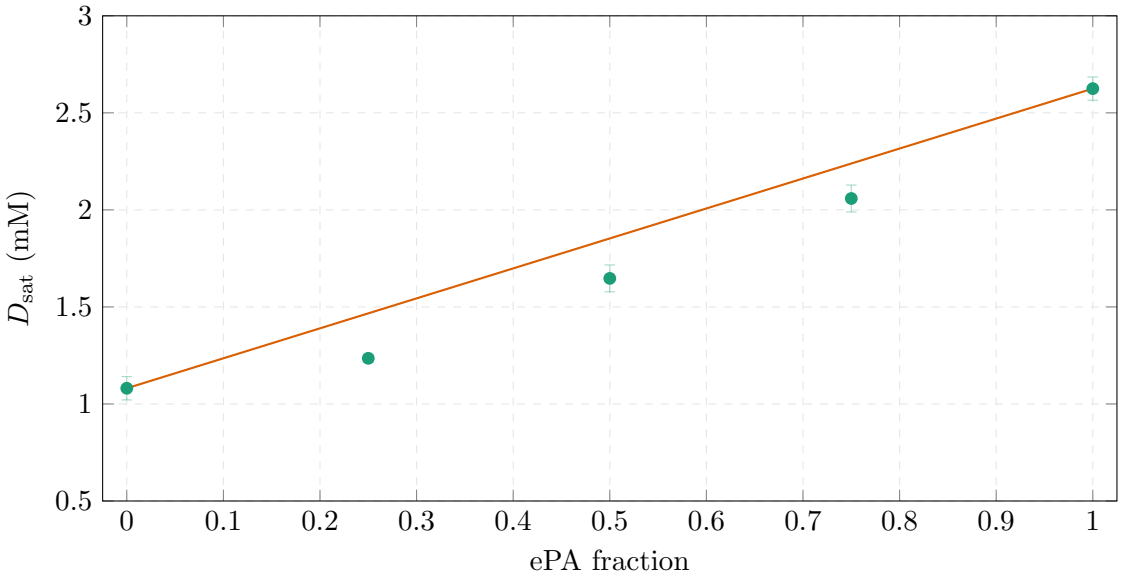

Figure 5.4: TX concentration at liposome saturation, D_{sat} for mixtures of ePC liposomes and ePA liposomes, displayed as the molar fraction of ePA liposomes, with the remaining fraction being ePC liposomes. Also shown is a weighted mean rule of mixtures fit to the D_{sat} of the pure liposome species (—).

100 nm pore membrane. In Figure 5.5, top row, the liposome populations of each sample composition were monodisperse in size. The average diameter of each sample is in Table 5.1. The average of the extruded liposome averages was 122.9 ± 3 nm. This corresponds with literature values for single liposome populations prepared by the same process. This shows that extruding multiple liposome populations with a similar average diameter, and the detergent solubilization process observed was not influenced by a variation in starting liposome size.

The size distributions of mixed-micelles for the varying lipid-liposome samples are also shown in Figure 5.5, bottom row. The populations were not two populations with different mean diameters. In Table 5.1, the average diameter of the solubilized liposomes, or mixed-micelles, is shown. Samples containing 0:100 ePC liposomes:ePA liposomes are slightly smaller in diameter than samples containing any ePC liposomes. This is explained by mixing of lipids in solution after solubilization between mixed-micelles. The lipid shape model in which ePA lipid molecules have a conical shape and ePC lipid molecules have a cylindrical shape [12]. These lipids enlarge the diameter of TX micelles from 11 ± 1 nm to 17 to 20 nm. In micelles of this size, the lipids are subjected to the effects of curvature. The conical shape of ePA packs with a smaller micellar diameter. Conversely, the cylindrical shape of ePC packs in micelles with a diameter several nanometers larger than ePA only. The cylindrical shape does not permit as tight of curvature in membranes as ePA [12], and this effect may carry over into micelles as well. Lipids in samples with mixtures of liposomes are thought to rearrange to form mixed-micelles contain ePC, ePA, and TX. With cylindrical lipids evenly distributed among micelles, the overall curvature due to packing decreases and the micellar diameter increases.

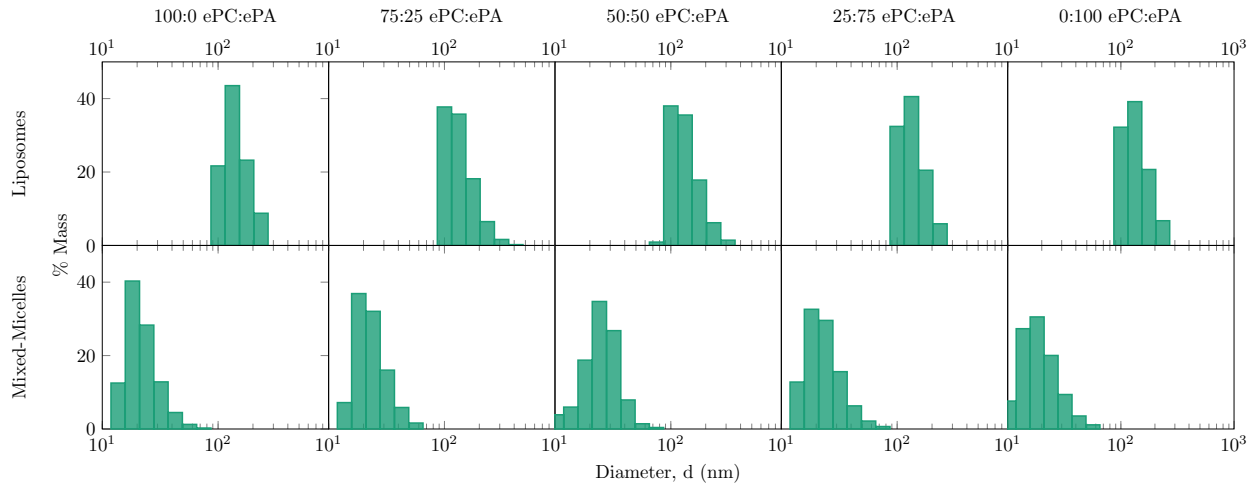

Figure 5.5: Particle size distribution measured using dynamic light scattering of mixed liposome samples after preparation (top row) and after complete solubilization, Stage III (bottom row).

Table 5.1: Diameter of mixed ePC and ePA liposomes, shown as ePC:ePA, after preparation and after solubilization in Stage III.

ePC:ePA	Liposomes d (nm)	Mixed-Micelles d (nm)
100:0	126.1 ± 2.8	19.9 ± 3.4
75:25	125.4 ± 1.5	18.1 ± 3.3
50:50	118.4 ± 4.7	19.7 ± 0.7
25:75	123.0 ± 2.7	19.4 ± 1.4
0:100	121.7 ± 3.5	17.8 ± 2.3

5.4 Equilibrium Model

As seen above, a simple weighted mean is not a good predictor of the concentration of detergent at saturation for a mixture of liposomes. A mechanistic model was derived to better predict the concentration of detergent that leads to saturation for mixed liposome solutions. Additionally, based on equilibria between liposomes and solubilized detergent this model allows estimation of the number of detergent sites filled at saturation in any mixture of these liposomes.

The derivation began with equilibrium expressions for detergent and liposomes in equations 5.1 and 5.2.

$$[A] + [D] \overset{K_A}{\rightleftharpoons} [D_A] \tag{5.1}$$

$$[B] + [D] \overset{K_B}{\rightleftharpoons} [D_B] \tag{5.2}$$

Here, $[A]$ and $[B]$ are the concentrations of $[ePC]$ and $[ePA]$ in liposomes, and $[D]$ is the concentration of detergent not bound to liposomes. The concentrations of detergent (TX in this case) bound to either A-type or B-type liposomes are then called $[D_A]$ or $[D_B]$, respectively. Then the equilibrium constants K_A and K_B were derived in equations 5.3 and 5.4.

$$K_A = \frac{[D_A]}{[A][D]} \tag{5.3}$$

$$K_B = \frac{[D_B]}{[B][D]} \tag{5.4}$$

In Stage I of liposome solubilization, all TX molecules ($[D_T]$) must be either free or in micelles ($[D]$) or incorporated into A-type or B-type liposomes ($[D_A]$ or $[D_B]$), therefore the mass balance for total detergent is described by equation 5.5.

$$[D_T] = [D] + [D_A] + [D_B] \tag{5.5}$$

Then the equations 5.3 and 5.4 are solved for $[D_A]$ and $[D_B]$ and substituted into the mass balance equation 5.5.

$$[D_T] = [D] + K_A[A][D] + K_B[B][D] \tag{5.6}$$

$[D]$ is isolated for an expression of detergent free or in micelles.

$$[D] = \frac{[D_T]}{1 + K_A[A] + K_B[B]} \tag{5.7}$$

This expression for $[D]$ is plugged into equation 5.5 for an expression to the total detergent concentration.

$$[D_T] = \frac{[D_T]}{1 + K_A[A] + K_B[B]} + K_A[A][D] + K_B[B][D] \tag{5.8}$$

This is simplified for a final expression describing the total concentration of detergent.

$$[D_T] = ([D_A] + [D_B])) \left(\frac{1 + K_A[A] + K_B[B]}{K_A[A] + K_B[B]} \right) \tag{5.9}$$

Equation 5.9 is then considered at saturation, which is denoted with an asterisk (*). As discussed above, liposomes are saturated at the maximum number of detergent molecules that can be incorporated before they begin splitting into mixed-micelles. This is shown in equation 5.9 and Figure 5.6 and

$$[D_T^*] = ([D_A] + [D_B])^* \left(\frac{1 + K_A[A] + K_B[B]}{K_A[A] + K_B[B]} \right) \tag{5.10}$$

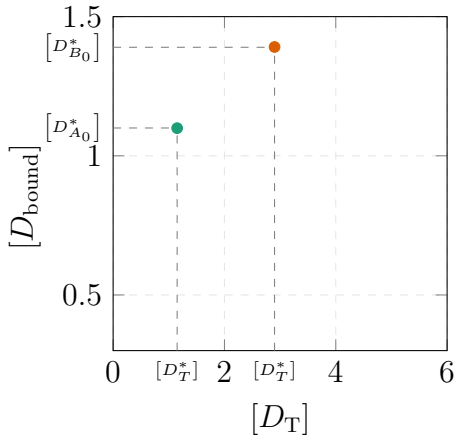

Figure 5.6: Graphical explanation of the relationship between total detergent and bound detergent at saturation for samples of pure A-type and pure B-type liposomes.

Assuming A-type liposomes and B-type liposomes do not mix significantly, and the presence of A-type liposomes does not affect the number of sites available for detergent adsorption in B-type liposomes (and vice-versa), then the total amount of detergent adsorbed at saturation is the sum of the number of sites available if all the lipids were pure A-type liposomes or B-type liposomes ($[A_0]$ or $[B_0]$). Here x_a and x_b are the mole fractions of lipid A and lipid B in the mixed liposome sample, and $[D^*_{A_0}]$ and $[D^*_{B_0}]$ are the molar concentrations of detergent bound to pure A-type or B-type liposomes at saturation.

$$([D_A] + [D_B])^* = x_a[D^*_{A_0}] + x_b[D^*_{B_0}] \tag{5.11}$$

Detergent incorporates into liposome bilayers between lipid molecules, thus the maximum number of detergent sites at saturation is a fraction less than or equal to 1 of the number of lipid molecules. n is used to represent the fraction of detergent sites on A-type liposomes or the detergent to lipid ratio at saturation.

$$[D^*_{A_0}] = n[A_0] \tag{5.12}$$

Similarly, m is used to represent the fraction of detergent sites on B-type liposomes.

$$[D^*_{B_0}] = m[B_0] \tag{5.13}$$

The detergent concentrations at saturation (D_{sat}) are related to the observed absorbance found during experimental solubilization of the pure liposome species. However, the relationship between the change in size caused by detergent uptake and the normalized change in absorbance for each liposome type is unknown. They are given the values γ and β for A-type and B-type liposomes, respectively.

$$[D^*_{A_0}] = n[A_0] \equiv \gamma(Abs^A_{\text{sat}}) \tag{5.14}$$

$$[D^*_{B_0}] = m[B_0] \equiv \beta(Abs^B_{\text{sat}}) \tag{5.15}$$

To compare the detergent to lipid ratio in each of the liposome species using absorbance, a constant α is assigned as a ratio of γ and β.

$$\frac{[D^*_{A_0}]}{[D^*_{B_0}]} = \frac{n[A_0]}{m[B_0]} \equiv \alpha\frac{(Abs^A_{\text{sat}})}{(Abs^B_{\text{sat}})} \tag{5.16}$$

This is rearranged such that the detergent concentration bound to B-type liposomes at saturation can be solved for using experimental absorbance data.

$$[D^*_{B_0}] \equiv \frac{n[A_0]}{\alpha}\frac{(Abs^B_{\text{sat}})}{(Abs^A_{\text{sat}})} \tag{5.17}$$

These two new relationships for $[D^*_{A_0}]$ and $[D^*_{B_0}]$ are inserted into equation 5.11 to find the concentration of detergent bound to A-type and B-type liposomes in a mixed system.

$$([D_A] + [D_B])^* = x_a n[A_0] + \frac{x_b n[A_0]}{\alpha}\frac{(Abs^B_{\text{sat}})}{(Abs^A_{\text{sat}})} \tag{5.18}$$

Now equation 5.18 is substituted into equation 5.9 for a final expression for the total amount of detergent at saturation in a mixture of two types of liposomes.

$$[D^*_T] = \left(x_a n[A_0] + \frac{x_b n[A_0]}{\alpha}\frac{(Abs^B_{\text{sat}})}{(Abs^A_{\text{sat}})}\right)\left(\frac{1 + K_A[A] + K_B[B]}{K_A[A] + K_B[B]}\right) \tag{5.19}$$

The equilibrium constants K_A and K_B are calculated from pure liposome data at saturation. The concentration of A-type liposomes does not change at saturation.

$$K_A = \frac{[D^*_{A_0}]}{[A_0][D^*]} \tag{5.20}$$

Using the mass balance in equation 5.5 at saturation, an expression for unbound detergent at saturation with only A-type liposomes present can be written.

$$[D^*] = [D^*_T] - [D^*_{A_0}] \tag{5.21}$$

This expression can be applied to equation 5.20, along with equation 5.12 to yield an expression for estimating the value of the equilibrium constant K_A for A-type liposomes.

$$K_A = \frac{n}{[D^*_T] - n[A_0]} \tag{5.22}$$

An expression for B-type liposomes can be derived in a similar fashion starting with the equivalent of equation 5.20 for B-type liposomes.

$$K_B = \frac{[D^*_{B_0}]}{[B_0][D^*]} \tag{5.23}$$

The mass balance in equation 5.5 at saturation also yields an expression for unbound detergent with only B-type liposomes present.

$$[D^*] = [D^*_T] - [D^*_{B_0}] \tag{5.24}$$

This expression can be applied to equation 5.23, along with equation 5.17, for a rate constant relationship for B-type liposomes.

$$K_B = \frac{1}{[B_0]\left(\frac{\alpha[D^*_{B_0}]}{n[A_0]}\frac{(Abs^A_{\text{sat}})}{(Abs^B_{\text{sat}})} - 1\right)} \tag{5.25}$$

Lastly, K_A and K_B are in the final expression for $[D^*_T]$ to determine the values of n and α that yield the best fit of equation 5.19 to the experimental data.

Table 5.2: Parameters used in solving equilibrium model for $[D_T^*]$.

Variable	Value
$[A_o]$	4.324
$[B_o]$	4.716
$[D^*_{A_0}]$	1.081
$[D^*_{B_0}]$	2.624
Abs^A_{sat}	0.010
Abs^B_{sat}	0.437

5.5 Equilibrium Model Results and Discussion

5.5.1 Solve for Relationship of Absorbance and TX Sites at $[D_T^*]$ at Best n and α Fits

Equations 5.19, 5.20, and 5.25 constitute an equilibrium model for predicting the concentration of detergent at saturation for a bimodal system of liposomes. The model needs only information about the saturation of the pure component liposomes, which is often readily available. The equilibrium model using experimental data found in Section 5.3.2 for 100 % ePC ($[A_0]$) and 100 % ePA ($[B_0]$). The detergent saturation and absorbance values from the section5.3.2 are used in the model and are listed in Table 5.2. The model was solved for the values of n and α that generate the best fit in the least squares sense to the data for $[D^{\text{exp}}_{\text{sat}}]$ at 25:75, 50:50, and 75:25 ePC:ePA.

Also, note that valid solutions for this model must avoid n and α values that yield non-possible denominators for K_A and K_B, that is, zero or negative values. These are represented by the gray areas in Figure 5.9, discussed later, where n must be less than 0.25 and $\frac{\alpha}{n}$ must be greater than 7.25. Additionally, an upper bound of $\alpha = 5$ was applied to the search algorithm; beyond this the solution diverged.

In Figure 5.8, the best solution to the equilibrium model is shown and compared with the previously mentioned weighted mean model. The parameter values of the best fit are of $\alpha = 2.7, n = 0.15$ for which the r^2 value is 0.00963. Here, r^2 was found as the sum of square of the differences between the experimental and model values for D_{sat}. This fit is closer to experimental values than the weighted mean model, $r^2 = 0.128$. The model collapses to

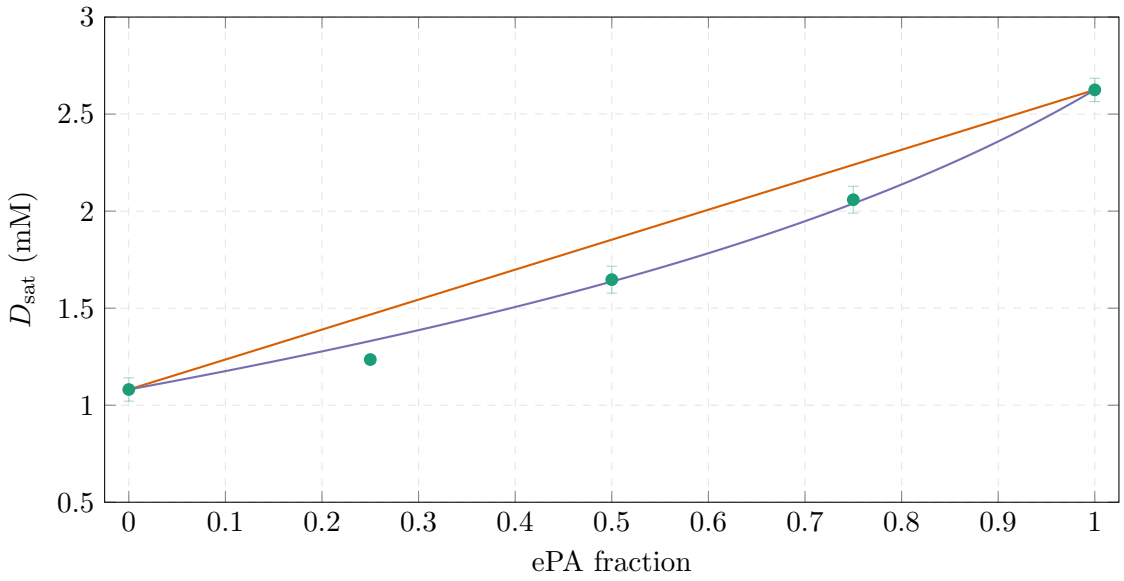

Figure 5.7: TX saturation of mixed liposomes at 0:1 to 1:0 mole fraction ePC:ePA determined by experiment (●), and fit with a mixing rule (——) and best model at $\alpha = 2.7, n = 0.15$ (——).

weighted averages at $\alpha = 1.8, n = 0.249$. Here K_A and K_B are also collapsing to 0, meaning no detergent incorporation is occurring.

Using $\alpha = 2.7$ and $n = 0.15$ with the above equations, it is possible to calculate the rate constant, K_A and K_B, and the number of detergent molecules incorporated into each of the liposome populations. Using this α and n in equations 5.22 and 5.25, K_A is 0.347 and K_B is 0.143. Additionally, these values mean that for every 100 ePC molecules in a saturated liposome, there are 15 TX molecules inserted into the bilayer. Thus the saturated liposomes are 13 mol% detergent and 87 mol% ePC lipids. Similarly, the detergent incorporation into ePA liposomes is analyzed by finding that $m = 0.455$ with equation 5.16. Therefore, the saturated liposomes are 31 mol% (molar) TX and 69 mol% ePA. This α and n can also be used to predict the D_T^* for different mixtures of bimodal liposomes.

A sensitivity analysis was performed in Figure 5.8. For this, the model was solved at $n = 0.15$ and α at half of 2.7 (——) and twice 2.7 (——). Half of the best-fit α ($n = 0.15$ & $\alpha = 1.35$) over-predicted D_T^* for the mixture, and twice the best-fit α ($n = 0.15$ & $\alpha = 5.4$) under-predicted D_T^*. Neither of these fits approached within a standard deviation of any

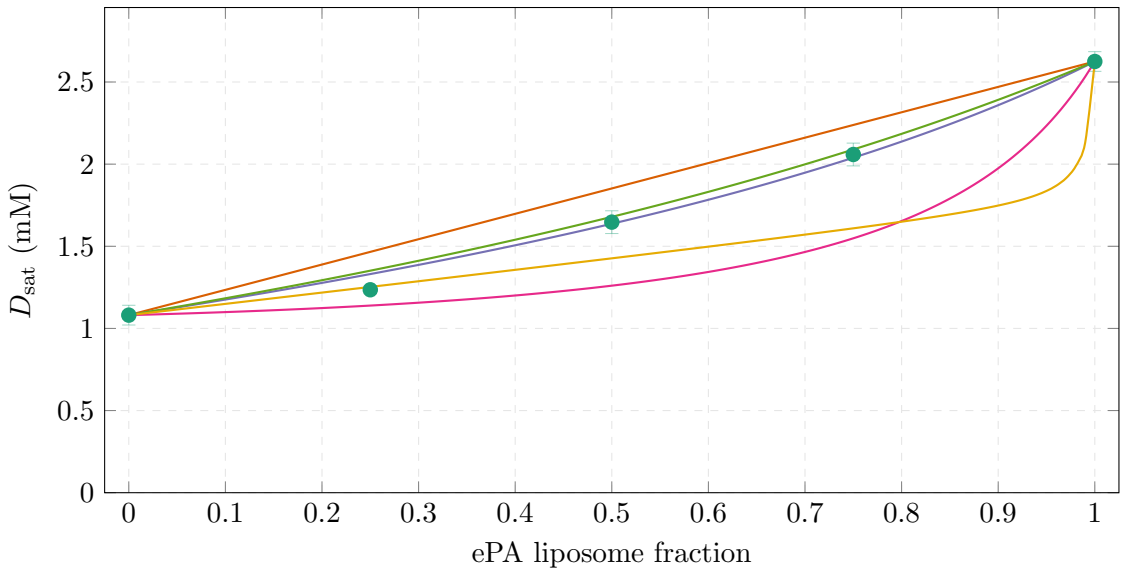

Figure 5.8: TX saturation of mixed liposomes at 0:1 to 1:0 mole fraction ePC:ePA as determined by experiment (●) and the equilibrium model at varying n and α: $n = 0.15$ & $\alpha = 2.7$ (—), $n = 0.15$ & $\alpha = 1.35$ (—), $n = 0.15$ & $\alpha = 5.4$ (—), $n = 0.05$ & $\alpha = 2.7$ (—), $n = 0.249$ & $\alpha = 2.7$ (—).

data point, but the deviation from the best-fit was more significant for a higher α value. This can be seen in terms of r^2 values in Table 5.3.

Similarly, the model was solved at $\alpha = 2.7$ and n at half (—) and nearly twice (—) that of the selected best fit (—). This high n value is near the maximum limit in which the denominator of K_A is less than or equal to zero. The curve for half of the best fit n, very slightly over-predicts D_T^*, therefore, the model is not sensitive to values of n less than the values identified as the best fit. The curve is within a standard deviation of the experimental data points at 50 and 75 % ePA liposomes. Nearly twice the best fit n significantly under-predicts D_T^* and has the highest r^2 value of the combinations sampled. It is not within a standard deviation of any experimental data points.

In Figure 5.9, the model is further is analyzed with a range of possible values for the parameters, n and α. Figure 5.9 (a) displays the fits for n and α as $1 - r^2$ to easily visualize the closeness of the predictions with the experimental data. There are two minimums for r^2. One lies along the K_B boundary line, and the other can be fit to a line, displayed in red (—).Around this line, the deviation from experimental data decreases as n approximates

Table 5.3: r^2 fit to experimental values for equilibrium model at select n and α from Figure 5.8 and the weighted mean model.

n	α	r^2
0.15	2.7	0.00963
0.15	1.35	0.128
0.15	5.4	0.419
0.075	2.7	0.0155
0.249	2.7	0.251
linear		0.128

towards zero. The best fit to the model for each n is better than the weighted mean fit. Of the best fit for each curve, the worst is at $n = 0.249, \alpha = 2.1$, in which $r^2 = 0.026$.

To better visualize the r^2 fit for the range of n and α, a color-coded scatter plot is shown in Figure 5.9(b). Gray areas represent non-physical solutions in which the denominators in equations 5.22 and 5.25 are less than or equal to zero. The two branches of potential solutions are represented by shades of blue and green dots. The primary branch starts at α near 3.5 and funnels to α near 2. A smaller branch is at the barrier region with K_B less than 0. The weighted mean model ($r^2 = 0.128$) would be in the orange region of this color bar.

5.6 Conclusions

In this paper, detergent solubilization is performed for a mixed population of ePC liposomes and ePA liposomes using absorbance spectrophotometry. The concentration of detergent at peak incorporation into liposomes was found from the apex of the solubilization curves. Next, a model is derived that fits experimental data using a binding equilibrium for two saturation events. The detergent saturation is assumed to be one liposome population that does not influence the saturation of the other and that the two liposome populations interact independently with TX. The model can determine the number of TX sites at saturation for each population. n and α were determined using the method of least squares, fitting the model to experimental data to find $[D_T^*]$. Once α has been determined, this model can be used to predict the number of detergent molecules associated with each population of liposomes at saturation. This model can be applied to any combination of liposomes.

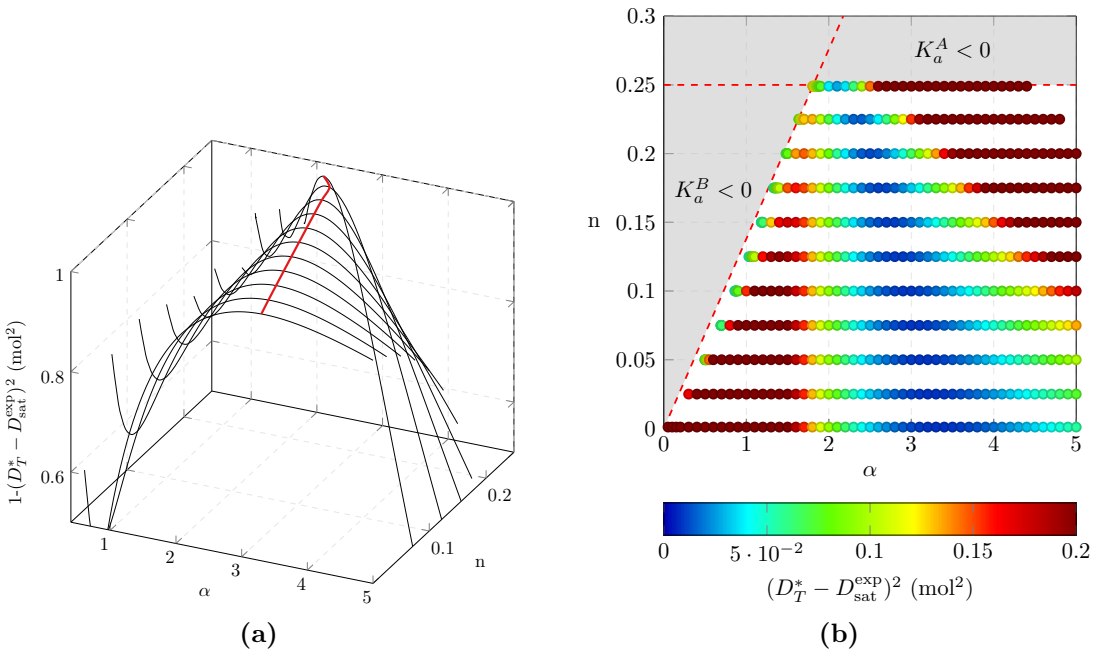

Figure 5.9: (a) XYZ plot for the model show the trend of the fit to experimental data, shown as $1 - r^2$ (1-$(D_T^* - D_{\text{sat}}^{\text{exp}})^2$), for a given n and α. The lowest r^2 for each n is shown with a line (—). (b) Least squares fit for D_T^* at given n and α values to experimental values, $D_{\text{sat}}^{\text{exp}}$. The color bar scale for the coefficient of determination is $r^2 = 0 - 0.2$

.

All that is needed is information on the detergent saturation of the individual liposome populations at the same lipid concentration. Additionally, this bimodal model could be expanded to include more than two liposomal species. These fits enable new insight into the number of TX detergent molecules that can be uptaken by liposomes of different species, and how bimodal mixtures of liposomes are saturated by detergent.

References

[1] Hasna Ahyayauch et al. "Detergent solubilization of phosphatidylcholine bilayers in the fluid state: Influence of the acyl chain structure". In: *Biochimica et Biophysica Acta - Biomembranes* 1758 (2006), pp. 190–196.

[2] Hasna Ahyayauch et al. "Lipid bilayers in the gel phase become saturated by Triton X-100 at lower surfactant concentrations than those in the fluid phase". In: *Biophysical Journal* 102.11 (2012), pp. 2510–2516.

[3] Alicia Alonso et al. "Kinetic studies on the interaction of phosphatidylcholine liposomes with Triton X-100". In: *Biochimica et Biophysica Acta* 902 (1987), pp. 237–246.

[4] Thomas M. Bayer, Gerd Dieter Werner, and Erich Sackmann. "Solubilization of DMPC and DPPC vesicles by detergents below their critical micellization concentration". In: *Biochimica et Biophysica Acta* 984 (1989), pp. 214–224.

[5] A De la Maza and Jose Luis Parra. "Vesicle-micelle structural transition of phosphatidylcholine bilayers and Triton X-100". In: *Biochemical Journal* 303 (1994), pp. 907–914.

[6] Allison Dickey and Roland Faller. "Examining the contributions of lipid shape and headgroup charge on bilayer behavior". In: *Biophysical Journal* 95 (2008), pp. 2636–2646.

[7] William Dowhan, Mikhail V. Bogdanov, and Eugenia Mileykovskaya. "Functional Roles of Lipids in Membranes". In: *Biochemistry of Lipids, Lipoproteins and Membranes*. Ed. by Neale D. Ridgway and Roger S. McLeod. 6th ed. Elsevier, 2015, pp. 1–40.

[8] Khalid Elamrani and Alfred Blume. "Incorporation Kinetics of Lysolecithin into Lecithin Vesicles. Kinetics of Lysolecithin-Induced Vesicle Fusion". In: *Biochemistry* 21 (1982), pp. 521–526.

[9] Hila Epstein et al. "Number-concentration of nanoparticles in liposomal and polymeric multiparticulate preparations: Empirical and calculation methods". In: *Biomaterials* 27 (2006), pp. 651–659.

[10] Jonas R. Henriksen et al. "Understanding detergent effects on lipid membranes: A model study of lysolipids". In: *Biophysical Journal* 98 (2010), pp. 2199–2205.

[11] Annegret Hildebrand et al. "Solubilization of negatively charged DPPC/DPPG liposomes by bile salts". In: *Journal of Colloid and Interface Science* 279 (2004), pp. 559–571.

[12] J. N. Israelachvili, S. Marcelja, and R. G. Horn. "Physical principles of membrane organization". In: *Quarterly Reviews of Biophysics* 13.2 (1980), pp. 121–200.

[13] Jan Knol, Klaas Sjollema, and Bert Poolman. "Detergent-mediated reconstitution of membrane proteins". In: *Biochemistry* 37 (1998), pp. 16410–16415.

[14] Oxana O. Krylova et al. "Pluronic L61 accelerates flip-flop and transbilayer doxorubicin permeation". In: *Chemistry European Journal* 9 (2003), pp. 3930–3936.

[15] Dov Lichtenberg, Robert J. Robson, and Edward A. Dennis. "Solubilization of phospholipids by detergents structural and kinetic aspects". In: *BBA - Reviews on Biomembranes* 737.2 (1983), pp. 285–304.

[16] Dov Lichtenberg et al. "Detergent solubilization of lipid bilayers: A balance of driving forces". In: *Trends in Biochemical Sciences* 38.2 (2013), pp. 85–93.

[17] M. Aránzazu Partearroyo et al. "Solubilization of phospholipid bilayers by surfactants belonging to the Triton X series: Effect of polar group size". In: *Journal of Colloid and Interface Science* 178.1 (1996), pp. 156–159.

[18] Antonio Pizzirusso et al. "Biomembrane solubilization mechanism by Triton X-100: A computational study of the three stage model". In: *Physical Chemistry Chemical Physics* 19.44 (2017), pp. 29780–29794.

[19] Jean Louis Rigaud, Bruno Pitard, and Daniel Levy. "Reconstitution of membrane proteins into liposomes: application to energy-transducing membrane proteins". In: *BBA - Bioenergetics* 1231.3 (1995), pp. 223–246.

[20] Annela M. Seddon, Paul Curnow, and Paula J. Booth. "Membrane proteins, lipids and detergents: not just a soap opera". In: *Biochimica et Biophysica Acta - Biomembranes* 1666.1-2 (2004), pp. 105–117.

[21] John R. Silvius. “Solubilization and functional reconstitution of bioemembrane components”. In: *Annual Review of Biophysics and Biomolecular Structure* 21 (1992), pp. 323–348.

[22] Liang Sun et al. “Coarse-grained molecular dynamics simulation of interactions between cyclic lipopeptide Bacillomycin D and cell membranes”. In: *Molecular Simulation* 44.5 (2018), pp. 346–376.

[23] Francis Szoka Jr. and Demetrios Papahadjopoulos. “Comparative properties and methods of preparation of lipid vesicles (liposomes)”. In: *Annual Review of Biophysics and Bioengineering* 9 (1980), pp. 467–508.

[24] Alice Verchère et al. “Reconstitution of membrane proteins in liposomes”. In: *Methods in Enzymology* 372.2000 (2003), pp. 65–86.

[25] Artem E. Zhirnov et al. “Lipid composition determines interaction of liposome membranes with Pluronic L61”. In: *Biochimica et Biophysica Acta - Biomembranes* 1720.1-2 (2005), pp. 73–83.

Chapter 6

Summary and Future Work

This dissertation has worked to advance systems that harness solar energy using a renewably sourced plant protein, PSI. It was demonstrated that PSI modified with an LPETG-peptide sequence on the stromal surface can be ligated to an enzyme containing the corresponding GGG-peptide sequence using sortase A. The rate of re-reduction of mutant PSI was also observed by using laser flash photolysis. Additionally, it was identified that there were no significant structural changes in structure and chlorophyll binding between LPETG-PsaE PSI and WT PSI.

Prerequisite studies were performed for the insertion of PSI into mixed-lipid liposomes to simulate the native thylakoid membrane. Mixed-lipid liposomes ranging from 0 to 100% egg phosphatidyl choline (ePC) and egg phosphatidic acid (ePA) were solubilized with the detergent, Triton X-100. ePA containing liposomes incorporated higher concentrations of TX than ePC only liposomes before achieving saturation and initiating dissolution into detergent and lipid mixed-micelles. It was concluded that the difference in lipid shape determined detergent incorporation, in that the conical shape of ePA increased mismatching in the bilayer and enabled increased uptake of detergent before complete dissolution compared to the cylindrical shape of ePC. Furthermore, the shape of ePA was adjusted with pH to the conclusion that less conical ePA behaved more similarly to ePC than more conical ePA. Therefore, it is the overall lipid shape moving from cylindrical to conical that affects the incorporation of TX detergent in the bilayer and the total concentration of TX that can be incorporated before the bilayer initiates disruption. The future direction for this

work is examining lower molar ratios of ePC:ePA in mixed-lipid liposomes to observe a critical threshold of conical lipids in a bilayer that causes a marked increase in D_{sat} and D_{sol} such that it is more similar to ePA only liposomes. Other combinations of prevalent lipids in nature, such as phosphatidylglycerol (PG), phosphatidylethanolamine (PE), and phosphatidylserine (PS), should be used at varying ratios in mixed-lipid liposomes with detergent solubilization experiments to gain insight into these lipid interactions within bilayers. Additionally, detergent solubilization of mixed-lipid liposomes should be extended beyond binary lipid combinations to ternary and quaternary lipid combinations. The wide range of lipid combinations will enable better replication of natural membranes for *in vitro* liposomes applications. Additionally, mutant PSI should be inserted into 75:25 ePC:ePA mixed-lipid liposomes. The structure and activity should characterized and compared with data found in this dissertation. Next, hydrogenase enzyme should be modified with a GGG-peptide sequence and ligated to PSI in a liposome. Hydrogen production should be observed in the presence of DCPIP under light conditions.

Furthermore, an equilibrium model was derived describing detergent association with membranes when there are more than one membrane type present. The model is supported by saturation data from solubilizing mixed egg phosphotidylcholine (ePC) liposomes and egg phosphatidic acid (ePA) liposomes with detergent. To fit the model, only detergent saturation of the two pure species liposomes is necessary. It then fits parameters for the the relationship between liposome size change due to detergent uptake and measured signal (e.g. absorbance spectrophotometry signal) and for the fraction of detergent sites in one of the liposome species to determine the detergent concentration at saturation of any given ratio of the two liposome species. The equilibrium model determines the number of detergent binding events that occur at saturation in each of the liposome populations present. Future directions should expand the equilibrium model to a three or more liposome species system and verify the derived models with experimental data.

Vita

Samantha Tyane Clark comes from Mobile, Alabama. She received her Bachelors of Science degree in Nutrition and Food Science in December of 2010 from Auburn University in Auburn, Alabama. She studied chemical engineering at the bachelors level in 2011 at the University of South Alabama, and joined the graduate chemical engineering program at the University of Tennessee, Knoxville in August of 2012, where she received her Masters of Science in August of 2015 and is defending her doctoral dissertation in July of 2019.